Journal of Nanomaterials

Nanomaterials for Sustainable Development in Agriculture

Lead Guest Editor: Thanh-Dong Pham
Guest Editors: Van-Duong Dao, Ajit Kumar Sharma, and Nguyen Van Noi

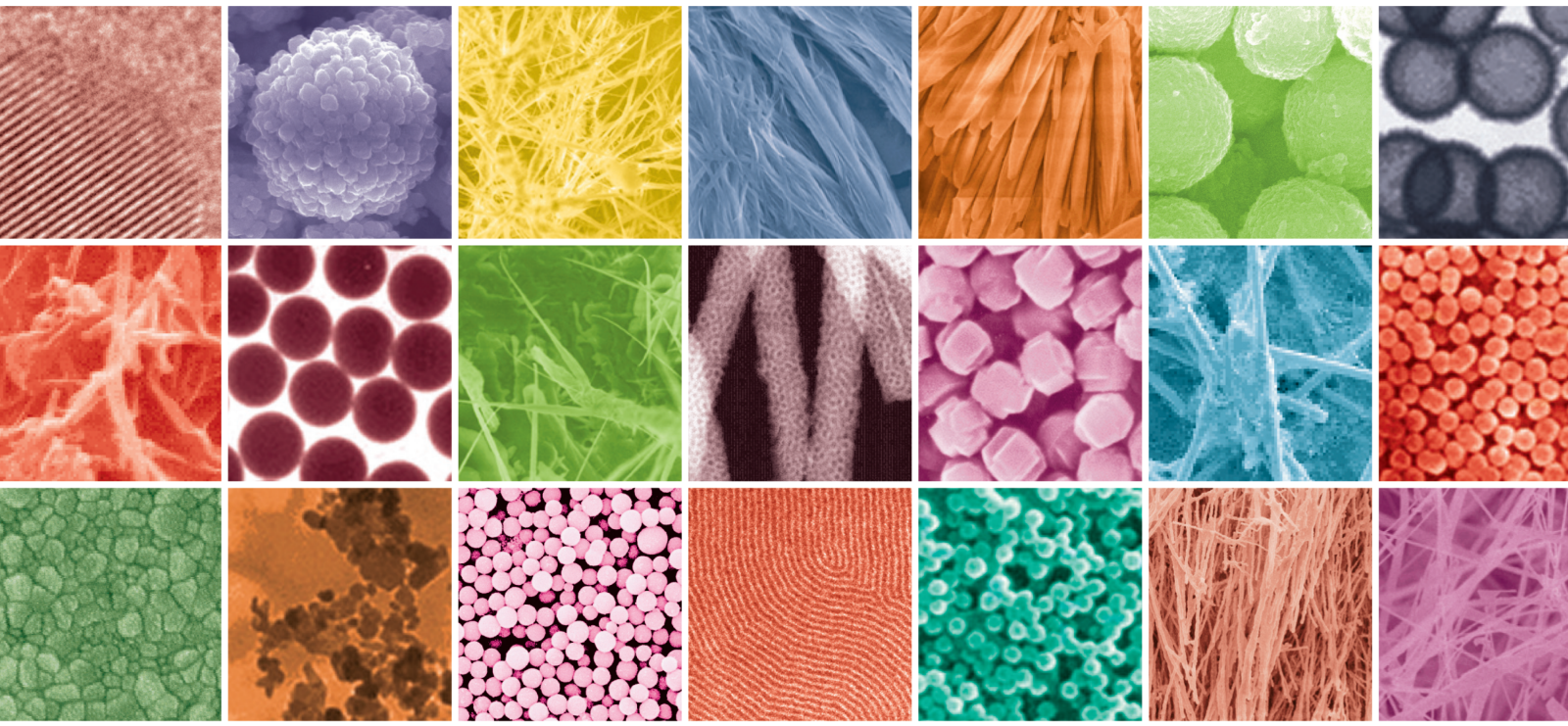

Nanomaterials for Sustainable Development in Agriculture

Journal of Nanomaterials

Nanomaterials for Sustainable Development in Agriculture

Lead Guest Editor: Thanh-Dong Pham
Guest Editors: Van-Duong Dao, Ajit Kumar Sharma, and Nguyen Van Noi

Contents

Hindawi
Journal of Nanomaterials
Volume 2022, Article ID 1777187, 9 pages
https://doi.org/10.1155/2022/1777187

Research Article

Study on Leaching of Phosphate from Municipal Wastewater Treatment Plant's Sewage Sludge and Followed by Adsorption on Mg-Al Layered Double Hydroxide

Thao Phuong[1], **Tien Dung Cong**[2], **Van Thanh Ta**[1] and **Thu Hang Nguyen**[3]

[1]*Faculty of Chemistry, VNU University of Science, Hanoi 100000, Vietnam*
[2]*Hanoi University of Mining and Geology, Hanoi 100000, Vietnam*
[3]*Vietnam-Russian Tropical Centre, Hanoi 100000, Vietnam*

Correspondence should be addressed to Thao Phuong; phuongthao@hus.edu.vn

Received 1 July 2021; Revised 4 January 2022; Accepted 17 January 2022; Published 2 February 2022

Academic Editor: Gaurav Sharma

Sewage sludge from municipal wastewater treatment plant was a rich phosphorus resource. In this study, HCl, H_2SO_4, and HNO_3 were investigated as leaching acids for extraction of phosphate from the sludge to recover this value nutrient by adsorption using layered double hydroxide (LDH) nanomaterial. Mg-Al LDH was synthesized by coprecipitation at room temperature and at a constant pH of 10 (±0.5) with Mg/Al molar ratio of 2.0. The material was characterized by scanning electron microscopy (SEM), X-ray diffraction (XRD), Brunauer-Emmet-Teller (BET), and Fourier transform infrared spectroscopy (FTIR) and then was used to adsorb phosphate leaching from the sewage sludge. Adsorption experiments were carried out as a function of adsorbent dose, phosphate initial concentrations, and pH. The adsorption isotherm data fitted the Langmuir model perfectly. The high adsorption capacity of Mg-Al LDH and slowly released phosphate of the post-adsorption LDH suggested that this material was an excellent adsorbent for phosphate recovery and could be considered as a potential phosphate release fertilizer.

1. Introduction

Phosphorus (P) is an essential nutrient for plant growth. In the form of phosphate, it was used to produce fertilizers in order to increase yields in agriculture. It also presents in many products that are widely used such as detergents, hardeners, toothpaste, corrosion inhibitors, industrial food additives [1]. However, the over-use of fertilizers, as well as phosphate-containing products causes a large amount of phosphate to accumulate in the soil or be washed out into rivers, streams, ponds, lakes, and present in wastewater contributes to significant phosphate pollution [2]. Pollution of phosphate in the aquatic environment can lead to the phenomenon called eutrophication, in which algal blooms excessively, dissolved oxygen will be largely consumed, so it causes serious effects on the quality of water and aquatic life [3].

In the face of such phosphate pollution, the treatment and control of phosphates in wastewater is a big challenge. According to data of the Vietnam Water Supply and Sewerage Association by the end of 2016, out of 35 centralized wastewater treatment systems operating in the country, only 7 biological treatment plants combine nitrogen and phosphate treatment thoroughly [4]. Nowadays, phosphate control is interested with the main research focusing on treatment techniques such as precipitation, adsorption, ion exchange, and biological treatment [4, 5]. However, we should know that the natural supplies of phosphate are nonrenewable and will be exhausted quickly. Because of the irreplaceable role of phosphate in fertilizer production, the objective of phosphate treatment should change from removal to recovery.

In conventional municipal wastewater treatment, it was reported that around 90% of incoming phosphorus load is concentrated in the sewage sludge [6]. Although sewage sludge from municipal wastewater treatment plant (MWTP) has high amounts of phosphate, it should not be used directly as fertilizer due to concerns about its consisting of heavy metals, pathogens, and other toxic matters [7].

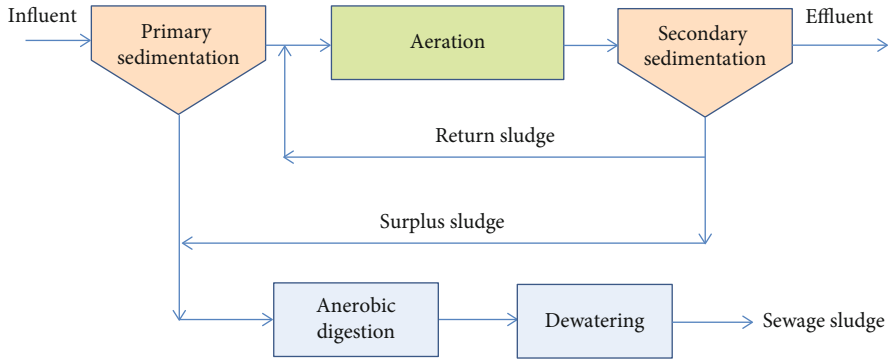

Figure 1: Municipal wastewater treatment system of Truc Bach plant.

Moreover, phosphate fix in the sludge exhibits low availability for plant to absorb [8]. So, the main technologies for phosphate recovery from sludge are leaching phosphate bound in the sludge into the liquid phase and then recovering phosphate from the supernatant by chemical precipitation or adsorption.

In order to extract phosphate from the sludge phase, wet chemical and thermochemical treatments are used [9]. In the thermochemical process, high purity of recovered phosphate is achieved but the high consumption of energy and specific equipment are needed [10]. In the wet chemical approach, both strong acids and alkalis were suggested. However, adding acids is reported more effective than adding alkalis. Alkali leaching achieves about 60-70% of total P separated from sewage sludge [11], while acid leaching can release over 80% of P [12].

After being released through the wet chemical process, the more effective method to recover phosphate in the leachate is adsorption. Recently, layered double hydroxides (LDHs), also known as hydrotalcite-like compounds or anionic clay, are considered promising materials that can effectively adsorb phosphates due to structural resemblance with the cation clays and exhibit high anion exchange capacity and good affinity for phosphate [13, 14]. LDHs are 2D nanomaterials that have the general formula $[M_{1-x}^{2+}M_x^{3+}(OH)_2]^{x+}[(A^{n-})_{x/n}.mH_2O]^{x-}$, where M^{2+} and M^{3+} are di- and trivalent metallic cations, respectively, and A^{n-} is an intercalated anion, which has the ability to be exchanged for other anions in solution giving special properties of LDHs [15]. LDHs have been proven as excellent adsorbents for phosphate removal from aqueous solutions in many research works [16].

It is indicated that phosphate ions are adsorbed on LDHs via electrostatic attraction, ligand exchange, and ion exchange [17, 18]. Previous studies mainly focused on phosphate recovery from waste streams by LDHs, followed by a release of phosphate from these materials by desorption solutions such as NaCl or NaOH [19]. Recently, it is noticed that LDHs are able to slowly release intercalated phosphate due to their unique structure [20]. After adsorption, the LDHs provide physical protection to phosphate, decreasing the direct contact of phosphate with the soil; therefore, phosphate can be released in a more controlled way. This means that phosphate loaded LDHs might be used directly as slow and controlled release P fertilizers in soils [21, 22]. The development of LDHs as fertilizers really makes sense to connect the recycling of phosphorus from waste streams and phosphorus fertilizers. Moreover, uptake of nutrients can be increased by encapsulating the phosphorus fertilizers in nanoform that provide gradual and controlled release of phosphate to the target sites through direct internalization of products, therefore ultimately reducing phosphorus loss and minimizing the risk of environmental pollution [23, 24].

In this paper, the wet chemical method using strong acids was tested for leaching of phosphate from municipal wastewater treatment plant's sewage sludge, and then recovery of phosphate in the leachate by adsorption onto Mg-Al layered double hydroxide nanomaterial was the aim of the study.

Table 1: Total phosphorus and metal composition of the sewage sludge.

Composition	Concentration	Unit
Total P	3.4	%
Cd	0.839	μg/L
Mg	9.151	mg/L
As	0.071	mg/L
Sn	1.695	μg/L
Na	0.518	mg/L
Hg	7.382	μg/L
Zn	0.604	mg/L
Al	29.977	mg/L
Ca	14.376	mg/L
Mn	0.255	mg/L
Fe	11.360	mg/L
Ni	0.019	mg/L
Cr	0.045	mg/L
Cu	0.098	mg/L
Pb	0.032	mg/L

2. Materials and Methods

2.1. Sludge Characteristics. Sludge was obtained from Truc Bach MWTP in Hanoi, Vietnam. The wastewater treatment system of this plant is presented as in Figure 1.

Table 2: Equations and parameters of isotherm models.

Isotherm models	Equation	Parameters
Langmuir	$q_e = \frac{q_{max} b C_e}{1 + bC_e}$ $R_L = \frac{1}{1 + bC_0}$	q_e (mg/g) is the equilibrium adsorption capacity. q_{max} (mg/g) is the maximum adsorption capacity. b (L/mg) is the Langmuir isotherm constant related to the energy of adsorption. R_L is a factor of adsorption feasibility.
Freundlich	$q_e = k_f C_e^{1/n}$	k_f and n are Freundlich isotherm constants related to adsorption capacity and adsorption intensity.
Dubinin-Radushkevich	$q_e = q_m \exp(-\beta\varepsilon^2)$ $\varepsilon = \mathrm{RTln}\left[1 + \frac{1}{C_e}\right]$ $E = \left[\frac{1}{\sqrt{-2\beta}}\right]$	q_m is the Dubinin-Radushkevich constant. β (mol^2/kJ^2) is the activity coefficient related to mean sorption energy. ε is the Polanyi potential. E (kJ/Mol) is the mean sorption energy.

The sewage sludge after dewatering was used in this study. Total phosphorus in the sludge was measured according to the procedure given in Vietnam Standards TCVN 8940-2011 [25]. Metals from the sludge were extracted in the ETHOS UP Microwave Digestion System according to U.S.EPA Method 3051A [26], and their concentration was measured on an inductively coupled plasma spectrometer (iCAP Q ICP-MS) according to SMEWW 3125 : 2017 [27]. The ICP measurements were made in duplicates to get the average data. Phosphorus and metal composition of the raw sewage sludge are presented in Table 1.

2.2. Acid Leaching of Sludge. The ability of leaching phosphate from the sludge was tested by the wet chemical method, which was individually carried out by using strong acids HCl, H_2SO_4, and HNO_3 at varying concentrations (0.05-2.0 mol/L HCl and H_2SO_4; 1.0-5.0 mol/L HNO_3). The liquid/solid (L/S) ratios of 10 : 1; 25 : 1, and 50 : 1 (mL/g) were examined. The leaching experiments were carried out at room temperature and shaken at 100 r/min for 24 h. After filtered through 1 μm ashless filter paper, the concentration of phosphate in the leachate was measured according to the Vanadomolipdophosphoric acid colorimetric method [28] and compared to its concentration in the raw sludge to calculate the leaching percentage; so, the optimal condition for leaching phosphate from the sludge would be determined.

2.3. Synthesis of Mg-Al Layered Double Hydroxide. In this study, Mg-Al LDH was synthesized by coprecipitation from the solution of $Mg(NO_3)_2.6H_2O$ and $Al(NO_3)_3.9H_2O$ (initial Mg/Al molar ratio of 2.0). The pH was maintained at 10 ± 0.5 by adding 2.0 M NaOH and 0.5 M K_2CO_3. The synthesis was performed at room temperature. The resulting precipitate was aged for 24 h and washed with deionized water until the effluent solution pH was neutral. After drying at 90°C overnight, the precipitate was lightly grounded to get particle size from 0.5 to 1.0 mm.

Crystal phases of the Mg-Al LDH were performed on Rigaku Miniflex 600 X-ray diffractometer using CuK-α radiation. Surface area and pore analysis were performed using the Brunauer-Emmet-Teller (BET) approach on a NOVA-touch LX4 adsorption analyzer. FTIR spectra were collected on a Jasco 4600 FTIR spectrophotometer. Scanning electron microscopy (SEM) was conducted to observe the surface morphological structure of synthesized Mg-Al LDH using a Hitachi S4800 scanning electron microscope.

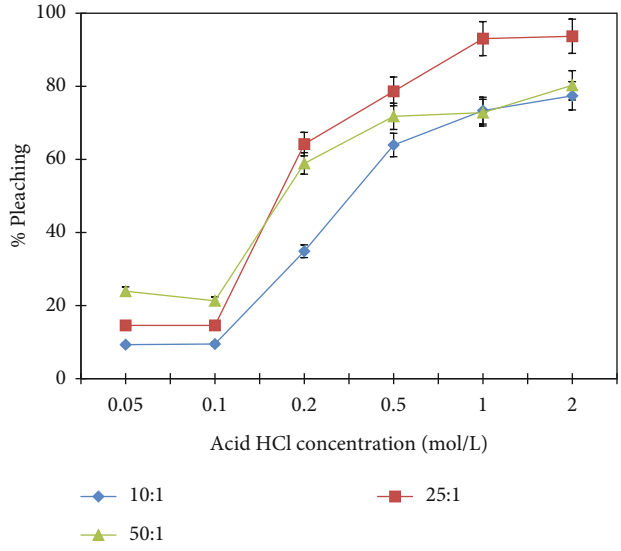

Figure 2: Effect of HCl concentration and L/S ratio on the leaching of phosphate from the sewage sludge.

2.4. Phosphate Recovery from Acid Leachate. Synthesized Mg-Al LDH was used to adsorb phosphate from acid leachate. The adsorption experiments were carried out in batches with 50 mL of adsorbed solution at neutral pH (adjusted by diluted NaOH) and at room temperature. After the equilibrium time (6 h), LDH was separated from the solution by centrifugation, and phosphate was analyzed in the solution by the Vanadomolipdophosphoric method. All the analyses were taken in triplicates. The adsorption capacity of the material q and adsorption efficiency E (%) was calculated according to the following formulas:

$$q = \frac{(C_0 - C_e)V}{m}, \quad (1)$$

$$E = \frac{(C_0 - C_e)}{C_0} \times 100\%, \quad (2)$$

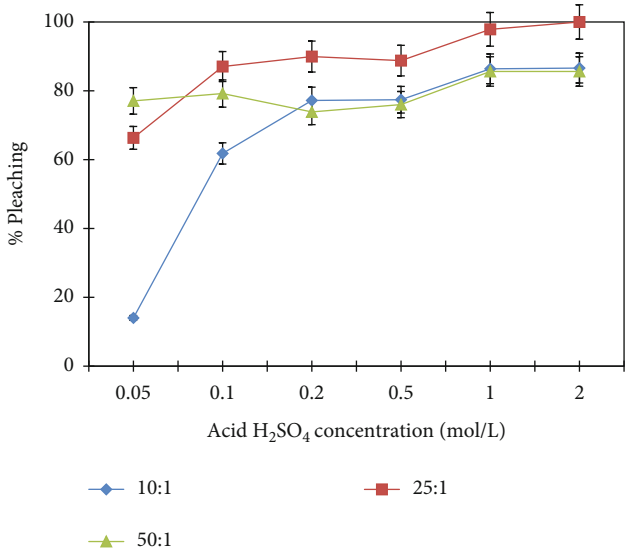

Figure 3: Effect of H_2SO_4 concentration and L/S ratio on the leaching of phosphate from the sewage sludge.

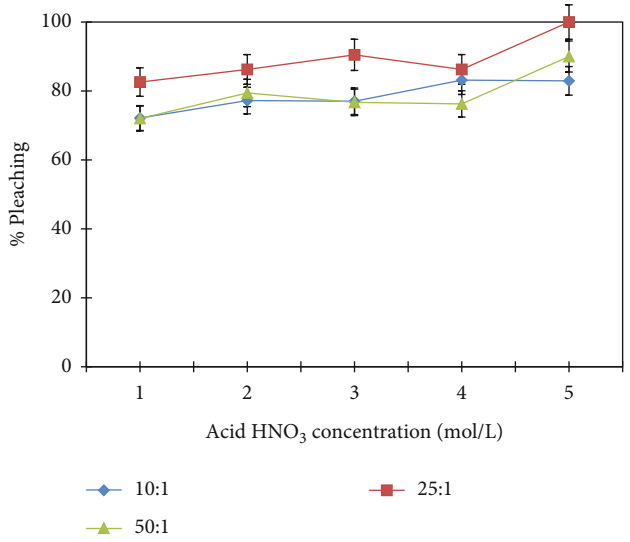

Figure 4: Effect of HNO_3 concentration and L/S ratio on the leaching of phosphate from the sewage sludge.

where C_0 and C_e are the initial and equilibrium concentration of phosphate in leachate (mg/L), q is the equilibrium adsorption capacity (mg/g), m is the adsorbent dry weight (g), and V is the adsorbed solution volume (L).

The influence of LDH dosage, the initial concentration of phosphate in leachate (adsorption isotherm), and pH are factors investigated in this work.

2.5. Adsorption Isotherms. The relationship between the amount adsorbed and adsorbate concentration in the aqueous phase at equilibrium was evaluated using three isotherm models: Langmuir, Freundlich, and Dubinin-Radushkevich models. Langmuir isotherm assumes the existence of a maximum adsorption limit corresponding to a complete monolayer formation of the adsorbate on the adsorbent surface.

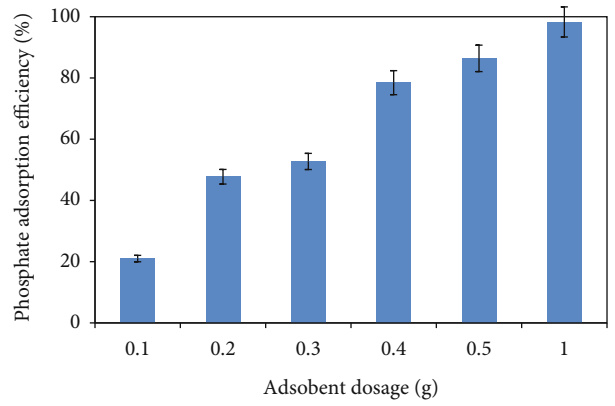

Figure 5: Phosphate recovery from acid leachate as a function of LDH dosage from 0.1 g to 1.0 g.

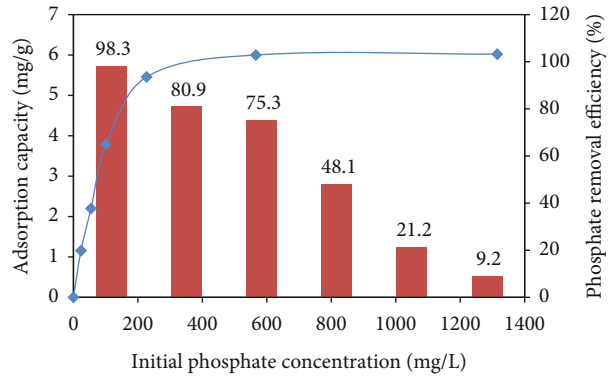

Figure 6: Adsorption capacity and removal efficiency of phosphate on Mg-Al LDH as a function of initial phosphate concentration.

The computed R_L value suggests the adsorption nature to be either unfavorable ($R_L > 1$), linear ($R_L = 1$), favorable ($0 < R_L < 1$), or irreversible ($R_L = 0$) [29]. The Freundlich model is often used to describe chemisorption on heterogeneous surfaces [30]. The Dubinin-Radushkevich model was commonly used to determine the adsorption type as physisorption or chemisorption [31]. Equations and parameters of the isotherm models are presented in Table 2.

2.6. Phosphate Release from LDH. To evaluate the applicability as a slow-release fertilizer of phosphate adsorbed LDH, 5 g of the material was put in a sealed plastic bottle containing 50 mL of the distilled water adjusted pH = 4, 6, and 8 at room temperature. After a certain time (1, 3, 5, 7, 10, 14, 28 days), the solution was decanted to determine the phosphate content, and another 50 mL of new pH adjusted water was added to the bottle to analyze for the next time. The solution was shaken well before taking samples for analysis.

3. Results and Discussion

3.1. Factors Affecting the Leaching Process. The effect of HCl, H_2SO_4, and HNO_3 on phosphate leaching from the sewage sludge at different concentrations and L/S ratios is depicted in Figures 2–4.

Table 3: Isotherm parameters for phosphate adsorption on Mg-Al LDH.

Freundlich isotherm		Langmuir isotherm		Dubinin-Radushkevich isotherm	
Parameters	Value	Parameters	Value	Parameters	Value
K_f (mg/g)	1.519	q_{max} (mg/g)	6.086	q_m (mg/g)	4.407
$1/n$	0.223	b (L/mg)	0.088	β (mol^2/kJ^2)	1.00E-07
R^2	0.931	R^2	0.999	R^2	0.671
		R_L	0.009-0.326	E (kJ/Mol)	1.581

The figures show that in most cases, the phosphate leaching increases with increasing acid concentration and gets the best results at the L/S ratio of 25 : 1. At this ratio, approximately 80% of phosphate was leached at a concentration of 0.1 mol/L and higher in the case of using H_2SO_4 and at higher than 0.5 mol/L and 1 mol/L in the cases of using HCl and HNO_3, respectively. H_2SO_4 seems to be the best acid for phosphate leaching. Considering the cost-effective consumption of acid and achievement of complete leaching of phosphate, 1.0 mol/L H_2SO_4 acid at the L/S ratio of 25 : 1 was chosen as the most suitable condition for phosphate leaching.

3.2. Recovery of Phosphate from Acid Leachate by Adsorption on Mg-Al LDH. Phosphate from acid leachate was recovered by adsorption on the synthesized Mg-Al LDH. The phosphate adsorption was investigated at different adsorbent doses, phosphate initial concentrations, and pH values.

3.2.1. Effect of Adsorbent Dose. The effect of Mg-Al LDH dosage from 0.1 to 1.0 g on the phosphate adsorption at the initial concentration of 23.46 mg/L (diluted acid leachate 100 times) was studied. As presented in Figure 5, the phosphate recovery increases with an increasing amount of the LDH. More than 80% of phosphate in leachate was uptaken at the adsorbent dose of 0.5 g, and nearly 100% was obtained at the dose of 1.0 g. So, the most suitable adsorbent dose for phosphate adsorption in 50 mL solution was 1.0 g.

3.2.2. Effect of Phosphate Initial Concentration. Different initial phosphate concentrations were prepared by diluted the acid leachate at different ratios (1 : 100, 1 : 50, 1 : 25, 1 : 10, 1 : 5, 1 : 2).

The results illustrated in Figure 6 showed that when varying the initial concentrations from 23.5 to 1315.0 mg/L, the adsorption capacity firstly increased and then reached the equilibrium capacity. However, the percentage removal decreased from 98.3% to 9.2% with the increase in phosphate concentration. The decrease in phosphate adsorption efficiency could suggest the lack of an available area required for the high initial concentrations of phosphate.

Adsorption capacity at different equilibrium concentrations could be illustrated by the adsorption isotherm. The three commonly used isotherms, Langmuir, Freundlich, and Dubinin-Radushkevich isotherm models, were applied, and the summary data are presented in Table 3.

The results showed that the adsorption of phosphate on Mg-Al LDH was perfectly described by the Langmuir isotherm with $R^2 = 0.999$. The fitting of equilibrium adsorption

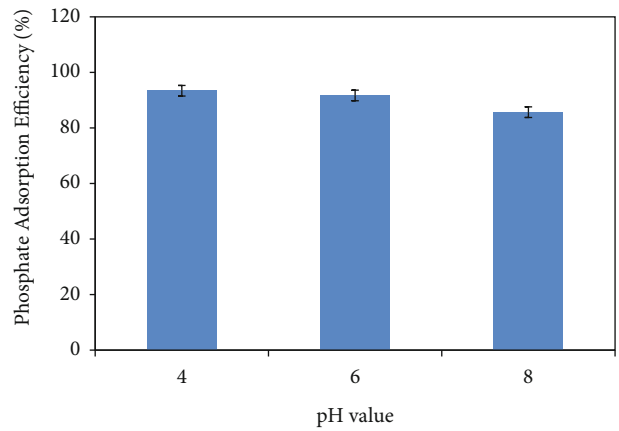

Figure 7: Efficiency of phosphate adsorption from acid leachate on Mg-Al LDH as a function of pH.

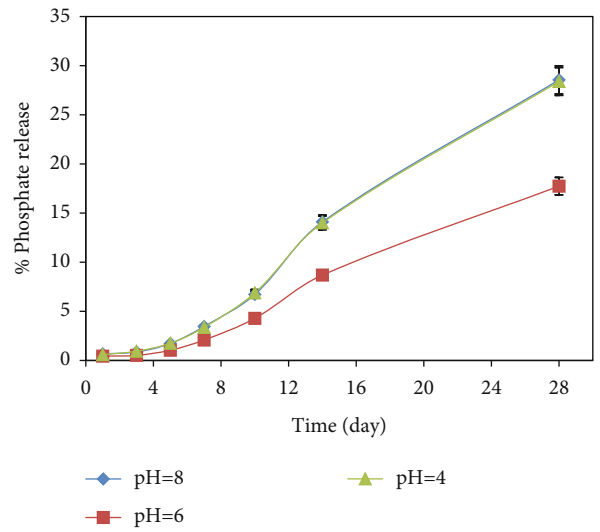

Figure 8: Efficiency of phosphate release from adsorbed Mg-Al LDH at pH = 4, 6, 8 using distilled water for desorption.

to Langmuir isotherm model suggests that monolayer and homogeneous adsorption onto the surface containing a finite number of identical sites were taken place [31]. This is in accordance with the anionic exchange mechanism involved in the phosphate adsorption on LDH. Moreover, the R_L values found in this study were between 0 and 1 which means the adsorption process is favorable. Furthermore, from the Freundlich isotherm data, the value of $1/n$ was

Table 4: Metal content in the adsorbed Mg-Al-LDH.

(a)

Metal	Cd	Pb	As	Cu
Content (mg/kg)	1.31	46.83	0.49	41.15
QCVN-01-189 : 2019/BNNPTNT	≤5 mg/kg	≤200 mg/kg	≤10 mg/kg	<1000 mg/kg

(b)

Metal	Fe	Mn	Zn	Ca
Content (mg/kg)	289.07	29.14	366.86	13,897.49 (or 1.38%)
QCVN-01-189 : 2019/BNNPTNT	<1000 mg/kg	<1000 mg/kg	<1000 mg/kg	<20%

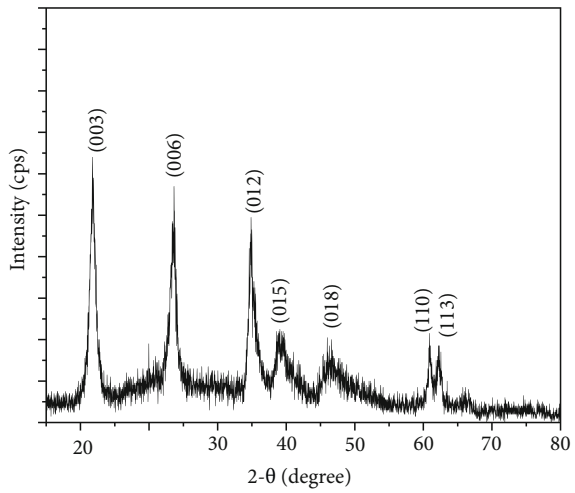

Figure 9: XRD pattern for synthesized Mg-Al LDH.

found to be 0.2231 also indicating that the sorption of phosphate onto Mg-Al LDH is favorable. On the other hand, the mean sorption energy computed from the Dubinin-Radushkevich isotherm equation was determined to be 1.581 kJ/mol indicating a physisorption process. This means that besides the ion exchange mechanism, phosphate anion uptake on the LDH surface was also promoted by the electrostatic attraction between a surface positive charge and the anions.

3.2.3. Effect of pH Value. Phosphate adsorption was evaluated at three different pH values (pH = 4, 6, 8), which presented for the acid, neutral, and basic environment. The results presented in Figure 7 show that the adsorption efficiency decreased when the pH was higher. The adsorption taken at acid and neutral pH was more favorable than at basic pH. The reason for lower adsorption efficiency at higher pH was supposed due to competition with carbonate ions. Moreover, phosphate exists in the lower charge ($H_2PO_4^-$) at low pH that allows for higher adsorption [17].

3.3. Phosphate Released from Adsorbed Mg-Al LDH. After adsorption, phosphate-loaded Mg-Al LDH was examined by the phosphate release efficiency in water at three different pH values as shown in Figure 8.

Table 5: Specific surface area, pore volume, and pore radius.

Sample	Specific surface area (m^2/g)	Pore volume (cm^3/g)	Pore radius (nm)
Mg-Al LDH BA	74.3603	0.19369	6.33512
Mg-Al LDH AA	36.0880	0.14390	7.97485

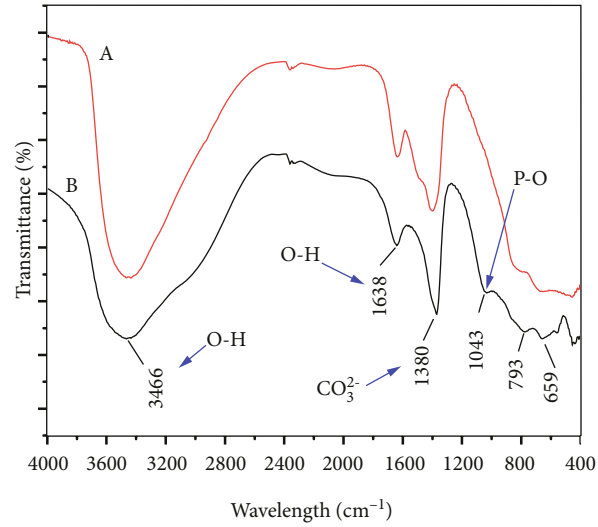

Figure 10: FT-IR spectra of Mg-Al LDH (a) before adsorption and (b) after adsorption.

After 28 days, the phosphate was released only 28.6%, 17.7%, and 28.4% at pH 8, 6, and 4, respectively. The release of phosphate by LDH was clearly slow, despite the process being incomplete, and it could be confirmed that the phosphate-loaded LDH can act as a slow-release fertilizer.

3.4. Evaluation of Metal Content in Adsorbed Mg-Al LDH. It is known that the raw sewage sludge contains metal components in certain concentrations. In the phosphate leaching process from the sewage sludge, strong acid is used, so it is inevitable that the metals will be dissolved into the leachate. To evaluate the possibility of metals being adsorbed on Mg-Al LDH during phosphate recovery from the leachate, the

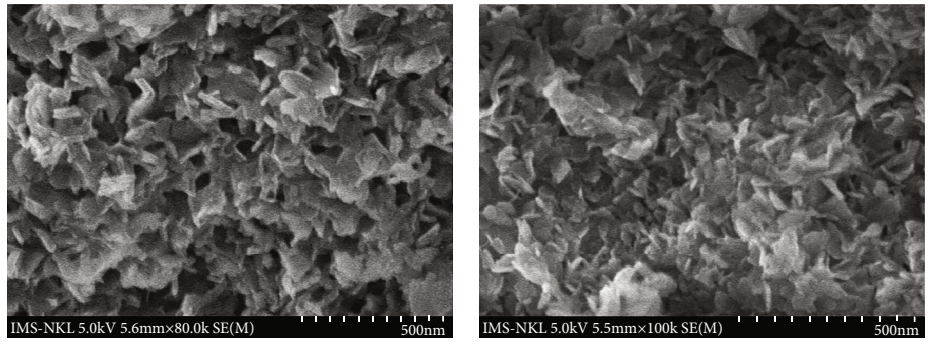

(a) (b)

Figure 11: Scanning electron microscopy images of the synthesized Mg-Al LDH (a) before adsorption and (b) after adsorption.

metal composition in the postadsorption Mg-Al LDH was analyzed according to SMEWW 3125 : 2017 [27].

For the purpose of using the postadsorption Mg-Al LDH as fertilizer, the results of metal composition in the material are compared to Vietnam National Technical Regulation on Fertilizer Quality QCVN-01-189:2019/BNNPTNT [32] as presented in Table 4. The results show that all metals, especially harmful metals such as Cd, Pb, As, and Cu, are much lower than the allowable limit. The presence of Fe, Mn, Zn, and Ca is partly beneficial because they are essential micronutrients for plants.

3.5. Characterization of Synthesized Mg-Al LDH. XRD pattern of synthesized Mg-Al LDH presented in Figure 9 showed typical signal peaks for Mg-Al layered double hydroxide material at 2θ angles of 11.70°, 23.60°, 34.79°, 39.06°, and 60.92°, which are assigned to the crystal planes of (003), (006), (009), (007), and (110).

Corresponding to the (003) and (006) reflections, peaks with large intensity appear, showing the large distance between the interlayers. The basal spacing of (003) reflection of the material was found to be 7.6 Å, which was consistent with the previous reports [20, 33]. This means that the LDH material was successfully synthesized by the coprecipitation method.

BET surface area of Mg-Al LDHs before and after adsorption determined via the Brunauer-Emmett-Teller plot is presented in Table 5. Specific surface area of Mg-Al LDH before adsortion (BA) was similar to the Mg-Al hydrotalcite product of Sigma-Aldrich ($78 m^2/g$) [33] and higher than typical values of the specific surface area measured by BET range from 24.6 to 69 m^2/g of this material [34]. After adsorption, the occupation of phosphate on the surface caused a decrease in pore volume, a slight increase in pore size and a considerable decrease in specific surface area.

Mg-Al LDH materials before and after phosphate adsorption were also analyzed by infrared spectrum. The results are shown in Figure 10.

On the FTIR spectrum of the LDH before and after adsorption, spectral lines typical for Mg-Al layered double hydroxide can be seen. The broad absorption band in the range 3800-2500 cm^{-1} is attributed to the valence vibrations of the O-H group in the LDH molecule and of the interlayer adsorbed water molecules. The peak located at 1638 cm^{-1} is assigned to the O-H bending vibration and indicated the presence of interstitial water molecules. Other absorption bands in the region below 1000 cm^{-1} characterize the oscillations of Mg-O and Al-O bonds in LDH. The new peak appearing at 1043 cm^{-1} on the postadsorption material is believed to be of the P-O bond, which gives information about the inner spherical surface (M-O-P) complex between phosphate and LDH [35]. It is therefore suggested that the surface hydroxyl groups (M-OH) of LDH are likely to be exchanged by phosphate ion, which is reported as the main mechanism for phosphate adsorption on LDH material [20].

The morphology of synthesized LDHs before and after adsorption is provided in Figure 11. SEM images show a well-developed layered structure with a fine dispersion of the platelet-like particles having estimated lateral size around a few tens of nanometers, and thickness is about a few nanometers. It also reveals relatively obvious hexagon overlapping crystals, which are typical for LDHs. The morphology features do not change after the adsorption and are similar to those observed in previous studies [14, 30, 36].

High specific surface area, unique morphology, and nanoparticle size are extremely important properties that make LDH have excellent phosphate adsorption capacity and well-controlled release ability.

4. Conclusions

The study of phosphate extraction from municipal wastewater treatment plant's sewage sludge has been performed for the view of recovery phosphate by Mg-Al layered double hydroxide. It could be confirmed that sewage sludge from municipal wastewater treatment plant was a beneficial source to recover phosphate. The conditions for above 80% of phosphate leaching were 0.1 mol/L H_2SO_4 or 1 mol/L HCl or 1 mol/L HNO_3 at the L/S ratio of 25 : 1 for 24 hours shaking at room temperature (~30°C). Mg-Al LDH with Mg:Al molar ratio of 2 : 1 was successfully synthesized and applied to adsorb phosphate from acid leachate. The synthesized LDH as a nanomaterial showed excellent phosphate adsorption efficiency at experimental conditions. Phosphate uptake by Mg-Al LDH fitted the Langmuir adsorption isotherm model perfectly and was intercalated in the LDH by exchange with ion carbonate. The LDH after adsorption could slowly release phosphate, which appears to be a

promising controlled release phosphate fertilizer. Metal content, especially harmful heavy metals such as Cd, Pb, As, and Cu in the adsorbed LDH, is much lower than the maximum allowable content specified in Vietnam National Technical Regulation on fertilizer quality. Thus, phosphate recovery from MWTP's sewage sludge by Mg-Al LDH after acid leaching may contribute to solving the problem of phosphate deficiency.

Data Availability

Data are available on request.

Conflicts of Interest

The authors declare that there is no conflict of interest regarding the publication of this paper.

Acknowledgments

This research is funded by the Vietnam National University, Hanoi (VNU), under project number QG.20.10.

References

[1] S. T. Hisao Ohtake, *Eds. Phosphorus Recovery and Recycling-Springer Singapore*, Springer, Singapore, 2019.

[2] O. Zoboli, M. Zessner, and H. Rechberger, "Supporting phosphorus management in Austria: potential, priorities and limitations," *Sci Total Environ*, vol. 565, pp. 313–323, 2016.

[3] E. M. Seftel, R. G. Ciocarlan, B. Michielsen, V. Meynen, S. Mullens, and P. Cool, "Insights into phosphate adsorption behavior on structurally modified ZnAl layered double hydroxides," *Applied Clay Science*, vol. 165, pp. 234–246, 2018.

[4] N. Cuong, 2017, https://baotainguyenmoitruong.vn/xu-ly-nito-va-phot-phat-trong-nuoc-thai-do-thi-246877.html.

[5] O. F. Schoumans, F. Bouraoui, C. Kabbe, O. Oenema, and K. C. van Dijk, "Phosphorus management in Europe in a changing world," *Ambio*, vol. 44, Suppl 2, pp. 180–192, 2015.

[6] L. D. C. Cédric Tarayre, R. Charlier, E. Michels, E. Meers, M. Camargo-Valero, and F. Delvigne, "New perspectives for the design of sustainable bioprocesses for phosphorus recovery from waste," *Bioresource Technology*, vol. 206, pp. 264–274, 2016.

[7] S. Donatello and C. R. Cheeseman, "Recycling and recovery routes for incinerated sewage sludge ash (ISSA): a review," *Waste Management*, vol. 33, no. 11, pp. 2328–2340, 2013.

[8] H. Kahiluoto, M. Kuisma, E. Ketoja, T. Salo, and J. Heikkinen, "Phosphorus in manure and sewage sludge more recyclable than in soluble inorganic fertilizer," *Environmental Science & Technology*, vol. 49, no. 4, pp. 2115–2122, 2015.

[9] S. Petzet, B. Peplinski, and P. Cornel, "On wet chemical phosphorus recovery from sewage sludge ash by acidic or alkaline leaching and an optimized combination of both," *Water Research*, vol. 46, no. 12, pp. 3769–3780, 2012.

[10] H. Herzel, O. Kruger, L. Hermann, and C. Adam, "Sewage sludge ash–a promising secondary phosphorus source for fertilizer production," *Sci Total Environ*, vol. 542, pp. 1136–1143, 2016.

[11] M. Takaoka, K. Oshita, X. Cui, K. Matsukawa, and T. Fujiwara, "Phosphorus material flow and its recovery from wastewater and solid waste," in *UNEP-DTIE-IETC, Regional Workshop on Waste Agricultural Biomass, Ed.*, Global Environment Centre Foundation in Osaka, 2010.

[12] B. K. Biswas, K. Inoue, H. Harada, K. Ohto, and H. Kawakita, "Leaching of phosphorus from incinerated sewage sludge ash by means of acid extraction followed by adsorption on orange waste gel," *Journal of Environmental Sciences*, vol. 21, no. 12, pp. 1753–1760, 2009.

[13] K. Kuzawa, Y. J. Jung, Y. Kiso, T. Yamada, M. Nagai, and T. G. Lee, "Phosphate removal and recovery with a synthetic hydrotalcite as an adsorbent," *Chemosphere*, vol. 62, no. 1, pp. 45–52, 2006.

[14] R. Borges, F. Wypych, E. Petit, C. Forano, and V. Prevot, "Potential sustainable slow-release fertilizers obtained by mechanochemical activation of MgAl and MgFe layered double hydroxides and K2HPO4," *Nanomaterials (Basel)*, vol. 9, no. 2, p. 183, 2019.

[15] R. A. S. L. P. F. Benício, R. A. Silva, J. A. Lopes et al., "Layered double hydroxides: nanomaterials for applications in agriculture," *Revista Brasileira de Ciência do Solo*, vol. 39, no. 1, pp. 1–13, 2015.

[16] K. H. Goh, T. T. Lim, and Z. Dong, "Application of layered double hydroxides for removal of oxyanions: a review," *Water Research*, vol. 42, no. 6-7, pp. 1343–1368, 2008.

[17] L. Lundehoj, H. C. Jensen, L. Wybrandt, U. G. Nielsen, M. L. Christensen, and C. A. Quist-Jensen, "Layered double hydroxides for phosphorus recovery from acidified and non-acidified dewatered sludge," *Water Research*, vol. 153, pp. 208–216, 2019.

[18] K. Yang, L. G. Yan, Y. M. Yang et al., "Adsorptive removal of phosphate by Mg-Al and Zn-Al layered double hydroxides: Kinetics, isotherms and mechanisms," *Separation and Purification Technology*, vol. 124, pp. 36–42, 2014.

[19] X. Cheng, X. Huang, X. Wang, B. Zhao, A. Chen, and D. Sun, "Phosphate adsorption from sewage sludge filtrate using zinc-aluminum layered double hydroxides," *Journal of Hazardous Materials*, vol. 169, no. 1-3, pp. 958–964, 2009.

[20] F. W. Roger Borges, E. Petit, C. Forano, and V. Prevot, "Controlled release of phosphate from LDH structures: dynamics in soil and application as smart fertilizer," *Nanomaterials (Basel)*, vol. 9, no. 183, pp. 1–18, 2019.

[21] M. Everaert, R. Warrinnier, S. Baken, J.-P. Gustafsson, D. De Vos, and E. Smolders, "Phosphate-exchanged Mg–Al layered double hydroxides: a new slow release phosphate fertilizer," *ACS Sustainable Chemistry & Engineering*, vol. 4, no. 8, pp. 4280–4287, 2016.

[22] J. J. Weeks and G. M. Hettiarachchi, "A review of the latest in phosphorus fertilizer technology: possibilities and pragmatism," *Journal of Environmental Quality*, vol. 48, no. 5, pp. 1300–1313, 2019.

[23] D. Mittal, G. Kaur, P. Singh, K. Yadav, and S. A. Ali, "Nanoparticle-based sustainable agriculture and food science: recent advances and future outlook," *Frontiers in Nanotechnology*, vol. 2, 2020.

[24] Y. Shang, M. K. Hasan, G. J. Ahammed, M. Li, H. Yin, and J. Zhou, "Applications of nanotechnology in plant growth and crop protection: a review," *Molecules*, vol. 24, no. 14, p. 2558, 2019.

[25] TCVN, *TCVN 8940:2011 soil quality – determination of total phosphorus – colorimetry method*, Vietnam National Standard, Hanoi, 2011.

[26] U S EPA, "Method 3051A microwave assisted acid digestion of sediments, sludges, soils, and oils," *Z. Für Anal. Chem*, vol. 111, pp. 362–366, 2007.

[27] APHA, "Standard methods for the examination of water and wastewater," in *Method 3125 Metals by inductively coupled plasma-mass spectrometry*, American Public Health Association, 1912.

[28] APHA, "Standard methods for the examination of water and wastewater," in *4500-P C*, Vanadomolybdophosphoric Acid Colorimetric Method, Washington, 1998.

[29] Y. W. Berkessa, S. T. Mereta, and F. F. Feyisa, "Simultaneous removal of nitrate and phosphate from wastewater using solid waste from factory," *Applied Water Science*, vol. 9, no. 2, 2019.

[30] C. Novillo, D. Guaya, A. Allen-Perkins Avendaño, C. Armijos, J. L. Cortina, and I. Cota, "Evaluation of phosphate removal capacity of Mg/Al layered double hydroxides from aqueous solutions," *Fuel*, vol. 138, pp. 72–79, 2014.

[31] D A O, "Langmuir, Freundlich, Temkin and Dubinin–Radushkevich isotherms studies of equilibrium sorption of Zn 2+ unto phosphoric acid modified rice husk," *IOSR Journal of Applied Chemistry*, vol. 3, no. 1, pp. 38–45, 2012.

[32] QCVN, *01-189:2019/BNNPTNT, "Vietnam National Technical Regulation on fertilizer quality"*, 2019.

[33] S. Park, D. Kwon, J. Y. Kang, and J. C. Jung, "Influence of the preparation method on the catalytic activity of Mg Al hydrotalcites as solid base catalysts," *Green Energy & Environment*, vol. 4, no. 3, pp. 287–292, 2019.

[34] M. Molano-Mendoza, D. Donneys-Victoria, N. Marriaga-Cabrales, M. A. Mueses, G. Li Puma, and F. Machuca-Martinez, "Synthesis of Mg-Al layered double hydroxides by electrocoagulation," *MethodsX*, vol. 5, pp. 915–923, 2018.

[35] J. Zhou, S. Yang, J. Yu, and Z. Shu, "Novel hollow microspheres of hierarchical zinc-aluminum layered double hydroxides and their enhanced adsorption capacity for phosphate in water," *Journal of Hazardous Materials*, vol. 192, no. 3, pp. 1114–1121, 2011.

[36] S. An, D. Kwon, J. Cho, and J. C. Jung, "Effect of the solvent on the basic properties of Mg–Al hydrotalcite catalysts for glucose isomerization," *Catalysts*, vol. 10, no. 11, p. 1236, 2020.

Hindawi
Journal of Nanomaterials
Volume 2021, Article ID 8493201, 9 pages
https://doi.org/10.1155/2021/8493201

Research Article

Study on Microstructure and Properties of the UV Curing Acrylic Epoxy/SiO_2 Nanocomposite Coating

Ngoc Linh Nguyen[1,2], **Thi My Linh Dang**[3], **Tuan Anh Nguyen**[3], **Hoang Thu Ha**[4] and **Thien Vuong Nguyen**[1,3]

[1]*Graduate University of Science and Technology, VAST, 18 Hoang Quoc Viet, Cau Giay, Hanoi, Vietnam*
[2]*Faculty of Pharmacy, Thanh Do University, Kim Chung, Hoai Duc, Hanoi, Vietnam*
[3]*Institute for Tropical Technology, VAST, 18 Hoang Quoc Viet, Cau Giay, Hanoi, Vietnam*
[4]*VNU-University of Education, Vietnam National University, Hanoi, Vietnam*

Correspondence should be addressed to Hoang Thu Ha; hoangthuhavnuued@gmail.com
and Thien Vuong Nguyen; vuongvast@gmail.com

Received 22 June 2021; Revised 12 August 2021; Accepted 1 October 2021; Published 29 October 2021

Academic Editor: Ester Vazquez

This study is aimed at exploring the effects of SiO_2 nanoparticles on the crosslinking and mechanical and thermal properties of UV curing acrylic epoxy coating. The curing polymerization process and thermal and mechanical properties of UV-curable acrylate epoxy system have been evaluated with or without the presence of SiO_2 nanoparticles. To fabricate the UV curing acrylic epoxy/SiO_2 nanocomposite coating, nano-SiO_2 particles (0.5–5 wt.% by weight of resin) were added in the photocurable system using sonication for 3 h. Various techniques for characterization have been used, such as FESEM (field emission scanning electron microscope), FTIR (Fourier-transform infrared spectroscopy), TGA (thermogravimetry analysis), gel fraction, and swelling degree analyses. FESEM data indicated that at the content of 2.5 wt.%, nanosilica was homogeneously dispersed in the coating procedure. However, once added 5 wt.%, large aggregation portions were found inside the coating matrices. Surprisingly, nano-SiO_2 could play dual roles, as both UV absorbers and nanoreinforcers, in this nanocomposite coating. Besides, data from FTIR, gel fraction, and swelling degree analyses confirmed the role of SiO_2 nanoparticles as UV absorbers that reduced the conversion performance of acrylate double bonds, thus increased slightly the swelling degree of coating. In addition, incorporation of SiO_2 nanoparticles (as nanofillers, at content of 2.5 wt.%) in the polymer matrix enhanced significantly the abrasion resistance and thermal stability of the coating, by 60% (from 98.3 to 158.4 lite/mil) and 9°C (from 348°C to 357°C), respectively.

1. Introduction

As can be processed at room temperature and organic solvent-free, acrylate resin-based UV curing paints exhibit many advantages, such as transparency, moisture resistance, chemical resistance, and environmental friendly. As reported, they have been widely applied to various finish surfaces, such as steel or wooden floors [1–5]. However, the main disadvantage of this resin system is the high curing shrinkage (up to 15%) [6, 7]. Its shrinkage could be enhanced by three pathways such as the following: (i) by selecting components (with suitable structure), (ii) by increasing the curing density, and (iii) by using fillers [7–12].

Nowadays, nanomaterials and nanotechnologies are extensively developed for emerging applications, such as nanoenergetic composites [13], propellant composite formulation [14], protein immobilization [15], microbial fuel cell [16], and microbial electrolysis cell [17]. In case of the coating technology, incorporation of inorganic nanoparticles, such as SiO_2 [18–20], ZnO [21–23], TiO_2 [24–26], Fe_3O_4 [27], and

nanohybrids [28–30] into the formulation of polymer materials, offers the significant enhancement of their properties when used for coating. By adding nanosilica in the coating process, the mechanical, thermal, and anticorrosion characteristics of the organic coatings were critically enhanced [31–36]. Nano-SiO_2 was employed for both superhydrophobicity coating [37–41] and hydrophilic coating [42].

However, the addition of nanoparticles (as nanofillers) can affect the curing reaction of thermoset resin systems depending on the nature and content of the nanoparticles. In the case of the epoxy matrix, Fe_3O_4 nanoparticles can act as a bridging link molecule, thereby reducing the total free mass and increasing the crosslinking density [43, 44]. In this direction, to study the healing dynamics of the epoxy/amine system, Fe_3O_4 nanoparticles were used as nanocontainers for loading the acid functional groups [45], amino functional groups [46, 47], or hydroxyl functional groups [46, 48]. The previous reported publications mentioned that the reaction between acidic groups and amine groups of curing agent can deactivate the hardener [45]. And the existence of hydroxyl and amine groups might boost the epoxy groups. It resulted to an increase in the content of thermal curing [46]. For example, Yari et al. investigated that nanosilica caused to an incomplete curing procedure of the acrylic melamine clearcoat, suggesting to a lower crosslinked density, as compared with the pure clearcoat and improved weathering capacity. It might be assumed that nano-SiO_2 absorbed the harmful incident UV rays, protecting the clearcoat against weathering degradation [49]. In our reported reviews [50], when conducting the curing reaction of acrylic polyols with isocyanate, we found that SiO_2 nanoparticles involved in reaction with isocyanate group to form a tight inorganic-organic hybrid structure. For UV curing systems, the degree of influence of additives depends not only on the content but also on their ability to absorb UV rays and photocatalytic activity. For Fe_3O_4-Ag hybrid nanoparticles, despite a strong UV absorption, their low content (0.1 wt.%) might not significantly affect the kinetics of curing reaction [51]. The organic UV absorber T384 reduced the efficiency of double bonds while nanoparticles absorb UV anatas-TiO_2 and ZnO increased the conversion of the acrylate groups of the system due to strong photocatalytic activity [52].

Although polymers/SiO_2 nanocomposites have been reported intensively in the literature, effect of nanoparticles on the kinetics of photo-curing process for UV curing acrylic epoxy resin system has not been well clarified. In this work, the photo-crosslinking polymerization process of the system of acrylate epoxy resin and 1.6 hexanediol diacrylate diluent in the presence of SiO_2 nanoparticles has been evaluated by using various techniques, such as the quantitative infrared analysis, relative hardness, gel fraction, and swelling degree measurements. In addition, the effect of SiO_2 nanoparticles on the mechanical and thermal properties of nanocomposite coating is evaluated.

2. Materials and Methods

2.1. Materials. All the chemicals were ordered from Sigma-Aldrich, such as Bisphenol A glycerolate dimethacrylate (BGDM) and 1,6-hecxanediol diacrylate 80% (HDDA). The photoinitiator 1-hydroxy-cyclohexyl-phenyl-ketone, Irgacure 184 (I.184) was obtained from CIBA (Merck). Their structures are shown in Figure 1. The used SiO_2 nanoparticles were self-synthesized according to the method presented in our previous article [50].

2.2. Preparation of Nanocomposite Coating. SiO_2 nanoparticles, at the contents from 0.5 to 5 wt.%, were firstly dispersed in HDDA by using a TPC-25 supersonic bath (Switzerland) for 3 h; then, these mixtures were mixed with E284 and I.184 by stirring in the Ika RW16 Basic Mixer (England) for 30 min. The ratio of E284 : HDDA : I.184 was 55 : 45 : 3.

Coatings with the thickness of ~25 μm were prepared on KBr pellets for IR spectral analysis, on Teflon sheets with the size of 100 × 100 × 10 mm for UV-Vis spectral, gel fraction, swelling degree, and FESEM analyses, on glass plates with the size of 100 × 100 × 2 mm for relative hardness and abrasion resistance tests by using a Quadruple Film Applicator Model 360. The coating process was applied for an UV radiation of a medium-pressure mercury lamp (250 mW/cm^2) at 25°C in an UV device, model F300S, USA. The product was conducted various times under the light with a web rate ranged of 5-40 m/s.

2.3. Methods for Characterization of Coatings

2.3.1. IR Spectral Analysis. Changes of IR absorption band at 983 cm^{-1} (=CH stretching) assigning to acrylate double bonds during the crosslinking reaction were quantitatively studied by using a FTIR spectroscopy NEXUS 670 from Nicolet. Experiments are carried out at the same position of each sample and after various time of UV exposure [51]. Benzene ring at 1510 cm^{-1} was selected as a band to eliminate the changes in the coating thickness.

The optical density (D) of groups was estimated by the following formula:

$$D = \log\left(\frac{I_0}{I}\right) = \log\left[1 + \frac{H}{(100 - U)}\right]. \quad (1)$$

The relationship between I_0 and I with H and U is shown in Figure 2 where H and U were calculated by using the software of FTIR spectroscopy.

Remaining acrylate group was calculated as follows:

$$\text{Remaining acrylate group (\%)} = \left[\frac{(D_{983\text{cm}^{-1}}/D_{1510\text{cm}^{-1}})_t}{(D_{983\text{cm}^{-1}}/D_{1510\text{cm}^{-1}})_0}\right] \times 100, \quad (2)$$

where D_0 and D_t are the optical densities of groups before and after curing.

2.3.2. Gel Fraction and Swelling Degree Analyses. Gel fraction and swelling degree analyses of coating product are conducted in Soxhlet tool in accordance with the ASTM (American Society for Testing and Materials) D 2765 [51]. Briefly, the dried coating was immersed in acetone solution for 24 h; then, the insoluble portion was dried at 50°C. The gel fraction is a weight ratio of insoluble portion and the initial coating.

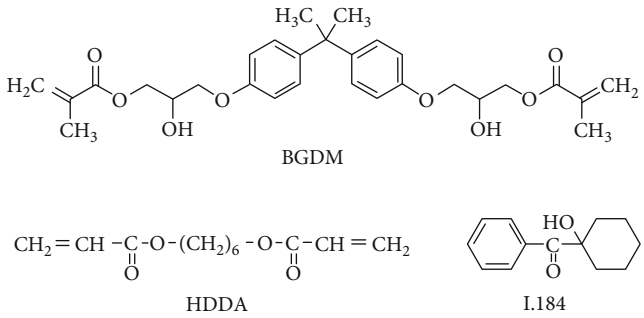

Figure 1: Chemical formula of Bisphenol A glycerolate dimethacrylate (BGDM), 1,6-hexanediol diacrylate (HDDA), and 1-hydroxy-cyclohexyl-phenyl-ketone (I.184).

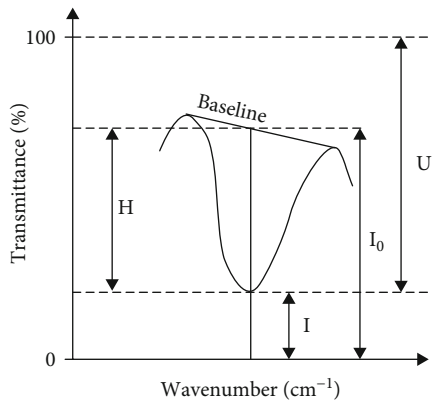

Figure 2: The relationship between I_0 and I with H and U.

Similarity, the swelling degree is a weight ratio of swollen film and the dried film.

2.3.3. Determination of Mechanical Resistance and Surface Morphology. The value of coating abrasion resistance was calculated by using abrasive falling methods, according to the ASTM D968 [28]. The value of relative hardness was determined on a Pendulum Damping Tester, model 300, according to the Persoz Standard, model NF T 30-016. It was calculated by the following equation:

$$\text{The relative hardness} = \frac{\text{absolute hardness of coating}}{425\ (425 \text{ was absolute hardness of standard glass})}. \quad (3)$$

The surface chemistry was observed in a scanning electron microscope (SEM-S-4800, Hitachi, Japan). To increase the electrical conductivity of products, their surface was covered by a carbon layer.

2.3.4. Thermal Analysis. Thermogravimetry experiments were performed using a well-equipped thermogravimetry analyzer (TGA-50, Shimadzu, Japan). The samples were heated in ranged of 25-600°C, at a rate of 10°C min^{-1} (under an argon atmosphere with a flow rate of 50 cm^3 min^{-1}).

3. Results and Discussions

3.1. IR Spectra Studies. IR spectra measurement has been used widely to evaluate the crosslinking process of UV-curable acrylate epoxy coating, thought the chemical conversion of acrylate double bonds [51, 52]. Figure 3 shows the IR spectra of the neat UV curing acrylate epoxy coating (UVAE) and the nanocomposite coating with 2.5 wt.% nano-SiO_2 (UVAE/SiO_2) before and after 9.6 s UV light exposure.

As shown in Figure 3, a decrease in intensity of the characteristic peaks (1636, 1409, 983, and 812 cm^{-1}) for =C-H stretching vibrations in acrylate groups was clearly observed after 9.6 s of UV exposure. Besides, the absorbance intensity of 1510 cm^{-1} band (=C-H stretching of aromatic ring) did not change after UV light exposure [51]. The peaks at 983 and 1510 cm^{-1} changed clearly but not overlapped with the neighboring bands. Therefore, the peak at 983 cm^{-1} was chosen to quantitatively evaluate the variation of the acrylate group during UV light irradiation exposure, whereas peaks at 1510 cm^{-1} can be used as the reference. Conversion of acrylate double bonds in the neat coating (UVAE) and the nanocomposite containing 2.5 wt.% nano-SiO_2 (UVAE/-SiO_2) during the UV light exposure process is presented in Figure 4. For the comparative study, we also added the conversion of acrylate double bonds in the acrylate urethane coating (UVAU) [50] in Figure 4.

As can be observed in Figure 4, the acrylate double bonds are conversed rapidly in the first 0.3 s of UV light exposure, and their conversion rate is reduced till 9.6 s of UV light exposure. Conversion of acrylate double bonds in the neat coating was higher than that in the nanocomposite. After 4.8 s of UV exposure, content of acrylate group conversed 87.3 and 81.6% in the neat coating and the nanocomposite, respectively. Further exposure to UV light irradiation could only improve slightly the conversion of acrylate double bonds. After 9.6 s of UV exposure, the content of acrylate groups conversed 89.4 and 85.0% in the neat coating and the nanocomposite, respectively.

It was reported in the literature that the photoinitiator was very sensitive to UV radiation [2, 51, 52]. Under UV light from a medium-pressure mercury lamp, photoinitiator I.184 was decomposed into the free radicals. Then, these free radicals reacted with acrylate double bonds, thus initiated photo-crosslinking polymerization reaction. Briefly, in the first 0.15 s of UV exposure, the content of photoinitiators was high (around 3%), and the curing system was relatively flexible (low viscosity). Therefore, the reaction of the acrylate double bonds was insignificantly affected by UV absorbers; however, the concentration of the photoinitiators and acrylate double bonds was reduced rapidly; thus, the conversion of the acrylate double bonds decreased.

This finding can be explained by the fact that nano-SiO_2 absorbed the UV light [20, 49, 50], leading to protect the photoinitiators from photon absorption. On the other hand, the conjugated double bonds of the benzene ring in BGDM that strongly absorb in the 270 nm wavelength region also prevent the UV energy absorption of the photoinitiators, which is a reason why the conversion performance of acrylate groups in this coating system (UV

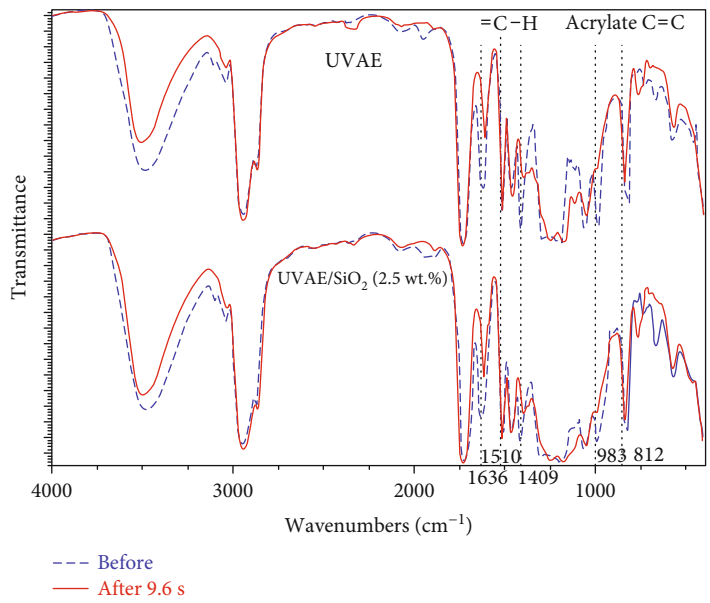

Figure 3: IR spectra of the neat UV curing acrylate epoxy coating (UVAE) and the nanocomposite (UVA/S_iO_2) before and after 9.6 s of UV light exposure.

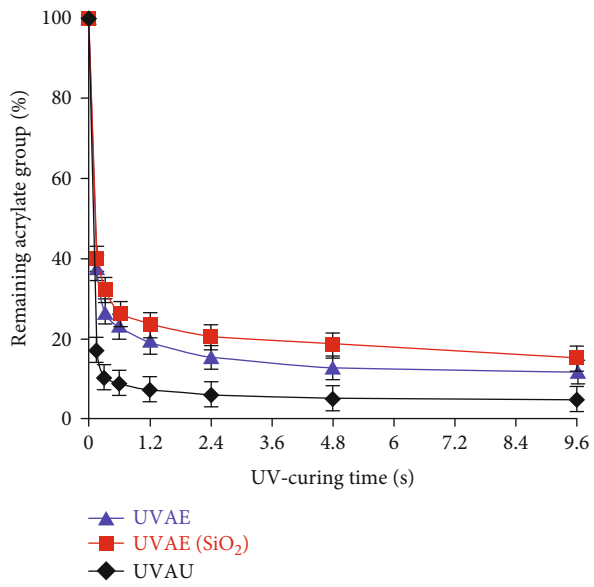

Figure 4: Conversation of acrylate double 2.5 wt.% S_iO_2 (UVAE/S_iO_2) during the UV exposure process.

curing acrylic epoxy resin) was lower than that in the UV curing acrylate urethane resin [52].

3.2. Gel Fraction and Swelling Degree Studies. Gel fraction and swelling degree were important parameters to evaluate the crosslinking of the thermoset resin. Figure 5 presents the variations of gel fraction and swelling degree of the neat coating and the nanocomposite with 2.5 wt.% nano-SiO_2 during the UV light exposure process. As shown, after 0.3 s of the reaction, the gel fraction of the coatings without and with 2.5 wt.% nano-SiO_2 appeared. The gel fraction increased, and the swelling degree reduced rapidly in the first 2.4 s, and after then, it slowed down. In the presence of 2.5 wt.% nano-SiO_2, the gel fraction decreased insignificantly, while its swelling degree increased slightly. After 4.8 s of the reaction, the gel fraction and swelling degree reached the maximum values of 95.5 and 365.2 (for the neat coating) and 95.0 and 380.4% (for the nanocomposite), respectively.

Thus, nano-SiO_2 did not affect to the gel fraction but affected slightly on the swelling of the coating. This obtained data could be explained by the fact that UV-absorbing nano-SiO_2 reduced the conversion efficiency of acrylate groups and did not significantly affect on the curing participation of BGDM resin and HDDA diluent but reduced slightly the crosslinking density of the coating so the gel fraction of the coating changed insignificantly, while its swelling increased slightly.

3.3. Coating Hardness Study. For thermoset resin systems, monitoring the hardness of system is also a simple and effective method to study the kinetics of curing reaction because during curing the resin system gradually changes from liquid to solid state and becomes stiffer over time. The changes in relative hardness of the neat coating and the nanocomposite containing 2.5 wt.% nano-SiO_2 during exposure to UV light radiation are presented in Figure 6. As can be seen in Figure 6, the hardness of the coatings increased rapidly in the first 1.2 UV exposure and then slowed down. After 4.8 seconds of the exposure, the hardness of the neat coating and the nanocomposite coating reached the maximum values of 0.91 and 0.89, respectively. The hardness of the coatings was not much different. The enhanced hardness of the coatings in the first stage of UV light exposure can be explained by the fast curing rate, due to the higher

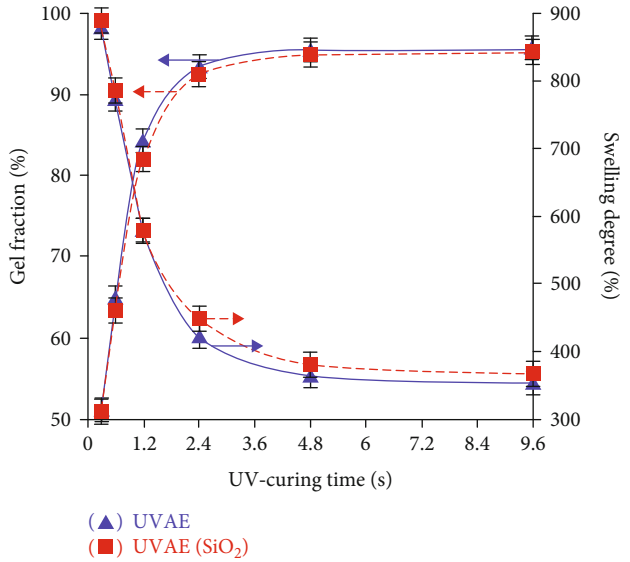

Figure 5: Variation of gel fraction and swelling degree of the neat coating (UVAE) and the nanocomposite with 2.5 wt.% nano-S_iO_2 during the UV exposure process.

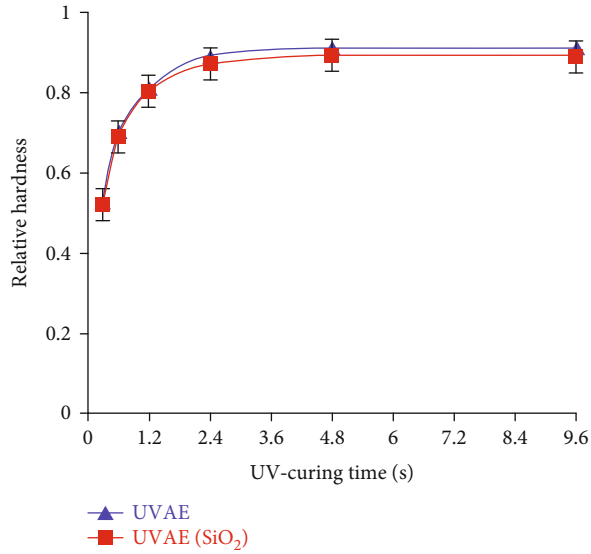

Figure 6: Variation of relative hardness of the neat coating (UVAE) and the nanocomposite with 2.5 wt.% nano-S_iO_2 during the UV light exposure.

concentrations of initiator and the acrylate group, as well as the higher coating flexibility. However, after 1.2 s of UV exposure, the initiator concentration was not much and the most of the acrylate double bonds has converted as well as the coatings were less flexible due to the high crosslinking density as shown in Figures 4 and 5 so the reaction rate slowed down resulting to that the hardness of the coatings increased also slowly.

Addition of 2.5 wt.% nano-SiO_2 into the coating matrix can make their structure became harder. However, it could

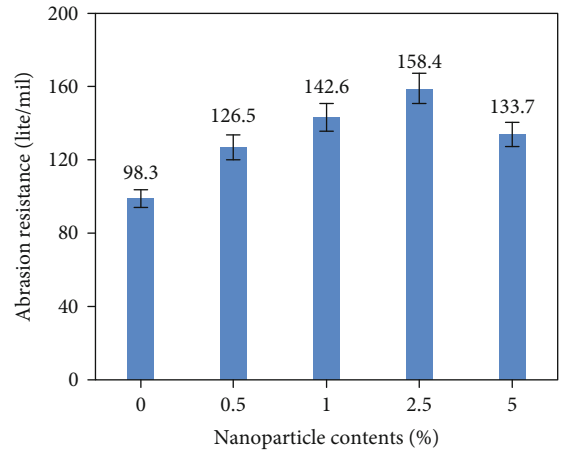

Figure 7: Influence of nano-S_iO_2 on the abrasion resistance of the coating.

also reduce the coating hardness due to the higher roughness of coating surface. These two contradictory impacts might compete with each other, leading to the slight variation in the coating hardness [51].

3.4. Coating Abrasion Resistance Study. SiO_2 nanoparticles have been used widely as nanofillers to enhance the abrasive resistance of polymer materials, due to their high hardness and abrasion resistance [49]. Figure 7 presents the effect of nano-SiO_2 contents on the abrasion resistance of the nanocomposite coating. As can be observed in Figure 7, abrasion resistance of the nanocoating increased with increasing the content of nano-SiO_2 (from 0 to 2.5 wt.%). In the introduction of 2.5 wt.% nanoparticles into the polymer matrix, the abrasion resistance of the coating increased 60% (from 98.3 to 158.4 lite/mil). However, when 5 wt.% nanoparticles were used, the abrasion resistance of the nanocoating was only 133.7 lite/mile (36% increase). Figure 8 was TEM (a) and FESEM (b) images of SiO_2 nanoparticles and the FESEM images of nanocomposite coatings with 2.5 wt.% and 5 wt.% of SiO_2 nanoparticles. Figures 8(a) and 8(b) present the FESEM and TEM images of SiO_2 nanoparticles. As can be seen in these figures, the average size of nano-SiO_2 is about 15 nm. Figures 8(c) and 8(d) are the FESEM images of nanocomposite coatings containing 2.5 and 5 wt.% of nanoparticles, respectively. In case that the content of nano-SiO_2 is 2.5 wt.%, FESEM image indicates that SiO_2 nanoparticles are homogeneously dispersed into the coatings (Figure 8(c)). In this case, these small nanoparticles could not only serve as nanofillers for the polymer matrix, but also actively participate in the polymer-curing process. We expect that these small nanoparticles can penetrate into small holes/indentation/capillaries in the polymer matrices and also can act as nuclei for the growth of crosslinking polymer networks. In case that the content of nano-SiO_2 is 2.5 wt.% is used, large aggregations (~0.5 μm in size) were found in the nanocomposite coating (Figure 8(d)). These aggregations might lead to reduce the mechanical property of the nanocomposite coating.

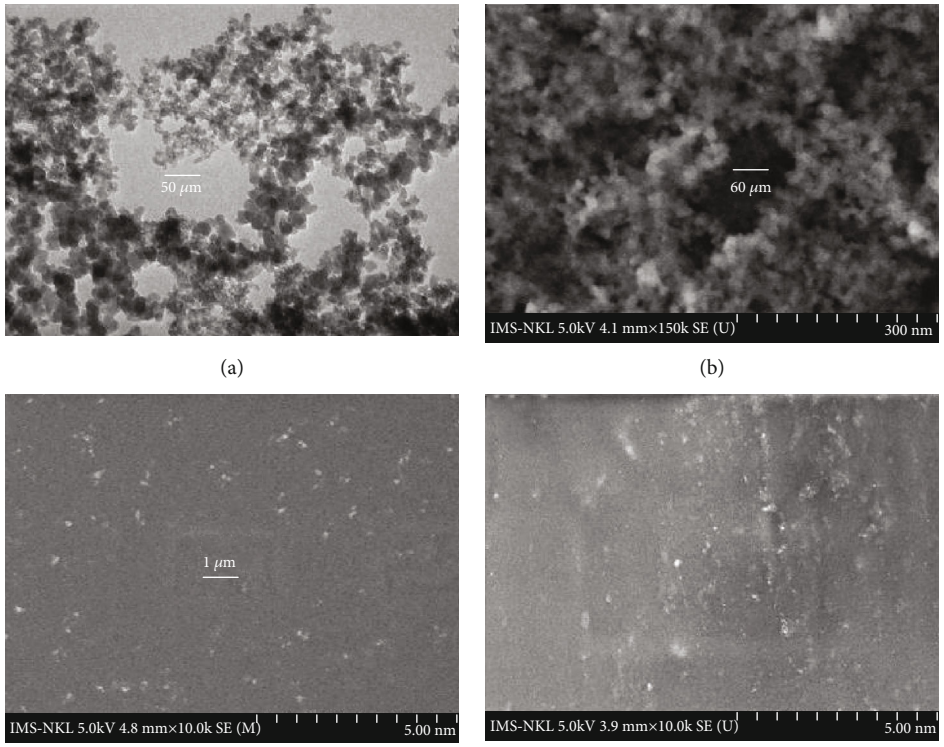

Figure 8: (a) TEM and (b) FESEM images of S_iO_2 nanoparticles and FESEM images of nanocomposite containing (c) 2.5 wt.% and (d) 5 wt.% nano-S_iO_2.

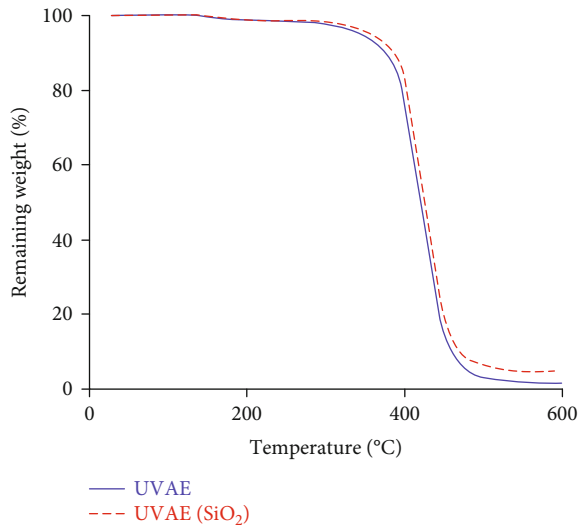

Figure 9: TGA curves of the neat coating and the nanocomposite coatings.

3.5. Study on Thermal Stability of Coating. Figure 9 is TGA curves of the neat coating and the nanocomposite coating with 2.5 wt.% nano-SiO_2. Table 1 shows the values of temperature at the weight loss of 5%, 50%, and 75% for the coating samples. The data from Figure 9 and Table 1 showed that the initial loss stage of the coatings with weight loss of 5% was observed around 345-360°C. The possible reason could be attributed to the release of both adsorbed water and low molecular organic substances. The $T_{5\%}$ (T_{initial}) of the neat coating and the nanocomposite with 2.5 wt.% nano-SiO_2 were 348 and 357°C. The $T_{5\%}$ increase of the coating (9°C) due to the presence of the nanoparticles could be interpreted in the terms of their role as thermal stabilizers. The stage of major weight loss of 50% occurred at

Table 1: Values of $T_{5\%}$, $T_{50\%}$, and $T_{75\%}$ for the neat and nanocomposite coatings.

Coatings	$T_{5\%}$ (°C) (5% loss in mass)	$T_{50\%}$ (°C) (50% loss in mass)	$T_{75\%}$ (°C) (75% loss in mass)
UVAE	348	420	440
UVAE/S_iO_2	357	425	445

420°C for the neat coating, and at 425°C for the nanocomposite was attributed to scission of backbone chain [25, 28] in acrylate urethane polymer matrix. The coatings lost 75% of its weight at the temperature of 440°C for the neat coating and 445°C for the nanocomposite.

As compared to the styrene acrylic polyurethane and acrylic emulsion coatings [25, 28], thermal stability of this nanocomposite coatings is higher. This finding can be explained by the higher crosslinking density and higher thermal resistance chemical bonds in this nanocomposite.

4. Conclusions

The effect of SiO_2 nanoparticles on the photo-crosslinking polymerization process of UV-curable acrylate epoxy system has been evaluated. Microstructure and properties of the UV curing acrylic epoxy/SiO_2 nanocomposite coating are also characterized.

The main findings of this study were as follows:

(i) FESEM images indicated that SiO_2 nanoparticles were homogeneously dispersed into the coatings, when used at the content of 2.5 wt.%. However, large aggregations were found in the nanocomposite coating with 5 wt.% nano-SiO_2

(ii) In the photo-crosslinking polymerization process, FTIR data indicated that nanoparticle reduced the conversion performance of acrylate double bonds, thus slightly increased the swelling degree of nanocomposite coating

(iii) Incorporation of SiO_2 nanoparticles into the coating matrix (as nanofillers, at content of 2.5 wt.%) enhanced significantly its abrasion resistance and thermal stability by 60% (from 98.3 to 158.4 lite/-mil) and 9°C (from 348°C to 357°C), respectively

(iv) In the UV curing acrylic epoxy/SiO_2 nanocomposite coating, SiO_2 nanoparticles can play dual roles, as both UV absorbers and nanoreinforcers

Data Availability

All the data and supporting materials are included within the article.

Conflicts of Interest

All authors declare that there are no conflicts of interest regarding the publication of this paper.

Acknowledgments

The paper is financially supported by the Graduate University of Science and Technology, Vietnam Academy of Science and Technology (GUST.STS.ĐT 2020-HH06).

References

[1] M. de Brito, X. Allonas, C. Croutxé-Barghorn, M. Palmieri, and I. Alig, "Kinetic study of photoinduced quasi-simultaneous interpenetrating polymer networks," *Progress in Organic Coatings*, vol. 73, no. 2–3, pp. 186–193, 2012.

[2] P. Nguyen-Tri, "Thien Vuong Nguyen, Radically Curable Nanobased Coatings (chapter 10)," in *Nanomaterials Based Coatings*, P. N. Tri, S. Rtimi, and C. Ouellet-Plamondon, Eds., pp. 339–372, Elsevier, 2019.

[3] L. X. Hien, N. T. Vuong, L. M. Thuy, and N. T. V. Trieu, "Study of photocrosslinking reaction of the resin system on the base of copolymer of tung and soyabean oils, methyl methacrylate, styrene," *Journal of Science and Technology*, vol. 48, no. 3A, pp. 150–157, 2010.

[4] N. T. Vuong, Đ. P. Hung, N. A. Hiep, M. Van Phuc, T. Van Thanh, and Đ. T. Lien, "Degradation of Primal AC-261 acrylic emulsion in the artificial weathering environment," *Journal of Science and Technology*, vol. 53, no. 3, pp. 317–321, 2015.

[5] T. V. Nguyen, X. H. Le, P. H. Dao, C. Decker, and T. P. Nguyen, "Stability of acrylic polyurethane coatings under accelerated aging tests and natural outdoor exposure: the critical role of the used photo-stabilizers," *Progress in Organic Coatings*, vol. 124, pp. 137–146, 2018.

[6] M. Sangermano, W. Carbonaro, G. Malucelli, and A. Priola, "UV-cured interpenetrating acrylic epoxy polymer networks: preparation and characterization," *Macromolecular Materials and Engineering*, vol. 293, no. 6, pp. 515–520, 2008.

[7] C. Rocco, F. Karasu, C. Croutxé-Barghorn, X. Allonas, and G. de With, "Highly-interpenetrated and phase-separated UV-cured interpenetrating methacrylate–epoxide polymer networks: influence of the composition on properties and microstructure," *Materials Today Communications*, vol. 6, pp. 17–27, 2016.

[8] T. A. T. Canellas, A. de Almeida Neves, I. K. B. dos Santos, A. R. P. de Rezende, and E. M. da Silva, "Characterization of low-shrinkage dental composites containing methacrylethyl-polyhedral oligomeric silsesquioxane (ME-POSS)," *Journal of the Mechanical Behavior of Biomedical Materials*, vol. 90, pp. 566–574, 2019.

[9] S. Garoushi, P. K. Vallittu, D. C. Watts, and L. V. J. Lassila, "Effect of nanofiller fractions and temperature on polymerization shrinkage on glass fiber reinforced filling material," *Dental Materials*, vol. 24, no. 5, pp. 606–610, 2008.

[10] M. Tafesse and H.-K. Kim, "The role of carbon nanotube on hydration kinetics and shrinkage of cement composite," *Composites Part B: Engineering*, vol. 169, no. 15, pp. 55–64, 2019.

[11] B. Pratap, R. K. Gupta, B. Bhardwaj, and M. Nag, "Modeling based experimental investigation on polymerization shrinkage and micro-hardness of nano alumina filled resin based dental material," *Journal of the Mechanical Behavior of Biomedical Materials*, vol. 99, pp. 86–92, 2019.

[12] S.-J. Lee, S. Kawashima, K.-J. Kim, S.-K. Woo, and J.-P. Won, "Shrinkage characteristics and strength recovery of nanomaterials-cement composites," *Composite Structures*, vol. 202, no. 15, pp. 559–565, 2018.

[13] D. Kumar, K. D. B. Yamajala, A. B. Samui, and S. Banerjee, "Tailoring of energetic groups in acroyloyl polymers," *Designed Monomers and Polymers*, vol. 20, no. 1, pp. 332–343, 2017.

[14] D. Kumar, H. Singh, M. Maurya et al., "Novel evaluation enhancement role of poly (1-(3-nitrophenyl)-1H-1, 2, 3-triazol-4-yl) acrylate materials for propellant composite formulation," *Materials Letters*, vol. 280, p. 128585, 2020.

[15] S. Singh, A. Singh, V. S. S. Bais, B. Prakash, and N. Verma, "Multi-scale carbon micro/nanofibers-based adsorbents for protein immobilization," *Materials Science and Engineering: C*, vol. 38, pp. 46–54, 2014.

[16] S. Singh, A. Modi, and N. Verma, "Enhanced power generation using a novel polymer-coated nanoparticles dispersed-carbon micro-nanofibers-based air-cathode in a membraneless single chamber microbial fuel cell," *International Journal of Hydrogen Energy*, vol. 41, pp. 1237–1247, 2016.

[17] A. Pophali and N. V. ShivSingh, "Simultaneous hydrogen generation and COD reduction in a photoanode-based microbial electrolysis cell," *International Journal of Hydrogen Energy*, vol. 45, no. 48, pp. 25985–25995, 2020.

[18] T. A. Nguyen, T. H. Nguyen, T. V. Nguyen, H. Thai, and X. Shi, "Effect of nanoparticles on the thermal and mechanical properties of epoxy coatings," *Journal of Nanoscience and Nanotechnology*, vol. 16, pp. 9874–9881, 2016.

[19] P. H. Dao, T. V. Nguyen, M. H. Dang et al., "Effect of silica nanoparticles on properties of coatings based on acrylic emulsion resin," *Vietnam Journal of Science and Technology*, vol. 56, no. 3B, pp. 117–125, 2018.

[20] T. V. Nguyen, T. A. Nguyen, and T. H. Nguyen, "The synergistic effects of SiO2 nanoparticles and organic photostabilizers for enhanced weathering resistance of acrylic polyurethane coating," *Journal of Composites Science*, vol. 4, no. 1, p. 23, 2020.

[21] T. V. Nguyen, P. H. Dao, T. A. Nguyen et al., "Photocatalytic degradation and heat reflectance recovery of water-borne acrylic polymer/ZnO nanocomposite coating," *Journal of Applied Polymer Science*, vol. 137, no. 37, article e49116, 2020.

[22] V. Tien Viet, T. V. Nguyen, M. Tabish et al., "Water-borne ZnO/acrylic nanocoating: fabrication, characterization, and properties," *Polymers*, vol. 13, no. 5, p. 717, 2021.

[23] T. V. Nguyen, P. H. Dao, K. L. Duong et al., "Effect of R-TiO2 and ZnO nanoparticles on the UV-shielding efficiency of water-borne acrylic coating," *Progress in Organic Coatings*, vol. 110, pp. 114–121, 2017.

[24] T. V. Nguyen, T. P. Nguyen, T. D. Nguyen, R. Aidani, V. T. Trinh, and C. Decker, "Accelerated degradation of water borne acrylic nanocomposites used outdoor protective coatings," *Polymer Degradation and Stability*, vol. 128, pp. 65–76, 2016.

[25] P. H. Dao, T. V. Nguyen, T. A. Nguyen et al., "Acrylic polymer/TiO2 nanocomposite coatings: mechanism for photodegradation and solar heat reflective recovery," *Materials Chemistry and Physics*, vol. 272, article 124984, 2021.

[26] T. V. Nguyen, T. A. Nguyen, P. H. Dao et al., "Effect of rutile titania dioxide nanoparticles on the mechanical property, thermal stability, weathering resistance and antibacterial property of styrene acrylic polyurethane coating," *Advances in Natural Sciences: Nanoscience and Nanotechnology*, vol. 7, no. 4, pp. 045015–045024, 2016.

[27] M. Jouyandeh, N. Rahmati, E. Movahedifar et al., "Properties of nano-Fe3O4 incorporated epoxy coatings from Cure Index perspective," *Progress in Organic Coatings*, vol. 133, pp. 220–228, 2019.

[28] T. T. Le, T. V. Nguyen, T. A. Nguyen et al., "Thermal, mechanical and antibacterial properties of water-based acrylic polymer/SiO2-Ag nanocomposite coating," *Journal of Materials Chemistry and Physics*, vol. 232, pp. 362–366, 2019.

[29] T. D. Ngo, T. M. H. le, T. H. Nguyen et al., "Antibacterial Nanocomposites Based on Fe3O4–Ag Hybrid Nanoparticles and Natural Rubber-Polyethylene Blends," *International Journal of Polymer Science*, vol. 2016, Article ID 7478161, 9 pages, 2016.

[30] T. N. L. Nguyen, T. V. Do, T. V. Nguyen et al., "Antimicrobial activity of acrylic polyurethane/Fe3O4-Ag nanocomposite coating," *Progress in Organic Coatings*, vol. 132, pp. 15–20, 2019.

[31] A. Allahverdi, M. Ehsani, H. Janpour, and S. Ahmadi, "The effect of nanosilica on mechanical, thermal and morphological properties of epoxy coating," *Progress in Organic Coatings*, vol. 75, no. 4, pp. 543–548, 2012.

[32] X. Shi, T. A. Nguyen, Z. Suo, Y. Liu, and R. Avci, "Effect of nanoparticles on the anticorrosion and mechanical properties of epoxy coating," *Surface and Coatings Technology*, vol. 204, no. 3, pp. 237–245, 2009.

[33] E. Amerio, P. Fabbri, G. Malucelli, M. Messori, M. Sangermano, and R. Taurino, "Scratch resistance of nanosilica reinforced acrylic coatings," *Progress in Organic Coatings*, vol. 62, no. 2, pp. 129–133, 2008.

[34] F. Bauer, R. Flyunt, K. C. H. Langguth, R. Mehnert, R. Schubert, and M. R. Buchmeiser, "UV curing and matting of acrylate coatings reinforced by nano-silica and microcorundum particles," *Progress in Organic Coatings*, vol. 60, no. 2, pp. 121–126, 2007.

[35] S. Maganty, M. P. C. Roma, S. J. Meschter et al., "Enhanced mechanical properties of polyurethane composite coatings through nanosilica addition," *Progress in Organic Coatings*, vol. 90, pp. 243–251, 2016.

[36] Y. C. Ching and N. Syamimie, "Effect of nanosilica filled polyurethane composite coating on polypropylene substrate," *Journal of Nanomaterials*, vol. 2013, Article ID 567908, 8 pages, 2013.

[37] M. U. M. Junaidi, S. A. Haji Azaman, N. N. R. Ahmad et al., "Superhydrophobic coating of silica with photoluminescence properties synthesized from rice husk ash," *Progress in Organic Coatings*, vol. 111, pp. 29–37, 2017.

[38] A. Madhan Kumar, S. S. Latthe, P. Sudhagar, I. B. Obot, and Z. M. Gasem, "In-situ synthesis of hydrophobic SiO2-PMMA composite for surface protective coatings: experimental and quantum chemical analysis," *Polymer*, vol. 77, pp. 79–86, 2015.

[39] G. Wu, J. C. Di Liu, G. Liu, and Z. Kong, "Preparation and properties of super hydrophobic films from siloxane-modified two-component waterborne polyurethane and hydrophobic nano SiO2," *Progress in Organic Coatings*, vol. 127, pp. 80–87, 2019.

[40] S. Ammar, K. Ramesh, I. A. W. Ma, Z. Farah, and A. K. Arof, "Studies on SiO2-hybrid polymeric nanocomposite coatings with superior corrosion protection and hydrophobicity," *Surface and Coatings Technology*, vol. 324, pp. 536–545, 2017.

[41] H. Chen, X. Zhang, P. Zhang, and Z. Zhang, "Facile approach in fabricating superhydrophobic SiO2/polymer nanocomposite coating," *Applied Surface Science*, vol. 261, pp. 628–632, 2012.

[42] B. Lin and S. Zhou, "Poly (ethylene glycol)-grafted silica nanoparticles for highly hydrophilic acrylic-based polyurethane coatings," *Progress in Organic Coatings*, vol. 106, pp. 145–154, 2017.

[43] N. Huong, *Improvement of Bearing Strength of Laminated Composites by Nanoclay and Z-Pin Reinforcement, [Ph.D. thesis]*, University of New South Wales, Australia, 2006.

[44] O. Becker, R. Varley, and G. Simon, "Morphology, thermal relaxations and mechanical properties of layered silicate nanocomposites based upon high-functionality epoxy resins," *Polymer*, vol. 43, no. 16, pp. 4365–4373, 2002.

[45] M. Jouyandeh, M. Shabanian, M. Khaleghi et al., "Acid-aided epoxy-amine curing reaction as reflected in epoxy/Fe3O4 nanocomposites: chemistry, mechanism, and fracture behavior," *Progress in Organic Coatings*, vol. 125, pp. 384–392, 2018.

[46] M. Jouyandeh, S. M. R. Paran, M. Shabanian et al., "Curing behavior of epoxy/Fe3O4 nanocomposites: a comparison between the effects of bare Fe3O4, Fe3O4/SiO2/chitosan and Fe3O4/SiO2/chitosan/imide/phenylalanine-modified nanofillers," *Progress in Organic Coatings*, vol. 123, pp. 10–19, 2018.

[47] M. R. Saeb, M. Nonahal, H. Rastin et al., "Calorimetric analysis and molecular dynamics simulation of cure kinetics of epoxy/-chitosan-modified Fe3O4 nanocomposites," *Progress in Organic Coatings*, vol. 112, pp. 176–186, 2017.

[48] M. R. Saeb, H. Rastin, M. Shabanian, M. Ghaffari, and G. Bahlakeh, "Cure kinetics of epoxy/β-cyclodextrin-functionalized Fe3O4 nanocomposites: Experimental analysis, mathematical modeling, and molecular dynamics simulation," *Progress in Organic Coatings*, vol. 110, pp. 172–181, 2017.

[49] H. Yari, S. Moradian, and N. Tahmasebi, "The weathering performance of acrylic melamine automotive clearcoats containing hydrophobic nanosilica," *Journal of Coating Technology and Research*, vol. 11, no. 3, pp. 351–360, 2014.

[50] T. M. A. Bui, N. T. Vuong, N. T. Mai et al., "Crosslinking mechanism, mechanical properties and weathering degradation of acrylic polyurethane nanocomposite coating reinforced by SiO2 nanoparticles issued from rice husk ash," *Materials Chemistry and Physics*, vol. 241, p. 122445, 2020.

[51] N. T. Vuong, D. T. Vy, H. M. Hung et al., "Crosslinking process, mechanical and antibacterial properties of UV-curable acrylate/Fe3O4-Ag nanocomposite coating," *Progress in Organic Coatings*, vol. 139, article 105325, 2020.

[52] N. T. Vuong, N. T. Phuong, A. Sohrab et al., "The role of organic and inorganic UV-absorbents on photopolymerization and mechanical properties of acrylate-urethane coating," *Materials Today Communications*, vol. 22, article 100780, 2020.

Hindawi
Journal of Nanomaterials
Volume 2021, Article ID 5801913, 13 pages
https://doi.org/10.1155/2021/5801913

Research Article

Agricultural Restructure Policy in Vietnam and Practical Application for Sustainable Development in Agriculture

Vinh Bao Ngoc,[1] **Nguyen Manh Hung**,[2] **and Phuong Thu Pham**[1]

[1]*VNU University of Economics and Business, Vietnam National University, Hanoi, Vietnam*
[2]*Ho Chi Minh National Academy of Politics, Hanoi, Vietnam*

Correspondence should be addressed to Vinh Bao Ngoc; vinhbaongocvnu@gmail.com

Received 24 May 2021; Revised 28 July 2021; Accepted 20 August 2021; Published 17 September 2021

Academic Editor: Ajit Kumar Sharma

The Vietnam's agricultural sector had to challenge with its course and learned lessons of further development. Novel policy might be adopted to encourage the private investments and sectors in agriculture. Furthermore, an introduction of new models such as climate-smart or green agriculture and application of modern technology increased productivity at the same time and creating jobs for millions of agricultural workers and reversing the massive rural-urban migration flux. Vietnam's agricultural sector needs to maintain the reform momentum, particularly liberalization policy, and to boost up agricultural potential. Obstacles such as land limitation policy must be removed to enable large-scale production and encourage private investment in the agricultural sector. To avoid being trapped by its own success, Vietnam is now shifting the old development paradigm that focuses too much on the quantity to the quality of the agricultural production. The government makes major efforts to achieve at the same time agricultural growth, better livelihood of the farmer, and the development of the rural areas. However, Vietnam still needs to prepare a "transition strategy" to overcome the impact of the technological progress on the traditional agricultural workers.

1. Introduction

1.1. Application and Role of Nanotechnology in Agricultural Systems. Nanomaterials are typically two- or three-dimensional materials, of which at least one dimension is nanometers (nm). Thus, nanomaterials can exist in three states: solid, liquid, and gas, in which solid nanomaterials are being studied the most, especially in the field of application in the agricultural system of developing countries such as Vietnam [1–3]. The concept of nanotechnology was first introduced in 1959 by the famous physicist Richard Feynman. Nanotechnology is defined as the specialization of materials at atomic, molecular, and supramolecular sizes. A more specific definition of nanotechnology is given by the American Association of Nanotechnology, according to which nanotechnology is the specialization of materials with a minimum size of 1-100 nanometers (1 billion nanometers is equal to 1 m) [4–6]. Nanotechnology is one of the most important tools in modern agricultural architecture. Nanotechnology in agriculture will become the economic engine of countries in the near future. Sustainable agrifood topics focus on sustainability and protection of agriculturally produced foods, including crops for human consumption and animal feed [7, 8]. Nanotechnology offers new chemical agents and new delivery mechanisms to improve crop yields. This promises to reduce the amount of pesticide use in agricultural production. Nanotechnology can boost agricultural production, and its broad applications include as can be seen in Figure 1 [9, 10]:

(i) In agrochemicals for application in pesticides and fertilizers for crop improvement

(ii) Application of nanotechnology in crop protection to identify diseases and residues of agrochemicals

(iii) Means for genetic manipulation of plants

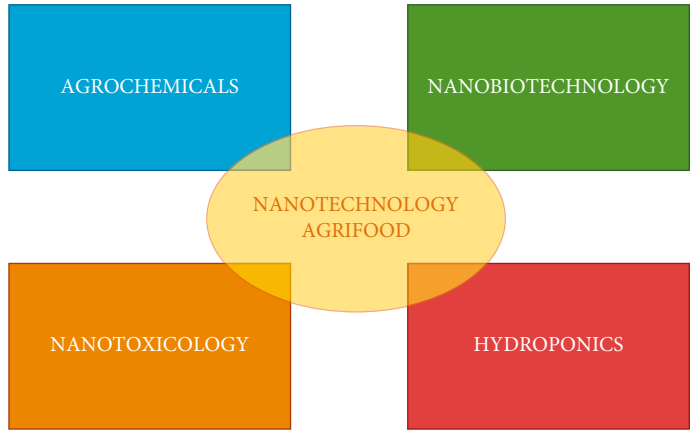

Figure 1: Nanotechnology in agricultural activities.

(iv) Diagnosis of plant diseases

(v) Animal health, animal husbandry, and poultry production

(vi) Postharvest management

1.1.1. Nanotechnology and Nanomaterial in the Treatment of the Growing Environment. The overuse of pesticides, herbicides, and insecticides in crop production has resulted in an issue of uncontrolled treatment of unwanted solid toxic wastes in chemical herbicides and insecticides to human natural ecosystems. Nanomaterials were regarded as a promising material to enhance crop production and remediate soil and groundwater pollution. Through recent reports on the application of nanotechnology in agricultural environments, researches have indicated that the overuse of nanomaterials to improve the quality of the environment helps detect and remediates pollution in different areas [4].

1.1.2. Nanotechnology in Crop Yield and Quality of Agricultural Products. Pesticides, herbicides, and insecticides play a very important role in agricultural production and development. However, the abuse of their chemicals had caused serious consequences for the natural ecosystems, adversely affecting the water and soil, affecting the quality and safety of agricultural products, and affecting human health. Nanomaterials allowed us to create integrated nanoproducts that helped plants grow and well develop and improved yield and quality of agricultural products [11]. Additionally, their chemicals helped plants increase resistance, thereby significantly reducing the amount of chemical fertilizers and pesticides used in cultivation, reducing environmental pollution, and contributing to sustainable agricultural development.

1.2. Agricultural Development in Vietnam. For over the past 30 years of economic reforms (Doi Moi), Vietnam has gained major achievement in agricultural development. Thanks are due to the liberalization policy, from a net food-imported country [12]. Vietnam has become among the top exporters of many agricultural products such as rice, coffee, and pepper. Millions of people in the rural areas have been lifted out of chronicle poverty and hunger. The face of the rural areas has been progressively changed. Vietnam's successful efforts in hunger eradication and poverty alleviation were highly appreciated by the donor community, including the development organizations such as the World Bank, Asian Development Bank, and the United Nations Development Program [13–15]. Restructure is a major topic of agricultural policy research in Vietnam. Despite major achievement in the Doi Moi (renovation), Vietnamese agricultural has been facing prolonged bottlenecks that are not easily overcome in a short period of time. The XII National Party Congress has issued policy guidelines to promote the agricultural development, focusing on the restructure of the sector to achieve productivity, efficiency, and quality. This article provides initial analysis of the restructure program, identifies the development vision of Vietnam's agricultural sector, and points out the key measures to be taken in the coming years to accelerate the agricultural restructure process [16, 17].

1.3. Role of Nanoparticles in Pesticides and Herbicides in Agricultural Activities. Nanotechnology is one of the most important tools of modern agricultural science, in which nanotechnology in the field of agrifood is predicted to become a driving force in the global economy in the future [3, 4, 18–22]. The rapid development of nanotechnology today is an objective process, reflecting the process of continuous improvement scientific and technical customs and changing technological habits. The advanced countries in recent decades in the field of trace fertilizers have made a technological leap: the traditional trace fertilizers have been replaced (rapidly) by new-generation preparations in the form of nanoparticles. Micronutrients ensure a high yield, while input costs are significantly reduced. It is known that in the US each year, the agricultural industry invests about 1 billion dollars in the application of nanotechnology in the cultivation, animal husbandry, and veterinary industries to earn nearly 20 billion dollars in profits from food production in nanoscale. Some countries in Europe and Asia also invest a lot of money in the nanoindustry.

Nanoparticles have a great potential for applications in agriculture with the following tasks:

(i) Seed treatment improves germination and growth rate, quality, and yield of products

(ii) Make foliar fertilizers including necessary trace elements in each stage of plant growth

(iii) Improve the efficiency of fertilizer use by applying controlled slow-release fertilizers

(iv) Improve use efficiency and reduce pesticide costs by developing methods of delivering nutrients and drugs to their destination

2. Vietnam's Agricultural Reforms since the Beginning of Doi Moi

Vietnam is located in the tropical region and has a huge potential for agricultural production. However, before the 1990s, the country used to face food shortages and food security was the major concern. There have been profound lessons learned from the past policy changes. In the period of 1953-1956, the state implemented land reforms, with the slogan "the plow has the land", by confiscating land of the landlords and dividing equally to farmers. In the period 1959-1960, to create agricultural cooperatives, the state then collected land of farming households and put it under the cooperatives to have a large field. These divisions and accumulations of land have created a great deal of disturbance in the way of organizing agricultural production and rural economy. The central planning mechanism, in particular, the model of agricultural cooperatives, a popular mode of farming production before Doi Moi, has not worked effectively because it eliminates the production motivation of farmers. The details of data and information are indicated in Tables 1 and 2.

2.1. Vietnam's Agricultural Reforms Have Undergone Three Major Stages of Development: "Crossing the Hunger" (1986-1988). Agriculture is known as the starting point of the economic reforms (Doi Moi) in the mid-1980s. Doi Moi in the agricultural sector has three main components [23]: (i) Farmers were given land use rights on the longer-term basis. In addition, they were also allowed to own other means of agricultural production. (ii) Farmer households became self-supporting economic units. Farmers were responsible for their production activities, from the cultivation to the sale of their products. (iii) The cooperatives served only as service providers (irrigation, electricity, and plant protection) and received fees from farmers who purchased those services.

In 1988, the Politburo promulgated Resolution 10 which is perceived today as the major breakthrough of land reform, initiating the institution of private property in agricultural and rural development. The resolution consisted of transferring control and cash-flow rights from the farming cooperative to the individual household. Land was allocated to households with 10-15 years of secure tenure. Farmers were given more power to manage the main inputs, make production decisions, and use their output. Nonetheless, the policy and institutional reforms in this period were pilot ones and focused only on production and distribution. These efforts were just sufficient to transform a collective economy to a household economy. Agricultural market had not fully emerged because the government still monopolized foreign trade; private sectors were allowed develop, but critical industries were still controlled by the government. Without the possibility to trade land use rights, land market did not develop. Credit market for agricultural production did not form because there was still one-tier banking system. In 1987 and in 1988, there was still hyperinflation at a three-digit level and unfavorable weather caused harvest loss and a fall of food output, leading to continued food shortage.

2.2. Extensive Commercial and Export-Oriented Production (1989-2000). After 1988, there was a rapid transition from self-sufficient to commercial agriculture production. The reforms of foreign trade pushed the export-oriented activities, including the export of agriculture sector. In 1989, the banking reforms occurred to help channel credit to the rural market. The monobanking system was transformed into a two-tier banking system, providing a more level playing field for credit institutions, contributing the resources to the agricultural development. The monopoly of the foreign trade was gradually lifted. During the period 1995-1999, Vietnam had taken active regional and multilateral economic integration as well as bilateral economic ties to enlarge its foreign market [24]. As a result, agricultural exports and export price increased; import price decreased. In the 1990s, rice market was liberalized gradually. Private sector began to take part in both retail and wholesale distribution system. Import and export activities became more competitive. Since March 1997, quota allocation has been decentralized so that all individuals and private companies are able to participate in rice export. The 1993 land law granted five rights to the households that unleash the motivation of farmers: the right to transfer, exchange, inherit, rent, and mortgage. The law extended the lease term to 20 years for annual crop land and 50 years for perennial crop land and provided the land use certificates. The reform of cooperatives and agricultural cooperative groups in 1989-1995 focused on two aspects: (i) Collectivization of land and other basic production inputs was abrogated in conformity with Resolution 10 and Land Law 1993. (ii) Agricultural cooperatives were directed to transforming functions, tenor, and ways of operation. Many weak cooperatives were dissolved or transformed to other forms in line with the market-oriented economy.

The important role for the private sector was further recognized and this created a boost in agricultural investment. In 1990, the Private Enterprises Law provided a legal basis for the establishment of sole proprietorships and the Company Law opened up for the establishment of new forms of enterprises such as limited liability and joint-stock companies. In 1992, the new Constitution officially recognized the role of the private sector. The decade of 1990 was the critical period of agriculture development as the sector switched from self-sufficed to commodity production. In 1989, food output reached 21 million tons and this was also the first year that Vietnam exported rice after a long time of being net rice importer [25]. Food has been secured, and rice monoculture was broken. During 1989-1999, productivity

Table 1: GDP and structure of agriculture in the period 2006-2017 (actual prices).

Year	Industry GDP (billion VND)	Net agricultural structure (%)	Structure of seafood (%)	Forestry structure (%)
2006	198.266	75.27	19.29	5.44
2007	232.188	74.97	19.83	5.20
2008	326.505	78.79	17.89	3.32
2009	346.786	78.54	17.81	3.65
2010	405.778	78.35	17.97	1.44
2011	558.284	79.09	17.81	3.10
2012	638.368	77.63	19.10	3.26
2013	658.779	76.44	19.92	3.64
2014	696.969	74.68	21.37	3.95
2015	712.460	74.90	20.76	4.34
2016	734.841	75.61	19.98	4.41
2017	768.212	72.86	22.32	4.82

Table 2: Comparison of labor productivity in the agricultural sector with other economic sectors (2001-2015) at comparative prices (2010).

Year	Agricultural labor productivity (million VND/labor)	Coefficient of agricultural labor productivity compared to other economic sectors (%)		
		Overall average	Construction industry	Service
2001	12.66	40.00	16.18	25.17
2002	13.20	40.33	17.18	26.07
2003	13.63	40.08	18.20	25.98
2004	14.11	39.70	18.27	26.36
2005	14.55	39.16	18.07	26.54
2006	15.24	38.56	18.36	25.97
2007	15.46	38.38	18.98	26.08
2008	15.95	38.53	19.73	25.93
2009	16.04	37.77	19.92	25.23
2010	16.33	37.13	24.21	22.17
2011	16.97	37.27	24.38	22.87
2012	17.47	37.23	23.75	23.81
2013	17.90	36.73	23.56	23.66
2014	18.50	36.20	23.19	23.48
2015	19.89	36.54	24.45	24.32

of many crops and animal husbandry increased [26]. The comprehensive and relatively development of the agricultural sector has raised the income of rural households, brought down the poverty rate in the rural areas [27], and contributed significantly to the development of household economy, farm economy, and private economy. The 8th National Party Congress in 1996 issued the guideline "developing rural industrialization and modernization" as to recognize the major achievement in the agricultural sector and rural economy.

2.3. Intensive Development (2000-2010). Since 2000, Vietnam's agriculture has entered the new phase of shifting from extensive to intensive production, aiming at higher productivity and quality. This is also a new period of Vietnam's international economic integration. On January 11th 2007, Vietnam officially became the WTO member [28]. Following the WTO accession, the Vietnam-US Trade and Investment Framework Agreement (TIFA), signed on June 22, 2007, was regarded as the manifestation of the two countries' successful cooperation. The Vietnam-Japan Economic Partnership Agreement (VJEPA) has also come into effect since October 1st 2009. The party and the government have issued several important guidelines and policies on agricultural development such as Resolution 09/NQ/CP of the Government about the agricultural production and consumption structure transference (15/06/2000), Resolution 03-NQ/CP of the Government about the farm economy (2/2/2000), and especially Party Central Committee's Resolution 5 (2/3/2002) on hastening industrialization and modernization of agriculture and rural area in 2001-2010. Resolution 5 cleared the way for the establishment of various agricultural development programs in poverty alleviation, varieties, technological cooperation, clean water, and environmental

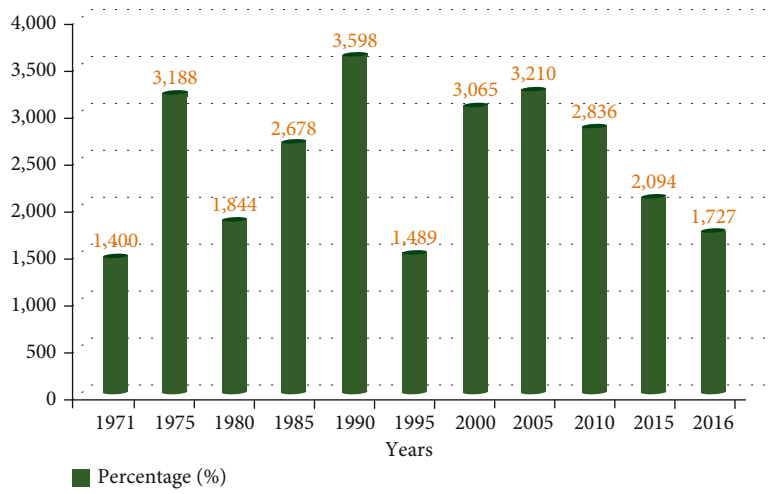

Figure 2: Growth rate of world agriculture in the period 1971-2016 (%).

safety [3, 29]. In 2008, the Central Party Committee issued Resolution No. 26 on "agriculture, farmers and rural area", which again emphasizes the strategic role of "agriculture, farmers and rural area" in industrialization and modernization. As the result of liberalization, household economy has developed farm production and nonstate sectors account for 96 percent of agricultural GDP. Agricultural output has continuously expanded. Increasing competition especially in the export market has made product quality greatly improved, leading to the increase of export value. In the Mekong Delta, the main rice basket of Vietnam, about 80 percent of the rice planting area is grown from high-quality seeds [30]. In the context of policy and market changes, there are profound transformations in role and development of farming households, state-owned enterprises, private enterprises, and cooperatives which are major stakeholders in agriculture production. Before Doi Moi, cooperatives and state-owned enterprises had controlled agriculture production and rural livelihood. The reforms of the agricultural sector have made farming households the main stakeholder in rural area. Private enterprises and enterprises with foreign investment have developed and found their position in the market.

3. Results and Discussions

3.1. Overviews in the Current Situation of World Agricultural Development. As shown in Figure 2, the growth rate of world agriculture was clearly displayed. The strong development of modern agriculture in the world has raised the question: Is agriculture only a faint role in development? Even at the extreme that, if food security is no longer a serious national problem, poverty is no longer a serious problem of rural areas, the industrialization strategy and priority thinking for agricultural development will need to change.

3.2. Overview of Vietnamese Agricultural Development. The reforms with market orientation have unleashed a great development potential and brought positive changes of the agricultural sector. There is a shift from a closed agriculture and a backward, self-sufficient production mode to commodity production agriculture, operating under market mechanisms and international integration. From a net food-imported country, Vietnam now exports every year about 7-8 million tons of food. The country has become among the top world exporters of many agricultural products such as rice, coffee, pepper, rubber, cashew nuts, shrimp, and fish. The prolonged system of subsistent agriculture has been shifted to a market mindset, which seeks to deeply regional and international economic integration. The reforms on the basis of ownership and motivation for producers, along with the industrialization process, have created breakthroughs in agricultural development. For example, the recognition of farmer household as an autonomous economic unit has removed the strict binding of the old mechanism and created a big push for agricultural development in the early period of Doi Moi. Rural economy, especially agricultural production, has rapidly moved from a self-sufficient nature to commodity production for the market at home and abroad.

As shown in Figure 3, GDP growth of the agricultural sectors has changed from a low and unstable growth trend, initially to recovery. In the period 2006-2013, the growth rate of the agricultural sector was not stable. Agricultural growth in 2005 reached 3.8%, then peaked in 2008 (reaching 4.69%) and dropped sharply to 0.49% in 2010, recovering in 2011 (reaching 4.23%) and fell sharply in 2012, 2013. GDP growth of the agricultural sector increased again in 2014 (3.44%) but then tended to decrease sharply, and in 2016, the growth rate of the agricultural sector industry is only 1.36%.

In addition to the thriving agricultural households, private and foreign-invested enterprises have begun to pay attention to investing in agriculture. In particular, a number of enterprises have pioneered the application of high technology, modern techniques, and advanced management models to agricultural production. The reforms have brought down the number of cooperatives while improving their quality and efficiency of operations. From focusing solely on agricultural production, the rural economic structure has been

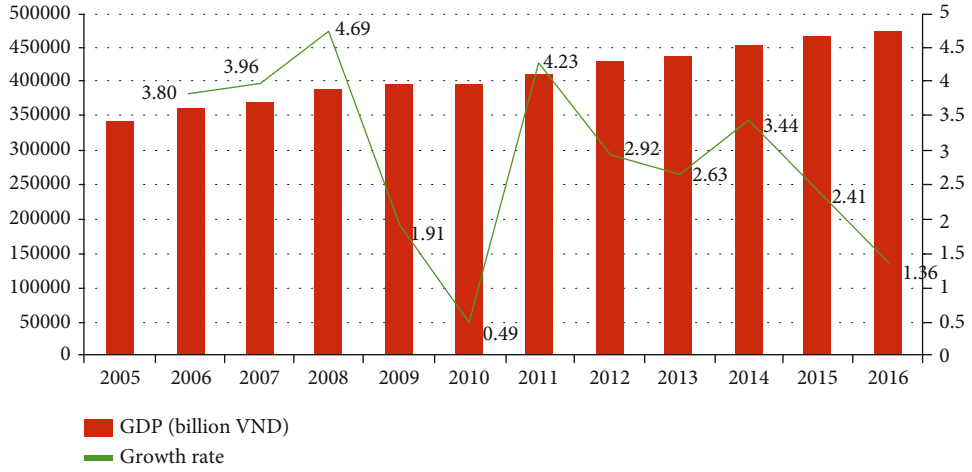

Figure 3: GDP growth of the whole agricultural sectors 2006–2016.

diversified and shifted towards increasing the proportion of service and handicraft industries. Agricultural production planning has been carried out, including the planning and construction of high-tech agricultural zones and agricultural processing industries. With the implementation of the new rural program, the face of rural infrastructure has made remarkable changes. Millions of people in the rural areas have been lifted out of chronicle poverty and hunger. The face of the rural areas has been progressively changed, especially with the recent implementation of new rural program. Vietnam's successful efforts in hunger eradication and poverty alleviation were highly appreciated by the international community, including the development organizations such as the World Bank (WB), Asian Development Bank (ADB), Food and Agriculture Organization (FAO), and the United Nations Development Program (UNDP). The material and spiritual life of farmers has been improved. The sociopolitical situation in rural areas is stable. After almost 35 years of Doi Moi, the proportion of the agricultural sector in the GDP of the economy has decreased, from about 35% in 1986 to 15% in 2018. The proportion of labor in agriculture has dropped from over 70% before the 1990s to about 38% in 2018. In fact, agricultural development proves to be a shining spot recently. In 2018, the GDP growth rate of the agricultural sector has reached 3.76%. This is the highest increase in the past 7 years, showing the great efforts in all fields and production fronts. In 2018, for the first time, the agricultural export value reached $40.02 billion. In particular, the export of key agricultural products reached $19.51 billion, of which aquatic products alone are at $9.01 billion and wooden products and forest products are at $9.34 billion (as shown in Figure 4).

Ten commodity groups had an export turnover of over $1 billion, of which 5 items had a turnover of over $3 billion (including wood and wood products, shrimp, vegetables, coffee, and cashews) [32]. Although the agriculture undoubtedly strengthens the position of Vietnamese economy in the upcoming period, it has revealed major weakness that can be aggravated by the emerging factors. In general, the process of industrialization and modernization of agriculture in Vietnam is still slow compared to the countries at the same stage of development. Vietnam's agriculture is still a latecomer with many underdeveloped characteristics: traditional production organization; small-scale production, mainly household economy; and weak link between agricultural sector with industry and services. The agricultural labor productivity of Vietnam as compared with some countries is also displayed in Table 3. The quality and added value of most agricultural products are not high. Many advantages of tropical agriculture have not been exploited, strengthened, and developed. The share of agriculture in GDP has decreased sharply but is still quite high compared to the criteria of an industrialized country. Especially, in the last 10 years, restructuring of economic sector has not positively changed the movement of population and labor between urban and rural areas or from agricultural labor to industrial and service labor. The main reason is that industry and services are not developing fast enough to attract labor from agriculture. Moreover, unemployment in rural areas is increasing rapidly due to the acquisition of agricultural land for urbanization. This is a huge challenge that hinders the improvement of labor productivity in the agricultural sector. Laborers working in agricultural sector are still overcrowded and at low quality. Most agricultural workers are still untrained. The skills of these workers are mainly formed from practical experience and low access to science and technology (S&T). Therefore, the agricultural and rural labor force faces barriers to access new occupations in urban and industrial areas, meaning that it is difficult to change agricultural jobs into nonagricultural jobs.

The gap in living standards between rural and urban areas tends to widen recently. The life of people in the mountainous and rural areas is still very difficult, often facing with natural disasters while the coverage and quality of the social security system are limited. Although the productivity and output of agricultural products have increased rapidly, the income of farmers is slowly improving; meanwhile, nonagricultural jobs provide higher incomes, causing many farmers to abandon their lands. This shows that the achievements of industrialization and modernization in

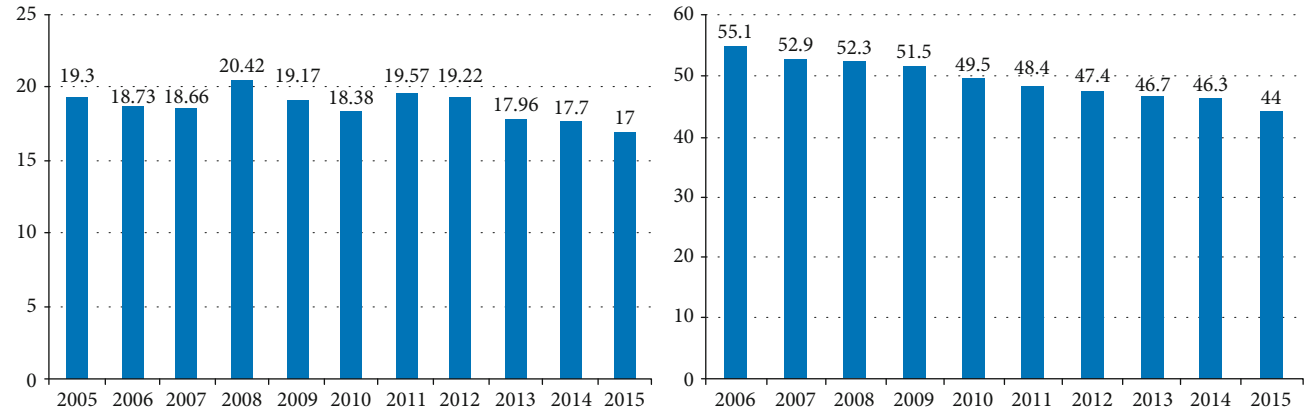

Figure 4: Vietnam's agricultural sectors *via* GDP and labor (%) (data in 2005-2015) [31].

Table 3: Agricultural labor productivity of Vietnam compared to some countries.

Unit: USD in PPP2010

Year	Cambodia	China	Indonesia	Laos	Philippines	Thailand	Vietnam
2001	568.15	793.59	1592.80	850.49	1501.87	1482.44	587.09
2005	651.60	929.84	1776.92	868.87	1713.98	1642.66	660.66
2006	677.93	975.76	1859.22	883.82	1774.47	1724.67	676.56
2010	766.92	1160.30	2124.26	937.27	1833.65	1860.01	719.06
2011	780.33	1214.09	2209.18	920.08	1871.67	1998.43	741.95
2012	804.33	1275.31	2312.70	924.07	1914.42	2089.97	756.67
2013	808.52	1332.56	2413.40	957.80	1925.30	2123.39	770.31
2014	802.99	1397.39	2520.65	1013.96	1946.35	2157.12	791.30
2015	797.71	1464.94	2628.63	1000.53	1941.33	2197.40	805.73

recent years have not been evenly distributed among groups of people, economic sectors, and regions. Farmers and rural population are the key force contributing to the socioeconomic development in rural areas but have not yet benefited adequately from such development. The socioeconomic infrastructure in rural areas is still inadequate of low quality and ineffectiveness. Rural infrastructure development is uneven, especially in mountainous provinces and the Mekong Delta. The rural economy has dealt with the issue of sustainable development. In the pursuit of immediate profits, agricultural production activities appear to damage the environment. Rural industry has grown at the expense of environmental pollution [1, 33]. The policy of agricultural industrialization and modernization has been set early but implemented very slowly. Research and development of scientific and technical progress is still limited because of insufficient coordination and synchronization. Export of agricultural products has driven the sector restructuring. However, Vietnam mainly exports raw and semiprocessed agricultural products. The added value is always low compared to other countries. The establishment and promotion of brands of agricultural, forestry, and aquatic products has not functioned effectively. Vietnam's agricultural products have not been able to participate in the value chains of large corporations, and it is difficult to gain access to the developed markets.

The speedy international integration also exposes Vietnam to various challenges in unpredictably changing world. Vietnamese agricultural products still face with fierce competition with many other countries, especially in terms of quality. Service and manufacture have not been developed to compete in terms of brand, food safety, and quality with agricultural products from Thailand, China, and other countries. Enhancing brand image and increasing added value in production are regarded a knotty issue for Vietnamese agriculturists. At present, the positive effects of many "untied" policies in agriculture and rural areas (e.g., Resolution 10 and Land Law) seem to be due, even some of them hinder the development of agriculture and rural areas and fail to solve essential problems the farmers are facing. The household economy once exerted a positive effect as a strong motivation to help farmers actively work on their assigned land, but it now no longer adapts to the requirement of applying new technology, specialization and increasing demands on greater quantity, higher quality, lower cost, and shorter time of supply. Agricultural growth is still based on the expansion of arable lands and use of resources and low level of science and technology. Vietnam's agriculture is still heavy on pure agriculture (cultivation and animal husbandry), but it has not exploited the natural advantages of forests, forest land, river, lake, and sea surfaces to strongly develop forestry specialties. The forestry sector, in particular, is currently using

the largest land bank, but its value is the lowest. Overall investment in agriculture has increased, but the ability to attract private and foreign direct investment in agricultural production is still limited. The rate of investment for an agricultural worker is too low. In addition, the efficiency of investment capital decreases, leading to the unsustainable investment situation in agriculture.

For decades, Vietnam's agricultural production has a prolonged weakness, due to scattered farming, low productivity, heavy use of fertilizers, and reliance on manual labor. The fourth industrial revolution requires fundamental changes in the farming method with the application of modern technology. It exposes a basic contradiction of Vietnam's agricultural restructure policy: the requirement of agricultural modernization and employment protection of agricultural workers. The global climate change that causes the sea level rise and extreme weather incidents to occur more frequently heavily pressurize Vietnam's agricultural production. It is exceedingly burdensome for the sustainable development of Vietnamese agriculture given that the farming methods have not been adapted to environmental problems [18, 34]. In addition, there are many major institutional bottlenecks, related to land, credit, infrastructure, and organization model such as cooperatives and food safety control, which need to be overcome. Disadvantages in agricultural production contribute to an immense gap between rural and urban areas in numerous aspects: incomes, health, education, entertainment, and quality of public services, which became dominant in the implementation of new rural program.

3.3. Agricultural Restructure Policy. To deal with the above weakness, Vietnam needs another phase (the 4th phase) of agricultural reforms—agricultural restructure which started in 2013. On June 10, 2013, the Prime Minister issued Decision No. 899/QD-TTg approving the scheme on restructuring the agricultural sector in the direction of increasing added value and sustainable development. There are 5 policy viewpoints about restructuring agriculture. Firstly, restructuring agriculture is a component of the overall restructuring of the national economy, consistent with the national socioeconomic development strategy and plan, associating with socioeconomic development and environmental protection to ensure sustainable development. Sustainable development is both a process and an objective of the agricultural development. Secondly, implementing the agricultural restructuring in line with market mechanism; ensuring the welfare of farmers and consumers; shifting from quantity-focused development to improve quality and efficiency, expressed in value and profit; and focusing on meeting social requirements are important. Thirdly, the state plays a supporting role, creating a favorable environment for activities of all economic sectors; supporting research and development, transfer of science and technology, market development, and infrastructure supply; and providing information and services. However, strengthening the participation of all economic and social sectors from the central to local levels in the process of agricultural restructuring promote the public-private partnerships (PPP), comanagement mechanisms, and the role of community organizations. Farmers and businesses directly invest in renewing production processes, technologies, and equipment to improve production and business efficiency and use resources more efficiently. Furthermore, restructuring is a complex, difficult, and long-term process that needs to be regularly evaluated, learned from experience to adjust to reality based on building a monitoring system and review and feedback from stakeholders. The agricultural restructuring scheme has three main objectives accordingly:

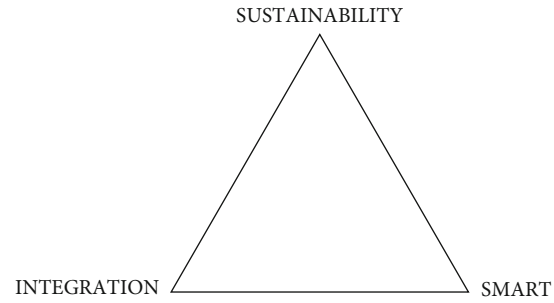

Figure 5: Three pillars of Vietnamese agricultural development.

(i) Maintain growth; improve efficiency and competitiveness through increasing productivity, quality, and added value; better meet the needs and tastes of domestic consumers; and boost exports. Strive to achieve an average GDP growth rate of 2.6% -3.0%/year in the 2011-2015 period and 3.5-4.0%/year in the 2016-2020 period

(ii) Improve income and living standards for rural residents and ensure food security (including nutritional security), contributing to poverty reduction. By 2020, rural household income will increase by 2.5 times compared to 2008; the number of communes meeting new rural criteria will be 20% by 2015 and 50% by 2020

(iii) Strengthen management of natural resources, reduce greenhouse gas emissions and other negative impacts on the environment, make good use of environmental benefits, and improve capacity of risk management and natural disaster prevention, raising the national forest coverage to 42-43% in 2015 and 45% in 2020, contributing to the implementation of the national green growth strategy [35]

In addition to the agricultural restructuring scheme, there are a number of policies and plans to accelerate the reforms of the agricultural sector such as the agricultural restructure plan for the period 2017-2020 and the restructure plans of individual subsectors as can be seen in Figure 5. Despite recently recorded achievements in agricultural development, the current agricultural restructure efforts have seemed inadequate to address the key problems of the agricultural sector. The reasons are linked to the nature of the scheme instead of the specific measures and

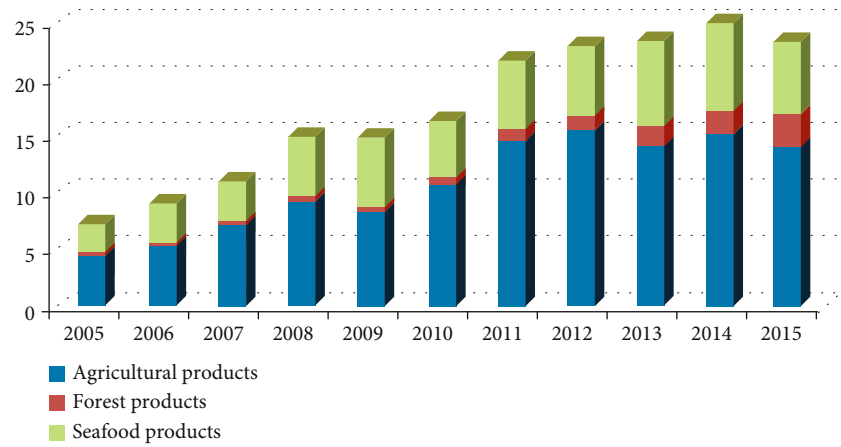

Figure 6: Export turnover of agricultural products (unit: billion USD).

guidelines. Current agricultural restructure scheme proposes the implementation timeline to 2020, despite the fact that the restructuring program for the period 2017–2020 has just been approved by the government. Because of time constraint, many objectives set in scheme may not be achieved by 2020. As a result, a number of agriculture reform measures may not be fully implemented by 2020. For example, issues of land accumulation and concentration, cooperative reforms, agricultural credits, etc. need to be experimented and gradually improved. The specific objective sets in the agricultural restructuring scheme are limited to produce major changes of Vietnam's agriculture by 2020. In fact, the restructuring program needs to be regarded in a broader sense as a comprehensive agricultural reform process that must be carried out over a longer period of time to bring significant changes. The implementation of the scheme was even delayed even when the scheme timeline was set only to 2020. Slow progress is due to various institutional barriers, limited resources, and inherent weaknesses of Vietnamese agriculture. There has not been a substantive effort to boost productivity, increase competitiveness, and restructure the agricultural workforce. Vietnam thus will need a long-term agricultural reform program to overcome the current weakness and bottleneck in agricultural development. As part of this program, we propose the model of Vietnam's agricultural development based on three key pillars: (i) sustainability, (ii) smart, and (iii) integration. On that basis, the objective of Vietnam's agricultural development to 2030 vision 2045 is to build a sustainable, smart, and integrated agriculture that firmly assures food safety, brings prosperity to rural areas, improves farmers' living standards, and accelerates Vietnamese industrialization and modernization.

As can be seen in Figure 6, in 2013, the export of agricultural, forestry, and fishery products reached 23.2 billion USD, accounting for 17.6% of the total export turnover of goods of Vietnam. In which, the export of agricultural and forestry products accounted for 71.1% and the export of aquatic products accounted for 28.9%. By the end of 2015, the total export turnover of agricultural, forestry, and fishery products reached 23,569 billion USD (agroforestry products accounted for 72.1% and fishery products accounted for 27.9%), equaling 14.5% of total export turnover country. In 2017, the export of agricultural, forestry, and fishery products reached 28.2 billion USD, accounting for 13.2% of the total export turnover of goods. In which, export turnover of agricultural and forestry products reached 19.8 billion USD, up 9% compared to 2016; seafood products reached 8.4 billion USD, up 18.5% compared to 2016.

3.4. Sustainable Agriculture. Based on the concept of sustainable development, sustainable agricultural development refers to the development of agriculture but does not harm the environment and ensures that no part of society is marginalized from agricultural development activities. For agriculture in developing countries, the requirements for sustainable development are increasingly pressing due to the intensification of production which leads to serious environmental degradation. For example, the indiscriminate use of chemical fertilizers pollutes the soil and the water. Meanwhile, the lives of farmers have not improved due to low agricultural productivity. The quality, added value, and competitiveness of products are low. The situation of "good harvest, devaluation" often takes place. To implement sustainable agricultural development, it is necessary to take measures of the government and the private sector to develop agriculture in the direction of ensuring the balance of all three objectives: agricultural growth (with the growth in production, ensuring food security), ensuring social justice (through farmers' income-ensuring mechanisms, distribution mechanisms, and reasonable price management), and protecting the environment (through solutions to develop green agriculture, smart agriculture, application of high-tech science instead of resource exploitation, protection land, water source, etc.).

3.5. Smart Agriculture. "Smart agriculture" or "climate-smart agriculture" is a new approach to agricultural development in the context of global climate change, to ensure food security, implementation of green growth, and sustainable development. According to the Food and Agriculture Organization of the United Nations (FAO), smart agriculture is "a way to achieve priorities in agricultural development both in the

short and long term along with other development priorities" [12]. Smart agriculture development is based on three pillars: (i) increasing the productivity of agricultural production in a sustainable way, thereby helping farmers increase income equitably, ensure food security, and promote development; (ii) improving the adaptive capacity and resilience to climate change of agricultural production systems at different levels; and (iii) reducing and eliminating greenhouse gas emissions from agricultural production [36]. Smart agriculture development is not only to ensure food security and increase agricultural output but also to a greater goal of improving the quality of life, ensuring social justice and human development. It also shows the multifunction and multipurpose nature of modern agricultural production, which is carried out in a synchronized and coherent manner. Therefore, smart agricultural development should be based on a combination of science with production policies and practices to identify priorities and effectively resolve conflicts between development goals, establishing appropriate institutions to help promote and nurture creativity, dissemination of good practice, and effectively use investment resources from both the private and public sectors. For backward agriculture, the application of science and technology to agricultural production is an indispensable direction to improve productivity, quality, efficiency, and the added value. In addition, developing agriculture in later economies requires changing many backward production practices and habits, lack of credit capital for farmers and high technology applications enterprises, fragmented land conditions, small-scale production that are difficult to facilitate mechanization, etc. Smart agriculture is a development approach that has a global mindset but is specifically developed to suit the specific conditions of each community, country, and region. The deployment of smart agriculture does not entirely depend on the level of development of the local economy. In fact, many smart agricultural models have been implemented simply and effectively in many developing and underdeveloped countries, from Latin America to Southeast Asia, South Asia, and Africa.

3.6. Integrated Agriculture. Liberalization is often seen as the starting point to build an integrated agriculture, opening up and participating in the world markets. Measures to liberalize the agricultural sector began in the 1980s within the framework of the structural adjustment program (SAP) of the IMF and the World Bank [37], for example, (i) taking austerity measures and reducing government spending to reduce budget deficits, including reducing subsidies for farmers and subsidizing food and foodstuffs; (ii) privatization of state-owned manufacturing to increase revenue and increase the efficiency of this sector. In many economies transitioning from central planning to a market mechanism, the consequence of this is the reform of agricultural cooperatives with the aim of increasing efficiency and profitability. But this also led to the dissolution of many cooperatives; and (iii) reducing market control to encourage competition and removal of tax barriers and protection of domestic agriculture. In fact, even in developed countries, the opening of agricultural markets is still very cautious, but this is inevitable under the pressure of joining free trade agreements. For developing economies with agricultural potential like Vietnam, participation in FTAs is expected to help promote exports, diversify markets, create job opportunities, and increase income for farmers. However, FTAs themselves are not sufficient to help Vietnam realize its agricultural development goals. Despite helping to gain access to partners' markets and increasing trade and investment volumes in the short term, FTAs do not guarantee that the Vietnamese economy can overcome the low segment of the global values chain or more productive jobs because these are largely dependent on the pace of domestic reforms. Moreover, with the application of new technologies in agricultural production activities, high-tech countries will have many advantages to develop a modern agriculture and export agricultural products back to Vietnam. If this challenge cannot be solved, new-generation FTAs become an "integration trap" for Vietnam's development process in the coming time.

4. Policy Recommendations

As part of the reform strategy, agricultural industrialization and modernization shall be a key factor in the next stage of Vietnam's agricultural development. This process can be shortened given the advantage of the follower by learning the best development practices in the world, applying modern technology and advanced management model for continuous breakthrough improvement of productivity, quality, and efficiency of agricultural production. As an essential change in the approach, Vietnam's agricultural production should give priority to quality instead of quantity development. The emphasis is on the added value of the production and market price of agricultural products. In the era of industry 4.0 and agriculture 4.0, synchronizing the application of advanced technology, including information technology, biotechnology, food processing, and preservation technology with green technology, must be considered as the core content of agricultural industrialization and modernization to improve labor efficiency as well as enhance the brand image and competitiveness of agricultural products [38]. There is a need for transformation from a fragmented agricultural production centralizing at household scale to extensive enterprise-based activities to develop a large-scale agriculture. There should be a close cooperation among government (especially the local authorities) with enterprises, scientists, and farmers to help handle the problems of output and input markets, application of modern technology, and other issues related to lands, credit, and marketing. Vietnam's agricultural structure is currently relatively simple, focusing mostly on areas with low productivity and added value. Targets should be aimed at the advancement of agricultural supporting industries and services. In particular, investment in food processing industries in rural areas plays an essential role in diversifying processed commodities. At present, the insignificant growth rate of agricultural supporting industries and services puts barrier to the increase of the added value and quality of crops, gives rise to imports of production inputs, such as agricultural

machinery, seeds, breeds, and fertilizers, and drives agricultural products with export advantage (fish sauce, cashew nuts, tea, etc.) to use foreign brand names. Priority should be given to the development of industries and services to boost both domestic consumption and export. Moreover, to maximize the aggregate value, it is suggested to combine agriculture with other services such as tourism to create new forms such as ecotourism or agriculture-based tourism. The traditional renovation model emphasizes on the development of a few prioritized competitive commodities in the international market (e.g., focus on the export of only key products such as rice, coffee, and some kinds of fruits). However, this bias gives rise to financial constraints for Vietnamese agriculture due to the precarious price of products in the world market and the emergence and fierce competition of other exporters, leaving negative impact on the environment for intensive farming of crops (for example, mass planting of rubber plantations and aquaculture). Consequently, sustainable development policies now focus on diversifying the structure of the agriculture and establishing common foundations for enhancing competitiveness and productivity, on which a basis of a few solid export-oriented agricultural sectors should be formed. The concept of local economic enhancement program in Vietnam has changed significantly. Many provinces have recognized the potential of local agricultural development as a leading industry that should be prioritized. However, the capacity of the support services in rural areas is yet limited, and for that reason, entrepreneurs face innumerable difficulties. Localities should develop a systematic agricultural growth strategy in alignment with the socioeconomic development plan and key investment programs besides promoting market expansion, tackling land, and infrastructure management bottlenecks in pursuance of achievement.

SMEs play an essential part in helping farmers deal effectively with market inputs and outputs for agricultural production. It is essential to promote agricultural and rural startup. Setting ecosystems of startup in agriculture and rural areas should concentrate on the role of community groups, associations, credit institutions, and local governments. Review and replication of the successful experiences of community cooperation models makes a huge contribution to agriculture. For example, in Dong Thap, the farmer organizations have been successfully built. This is a voluntary association supporting farmers where they "listen and talk" about production and business. It acts not only as a communication channel among farmers and between farmers and local authorities but also as a link between farmers and enterprises purchasing processed crops. Other initiatives include computerized solutions that help connect farmers with one another as well as with other enterprises and keep them up with the trends of the current market. It is also essential to build websites with the purpose of promoting agricultural brands and products. A more liberal mechanism for the accumulation of land is needed to facilitate the development of a large-scale, high-yielding agriculture. The accumulation and concentration of land should be implemented under the market mechanism. Land consolidation should be linked to the lives of farmers. This requirement is to handle the harmonious relationship between economic efficiency (accumulation and concentration of land) and social efficiency (securing employment, income for farmers, and sociopolitical environment in rural areas). The speed and scale of accumulation and concentration of land should be in line with the pace of economic and labor restructuring. It is a matter of skill training for agricultural workforce. Vietnam needs to improve land governance as the process through which decisions are made about the use of and control over land, the manner in which the decisions are implemented and enforced, and the way that competing interests in land are managed [38]. The governance approach not only focuses on the act of land reforms but also on the reforming process; as in reality, a number of sound policies and technical measures have been implemented, yet not fully or effectively. Governance is not just proposing "sound" policies on paper, but more importantly how to implement them.

5. Conclusion

To overcome the credit barriers, besides amending and supplementing existing regulations (for example, allowing agricultural land to be used as collateral), the state, especially local authorities, associations, and community organizations, needs to make a more active intervention to assist farmers in obtaining loans on a case-by-case basis, even issuing guarantee if necessary and requiring credit institutions to increase the loan limits as well as the value of the loan compared to the value of the collateral. Besides continuously making efforts to develop infrastructure, especially transport infrastructure in agricultural areas, it is also necessary to learn and apply some localities' innovative ways of implementing public-private partnerships in this field. To attract private investment, it is necessary to have appropriate incentive policies (on tax, land, financing, or credit) that at the same time can both build capacity and raise awareness of PPP for different stakeholders. It is necessary to develop a set of standardized and reasonable contracts that guarantee benefit for all stakeholders, as well as build capacity and raise awareness of PPP so that each enterprise has the ability to self-assess their pros and cons before making decisions. Moreover, in case the government fails to arrange the budget to pay for investors, favorable incentive-based policies (such as exchanging land for infrastructure or projects for infrastructure) will be a critical solution to magnetize private investors.

Data Availability

All the data and supporting materials are included within the article.

Conflicts of Interest

The authors declare that they have no conflicts of interest.

References

[1] H. T. Ha, N. T. Huong, B.-K. Lee et al., "Ternary magnetic polymer cross-coupled in [γ-APTES]-dispersion to remove azole compound: economic research and educational policy management," *Res. Chem. Intermed.*, pp. 1–26, 2020.

[2] T. D. Minh and B.-K. Lee, "Ternary cross-coupled nanohybrid for high-efficiency 1H-benzo [d] imidazole chemisorption," *Environmental Science and Pollution Research*, vol. 25, no. 22, pp. 21901–21914, 2018.

[3] T. D. Minh, B.-K. Lee, and M.-T. Nguyen-Le, "Methanol-dispersed of ternary Fe_3O_4@γ-APS/graphene oxide-based nanohybrid for novel removal of benzotriazole from aqueous solution," *Journal of Environmental Management*, vol. 209, pp. 452–461, 2018.

[4] A. Athawale, A. Bokare, H. Singh et al., "Synthesis of Ag_2O coated TiO_2 nanoparticles by sonochemically activated methods for enhanced photocatalytic activities," *Topics in Catalysis*, vol. 63, no. 11, pp. 1056–1065, 2020.

[5] K. S. Maan, A. Sharma, P. Nath, D.-V. N. Vo, H. T. Ha, and T. D. Minh, *Application of carbon-based smart nanocomposites for hydrogen production: current progress, challenges, and prospects*, New Dimensions in Production and Utilization of Hydrogen, 2020.

[6] H. Singh, A. Kumar, A. Thakur et al., "One-pot synthesis of magnetite-ZnO nanocomposite and its photocatalytic activity," *Topics in Catalysis*, vol. 63, no. 11, pp. 1097–1108, 2020.

[7] H. T. Ha, P. T. Phong, and T. D. Minh, "Synthesis of iron oxide nanoparticle functionalized activated carbon and its applications in arsenic adsorption," *Journal of Analytical Methods in Chemistry*, vol. 2021, Article ID 6668490, 9 pages, 2021.

[8] H. Thu Ha, T. Dinh Minh, and H. Minh Nguyet, "Application of green nanocomposite to adsorb cadmium ion in wastewater," *VNU Journal of Science: Earth and Environmental Sciences*, vol. 37, no. 1, 2021.

[9] H. Kaur, C. A. Huerta-Aguilar, and J. Singh, "Eclectic and economical synthesis, characterization of Li-Ba-Zn magnetic nanostructured mixed ferrites," *Journal of Sol-Gel Science and Technology*, vol. 94, no. 2, pp. 448–460, 2020.

[10] H. Kaur, J. Singh, and B. Randhawa, "Essence of superparamagnetism in cadmium ferrite induced by various organic fuels via novel solution combustion method," *Ceramics International*, vol. 40, no. 8, pp. 12235–12243, 2014.

[11] A. Thakur, A. Kumar, P. Kumar et al., "Novel synthesis of advanced Cu capped Cu_2O nanoparticles and their photocatalytic activity for mineralization of aqueous dye molecules," *Materials Letters*, vol. 276, p. 128294, 2020.

[12] L. Lipper, P. Thornton, B. M. Campbell et al., "Climate-smart agriculture for food security," *Nature Climate Change*, vol. 4, no. 12, pp. 1068–1072, 2014.

[13] T. Yagi, *A theory for measuring productivity change in the system with fixed capital*, 2010.

[14] T. Yagi, *The Sraffian price system and the classical theory of value and distribution*, 2010.

[15] T. Yagi, *Rent and profit*, 2011.

[16] K. Saito, "International trading rules and the market mechanisms: changes in the international market of agricultural commodities," *Journal of Rural Economics*, vol. 85, no. 359-2016-18460, pp. 89–101, 2013.

[17] D. B. Paudel and K. Saito, "Impact of implementation of current land reform policy in Nepal," *The Japanese Journal of Rural Economics*, vol. 17, pp. 35–39, 2015.

[18] T. D. Minh and B.-K. Lee, "Effects of functionality and textural characteristics on the removal of Cd (II) by ammoniated and chlorinated nanoporous activated carbon," *J. Mater. Cycles Waste Manag.*, vol. 19, no. 3, pp. 1022–1035, 2017.

[19] M.-T. Nguyen-Le, B.-K. Lee, and D.-M. Tran, "EDTA-Na_2-assisted synthesis of rod-like titanate-TiO_2 composite architectures with enhanced visible-light-driven properties," *Journal of Industrial and Engineering Chemistry*, vol. 56, pp. 225–233, 2017.

[20] N. T. Hanh, N. L. M. Tri, D. Van Thuan et al., "Monocrotophos pesticide effectively removed by novel visible light driven Cu doped ZnO photocatalyst," *J. Photochem. Photobiol. A: Chem.*, vol. 382, p. 111923, 2019.

[21] M.-V. Nguyen, B.-K. Lee, and T. D. Minh, *Development of highly porous amine-modified biochar bead with high CO_2 capturing capacity*, 한국대기환경학회 학술대회논문집, 2015.

[22] M.-T. Nguyen-Le, D.-M. Tran, and B.-K. Lee, "Comparison of characteristics of 16 pahs in road dust from two largest cities of Vietnam," 한국대기환경학회 학술대회논문집, 2015.

[23] N. N. Que and N. T. Que, "Effects of trade liberalization on agriculture in Vietnam: commodity aspects," 2000.

[24] V. T. Thanh, "Vietnam's trade liberalization and international economic integration: evolution, problems, and challenges," *ASEAN Economic Bulletin*, pp. 75–91, 2005.

[25] N. Minot and F. Goletti, *Rice Market Liberalization and Poverty in Viet Nam*, Intl Food Policy Res Inst, 2000.

[26] T. H. Nguyen, *An Overview of Agricultural Pollution in Vietnam: the Crops Sector*, World Bank, 2017.

[27] L. Brandt, J. Gibson, J. Giles et al., "Well begun, not yet done-Vietnam's remarkable progress on poverty reduction and the emerging challenges," *World Bank Poverty Assessment*, vol. 74910, 2013.

[28] F. Chigavazira, *The Regulation of Agricultural Subsidies in the World Trade Organization Framework. A Developing Country Perspective*, diplom. de, 2016.

[29] H. Ha, T. D. Minh, H. M. Nguyet, and A. K. Sharma, "Ampicillin adsorption onto amine-functionalized magnetic graphene oxide: synthesis, characterization and removal mechanism," *Korean Journal of Chemical Engineering*, vol. 38, no. 1, pp. 22–31, 2021.

[30] D. K. Son, "Agricultural Policy and Renovation in Vietnamese Agricultural Sector," Vietnamese Agriculture under Market Oriented Economy, The Agricultural Publishing House, Hanoi, 2001.

[31] H. S. Lee, V. D. Thiem, D. D. Anh et al., "Geographical and temporal patterns of rabies post exposure prophylaxis (PEP) incidence in humans in the Mekong River Delta and Southeast Central Coast regions in Vietnam from 2005 to 2015," *PLoS One*, vol. 13, no. 4, article e0194943, 2018.

[32] T. M. Nguyen, T. H. Lin, and H. P. Chan, "The environmental effects of urban development in Hanoi, Vietnam from satellite and meteorological observations from 1999–2016," *Sustainability*, vol. 11, no. 6, p. 1768, 2019.

[33] H. T. Ha, N. T. Huong, T. D. Minh et al., "Feasibility study of Cd (II) adsorption by a novel magnetic-graphene oxide assisted with polymer from solution," *J. Environ. Chem. Eng.*, vol. 146, no. 7, p. 04020060, 2020.

[34] H. T. Ha, N. T. Huong, L. L. Dan, N. D. Tung, V. B. Trung, and T. D. Minh, "Removal of heavy metal ion using polymer-functionalized activated carbon: aspects of environmental economic and chemistry education," *Journal of Analytical Methods in Chemistry*, vol. 2020, Article ID 8887488, 13 pages, 2020.

[35] T. B. N. Nguyen, L. T. H. Thu, and P. Q. Nguyen, "The impact of new generation FTAs on the sustainable agriculture businesses in Vietnam: case of EVFTA," *International Journal of Conservation Science*, vol. 11, no. 3, 2020.

[36] J. Verhagen, T. Vellinga, F. Neijenhuis et al., *Climate-Smart Agriculture: Scientists' Perspectives*, 2014.

[37] K. G. Kingston, "The impacts of the World Bank and IMF structural adjustment programmes on Africa: the case study of Cote D'Ivoire, Senegal, Uganda, and Zimbabwe," *Sacha Journal of Policy and Strategic Studies*, vol. 1, no. 2, pp. 110–130, 2011.

[38] N. Xuan Thang, "Promoting the role of farmers as subject and settling the relations between law and self-governed mechanisms for development of new rural society," *Vietnam Social Sciences*, no. 5, p. 1, 2016.

Hindawi
Journal of Nanomaterials
Volume 2021, Article ID 8053120, 8 pages
https://doi.org/10.1155/2021/8053120

Research Article

Feasibility of Using Sequential Sulfurized Nanoscale Zerovalent Iron-Persulfate Process to Degrade Tetrabromobisphenol A

Tuan Nguyen Quoc,[1] Khanh Hoang Nguyen,[2] Huong Ngo Thi Thuy,[3] Nguyen Thi Hanh Tien,[3] Chau Tran Thi Minh,[4] Van-Duong Dao,[3] and Thao Thanh Le[3,5]

[1]*Dept. Energy Resources & Geosystem Engineering, Sejong University, 209 Neungdong-ro, Gwangjin-gu, Seoul, Republic of Korea*
[2]*National Food Institute, Technical University of Denmark, Kgs. Lyngby 2800, Denmark*
[3]*Faculty of Biotechnology, Chemistry and Environmental Engineering, Phenikaa University, Hanoi 12116, Vietnam*
[4]*Faculty of Chemistry, VNU University of Science, Hanoi, Vietnam*
[5]*Bioresource Research Center, Phenikaa University, Hanoi 12116, Vietnam*

Correspondence should be addressed to Van-Duong Dao; duong.daovan@phenikaa-uni.edu.vn
and Thao Thanh Le; thao.lethanh@phenikaa-uni.edu.vn

Received 29 June 2021; Revised 27 July 2021; Accepted 29 August 2021; Published 13 September 2021

Academic Editor: P. Davide Cozzoli

This study proposed a sequential redox process to partially degrade tetrabromobisphenol A (TBBPA) within a reactor to a great extent. After 72 hours in an anoxic environment, 20 ppm of TBBPA could be effectively degraded by sulfurized zerovalent iron nanoparticles (S-nZVI) at concentrations of $2\,g\,L^{-1}$ and $4\,g\,L^{-1}$. Biphenol A (BPA) together with tri-, di-, and monobromobisphenol A was detected by high-performance liquid chromatography (HPLC) suggesting that TBBPA was debrominated by S-nZVI in a stepwise manner. Following the S-nZVI treatment, a persulfate-advanced oxidation process (PS-AOP) system with persulfate concentrations varied from 5 to 20 mM was incorporated to degrade the final debrominated byproduct, BPA, for 2 hours. The two-stage anoxic/oxic reactions at the same reactor with initial conditions (0.037 mM TBBPA, $4\,g\,L^{-1}$ of S-nZVI, pH 6 in anoxic stage, 20 mM of PS in the latter oxic stage) were investigated. The sulfurized layer played an important role in such a system and hypothetically contributes to increasing electron transfer from Fe^0 core as well as hydrophobicity of the NP surface. It was demonstrated that the S-nZVI/PS-AOP system could effectively remediate TBBPA and BPA and consequently provide a promising strategy to remedy brominated organic pollutants in the environment.

1. Introduction

Tetrabromobisphenol A (TBBPA) is one of the most widely used brominated flame retardants which is designed to improve the fire safety of plastic paints, synthetic textiles, electrical devices, or other materials [1–3]. TBBPA is ubiquitous and can be found in many environmental compartments such as the hydrosphere, soil, sewage sludge, sediments, and house dust [3, 4]. It could also occur in the biosolids or discharge of wastewater treatment plans if such plans could not treat TBBPA efficiently [5, 6]. Consequently, TBBPA might potentially occur in agricultural farming if contaminated biosolids or discharge was used [6]. This could be one of the entry points for TBBPA to enter the food chain and ultimately reach consumers due to its bioaccumulative property. Indeed, TBBPA has been found in food items or human biological samples [3, 4, 7, 8]. Many studies have reported negative effects of TBBPA on the health of aquatic organisms, mammals, and human beings, such as affecting cellular signalling pathways and levels of thyroid hormones and causing immunotoxicity or neurotoxicity [1, 7]. TBBPA is known as a potential endocrine disruptor and a source of oxidative stress in a wide variety of organisms [9] due to its weak estrogen-like properties and being a precursor to bisphenol A (BPA) [3, 10].

Because of TBBPA's ubiquity and health concerns, various methods have been developed to remove TBBPA from water including adsorption [11], photocatalytic degradation [12], microbial degradation [9, 13], or chemical oxidation [14, 15]. In addition to TBBPA, remediation measures also need to pay special attention to its debromination products since they could be of the same level of toxicity or even higher than that of TBBPA. For instance, BPA is a reported debrominated product of TBPPA and also a well-known endocrine disruptor [2, 16]. Therefore, complete degradation of those harmful intermediates is needed to minimize their potential risks towards the environment [9, 13, 17, 18]. For that purpose, a sequential anoxic reduction-oxic oxidation process could potentially be applied.

Recently, there have been evidences that iron-based nanoparticles such as nanoscale zerovalent iron (nZVI) [19], palladium/iron nanoparticles (Pd/Fe NPs) [2], bismuth-modified zerovalent iron nanoparticles (Bi/Fe^0 NPs) [17], or sulfurized zerovalent iron nanoparticles (S-nZVI) [18] could be employed to directly remediate or enhance the degradation of TBBPA in anoxic/oxic conditions. ZVI-based nanoparticles could also be used to activate advanced oxidation processes (AOPs) by gradually releasing Fe^{2+} to induce scavenging reactive oxygen species (ROS) in excessive medium [20, 21]. They are also affordable and environmentally friendly. In comparison to nZVI, S-nZVI showed more advantages in reductive degradation of organic pollutants due to several reasons: (i) higher hydrophobicity resulting in greater interaction with hydrophobic contaminants, (ii) lower electron transfer resistance from Fe^0 to the contaminant, and (iii) inhibition of the water reduction reaction and H_2 evolution [22, 23]. Therefore, S-nZVI was chosen as the reagent for the anoxic reduction process of TBBPA.

One of the candidates for the oxidation process is AOPs using reactive oxidants. Among them, peroxydisulfate (PS) has gradually become more conspicuous than traditional oxidants including H_2O_2 and permanganate [16]. Several technical advantages of PS-AOPs over H_2O_2-AOPs are (i) the higher achievable radical formation yield, (ii) less dependence on the operational parameters (e.g., pH, initial peroxide loading, and background constituents), and (iii) lower costs of storage and transportation due to the availability of persulfate salts [24]. Recent studies also observed that S-nZVI exhibited higher activation efficiencies for PS than nZVI due to the semiconductor material, FeS, generated on the surface of S-nZVI and better adaptability in pH variation [25, 26]. This reinforced the decision to choose S-nZVI for the anoxic reduction process.

In this work, S-nZVI was prepared then used to activate sodium persulfate ($Na_2S_2O_8$) for TBPPA degradation. The degradation of TBBPA by S-nZVI-$Na_2S_2O_8$ involved two-stage processes: reduction and persulfate oxidation. The objectives of this study were to investigate (i) various treatment parameters for optimizing the TBBPA debromination, (ii) BPA degradation efficiency, and (iii) the performance of the sequential redox treatment to achieve complete degradation of TBBPA. The outcomes from this study could offer a promising method for the complete degradation of many recalcitrant pollutants in contaminated water.

2. Materials and Methods

2.1. Chemicals and Materials. Iron (III) chloride hexahydrate, $Na_2S_2O_8$, sodium borohydride ($NaBH_4$), sodium dithionite, TBBPA, and BPA were obtained from Sigma Aldrich (Missouri, U.S.A.). HPLC-grade methanol (MeOH), ethanol (EtOH), and acetone nitrile (ACN) were obtained from Merck (Darmstadt, Germany). All chemicals were used as received without further purification. Ultrapure (18 MΩ·cm) deionized (DI) water from a Millipore Milli-Q system was used in all batch experiments.

2.2. S-nZVI Synthesis. S-nZVI nanoparticles were synthesized following Kim et al.'s method [27] with a small modification. The setup is schematically shown in Figure 1. Briefly, 30 mL solution of 0.8 M $NaBH_4$ and 0.025 M sodium dithionite was titrated to 10 mL of 0.5 M $FeCl_3$ solution with nitrogen gas purging condition. The precipitated particles were collected by magnet then rinsed with degassed water three times to remove residual $NaBH_4$. Afterwards, the particles were rinsed with EtOH, dried in a vacuum oven for 1 day at 60°C, and then stored in an anaerobic chamber prior to use for further experiments. The scanning electron microscope (SEM) images of S-nZVI are shown in Figure 1.

2.3. Sequential Redox Process

2.3.1. Reductive Debromination of TBBPA by S-nZVI NPs. Batch experiments were performed in 100 mL serum bottles capped with Teflon septa and aluminum crimps. TBBPA solutions were prepared in N_2-degassed water, and the initial TBBPA concentration was fixed at 0.037 mM (20 mg L^{-1}). The reduction process (anoxic treatment) was initiated by adding S-nZVI NPs into the prepared TBBPA solution; then, the mixture was stirred at 150 rpm under anoxic conditions. Samples were withdrawn at specific time intervals during the reaction and filtered through a 0.22 μm PTFE syringe filter for TBBPA analysis. The experimental period was 72 hours in total. The effects of NP concentrations and pH on removal efficiencies were also investigated. The concentrations of NPs were evaluated at three different levels: 1 g L^{-1}, 2 g L^{-1}, and 4 g L^{-1}. The pH of the medium adjusted by NaOH 1 M and HCl 1 M was also changed from 3 to 10. The reaction was maintained at room temperature.

2.3.2. Oxidative Degradation of BPA with S-nZVI-PS. The oxidation process was conducted by adding an appropriate amount of S-nZVI NPs and PS in serum bottles with an opened cap, exposed to the air, and stirred at 150 rpm. The BPA concentration used in this experiment was fixed at 0.037 mM, estimated by the hypothesis that TBBPA totally transformed to BPA in the prior reduction process. After 2 hours of experiment, the sample was collected and quenched with methanol for BPA analysis. The effects of PS concentrations were evaluated in the ranges of 0 mM, 5 mM, 10 mM, and 20 mM.

2.3.3. Sequential Redox Process. For the sequential redox process (anoxic followed by oxic treatment), the reduction process was initiated by adding a predetermined amount of

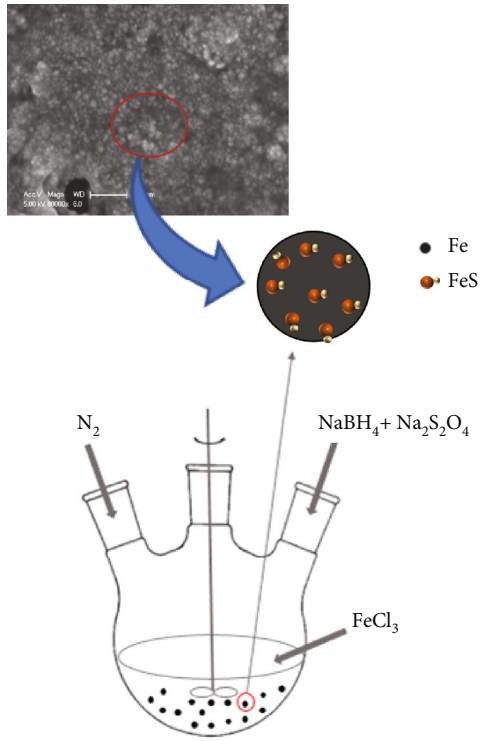

Figure 1: Scheme for one-pot synthesis of S-nZVI.

S-nZVI NPs into the reaction solution, which was continuously stirred during the reaction. After the reductive debromination process, PS was added to the solution to initiate the oxidation process. The bottle was opened and stirred at 150 rpm so that molecular oxygen could enter the test environment. The reduction and oxidation process proceeded for 72 hours and 2 hours, respectively, and samples were withdrawn for TBBPA and BPA analysis at specific time intervals during the reaction. A control test using only TBBPA without NPs was also conducted to evaluate the loss of TBBPA due to volatilization and sorption. All experiments were carried out in duplicate.

2.4. Analytical Methods. The concentrations of TBBPA and its brominated products were analyzed using a high-performance liquid chromatography (HPLC, Agilent 1100, USA) with a C_{18} reversed phase column and diode-array detector. The mobile phase was an ACN/water (70 : 30, *v*/*v*) mixture at a flow rate of 1.0 mL min^{-1}.

Removal efficiency was calculated as the below equation:

$$\text{Removal efficiency}\,(\%) = \frac{C_0 - C_t}{C_0} \times 100\%, \qquad (1)$$

where C_0 is the initial concentration of compound and C_t is the concentration of compound at t time.

3. Results and Discussion

3.1. Reductive Debromination of TBBPA by S-nZVI. The reductive debromination of TBBPA by S-nZVI was investigated with various NP concentrations (Figure 2(a)). Figure 2(a) indicates that the TBBPA removal efficiencies increased with the increase of S-nZVI NP concentration. Specifically, after 72 hours, only 50% of TBBPA was removed in the treatment with 1 g L^{-1} of NPs whereas TBBPA was almost completely removed when either 2 g L^{-1} or 4 g L^{-1} NPs were added. Additionally, the debromination rate of TBBPA was faster with 4 g L^{-1} of NPs or 2 g L^{-1} of NPs. Thus, 4.0 g L^{-1} was selected as the starting NP concentration for further experiments.

After the selection of an appropriate NP concentration, the effects of pH on TBBPA removal efficiencies were also evaluated (Figure 2(b)). It was clear that the anoxic debromination favors a low pH condition. In detail, only 50% of TBBPA was removed at pH 3 medium while the TBBPA removal efficiencies were nearly 100% at pH 6 and 10 after 72 hours. Therefore, pH 6 was selected to conduct the next experiments as it might be closer to real environmental conditions. The TBBPA removal in this study could result from both degradation and adsorption, which might give rise to the differences in pH-dependent trends from other studies that only take degradation into account. Butler and Hayes [28] reported that the rate of reductive dehalogenation by FeS increased with the increase of pH from 7.3 to 9.3, which was possibly due to a decrease in the reduction potential of reactive surface species with increasing pH. It was also reported that the deprotonated ligands (i.e., ≡FeO- and ≡S-) are more favorable for electron donation [27], which results in the increased rates of TBBPA reduction at higher pH levels.

During the course of the anoxic treatment, the debrominated metabolites of TBPPA, including tribrominated- (tri-BBPA), dibrominated- (di-BBPA), and monodibrominated bisphenol A (mono-BBPA), and BPA were observed by HPLC analysis (Figure 3). It is worthy to note that the debrominated metabolite patterns were considerably different between 2 g L^{-1} and 4 g L^{-1} of NP treatments (Figure 4). For instance, the production of tri-BBPA was steeply increased during the first 12 hours of 2 g L^{-1} NP treatment, whereas the tri-BBPA production in 4 g L^{-1} NP treatment peaked after 6 hours then declined afterwards. The slowly decreasing peaks of further debrominated byproducts, such as di- and mono-BBPA, in 2 g L^{-1} or 4 g L^{-1} of NPs indicated the uncompleted debromination of TBBPA after a 72-hour reaction. The occurrence of BPA was detected after 24 hours and 12 hours of adding 2 g L^{-1} and 4 g L^{-1} of NPs, respectively. After 72 hours, the concentration of BPA with 4 g L^{-1} NP treatment was measured at 0.03 mM. According to the stoichiometric ratio and mass balance, 83.3% of TBBPA was transformed to BPA while 17.7% of TTBPA remained in di- and mono-BBPA byproducts.

To explore the role of the sulfurized layer, Wu et al. [18] calculated the electron efficiency (EE) of S-nZVI for TBBPA reduction. It was suggested that sulfidation could improve the electron transfer of the core Fe^0 NPs. Many studies also agreed that the FeS layer could facilitate electron conduction from the Fe^0 core to the S-nZVI surface since FeS is a well-known metallic conductor [18, 27]. Besides, the impact of sulfur amount and speciation on the reactivity and

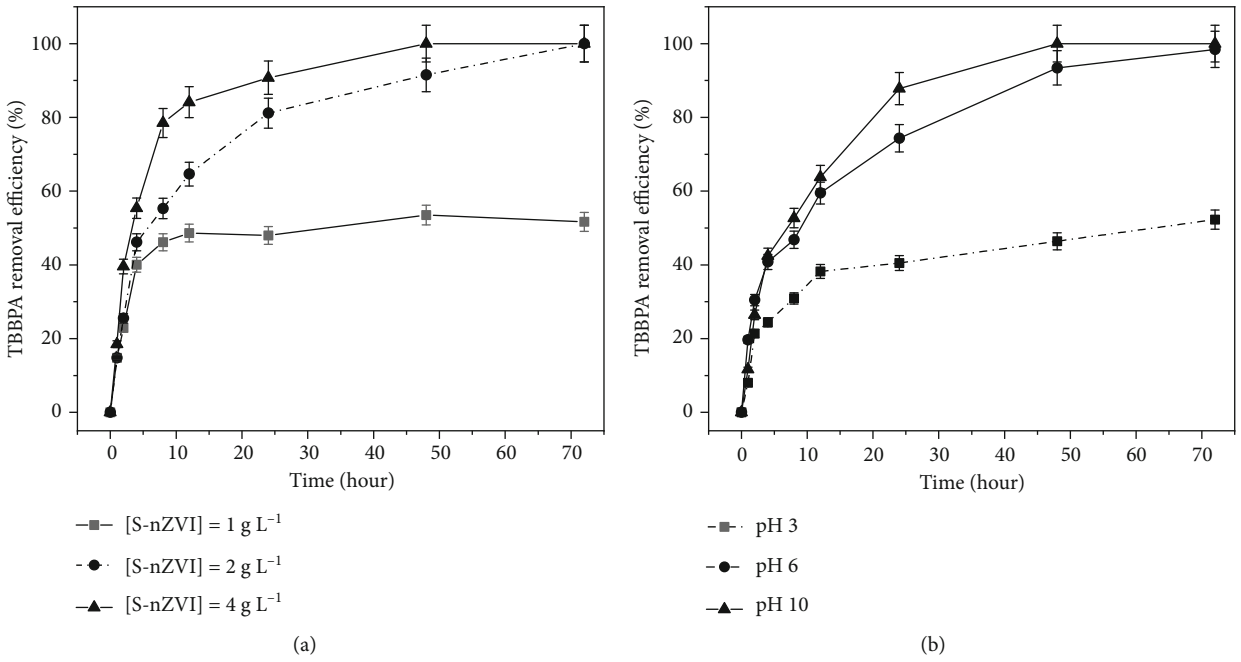

Figure 2: TBBPA degradation by S-nZVI under anoxic conditions: (a) the effect of S-nZVI concentration at 1 g L^{-1}, 2 g L^{-1}, and 4 g L^{-1} and (b) the effect of pH at 3, 6, and 10.

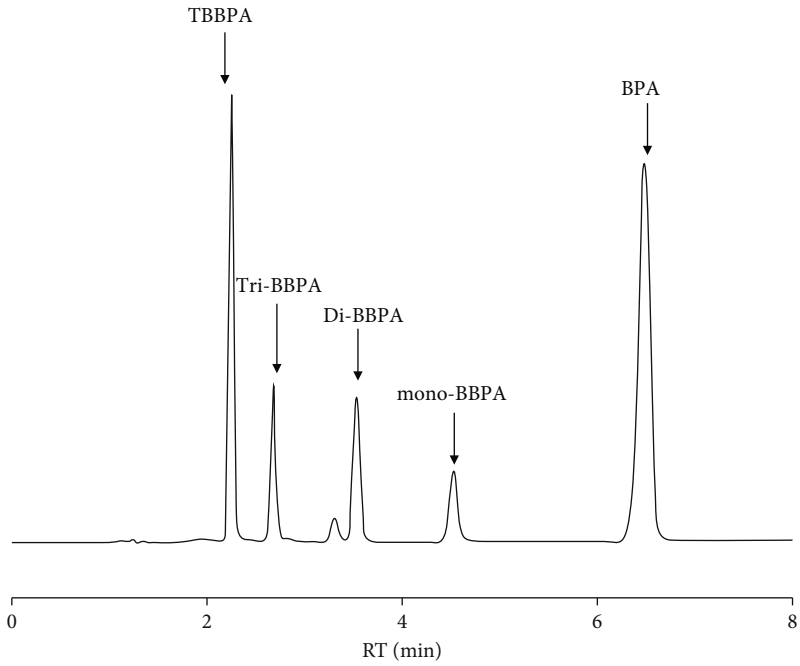

Figure 3: HPLC chromatogram for the TBBPA and its debrominated products after 24-hour anoxic treatment by the S-nZVI system.

selectivity of S-nZVI has been reported previously [22]. It was observed that hydrophobicity appears to be an important factor for electron selectivity, but the S/Fe ratio also plays a role in the overall electron efficiency. Xu et al. [22, 29, 30] also reported that the high selectivity and low reactivity with water indicate that S-nZVI could express better reactivity with hydrophobic pollutants, especially halogenated compounds. The sulfidation induced hydrophobicity, improved electron transfer, blocked hydrogen adsorption, and charge density redistribution which promote degradation of organic contaminants via electron-mediated reductions instead of hydrogenolysis in the case of nZVI [22, 29].

3.2. Oxidative Degradation of BPA with S-nZVI/Persulfate System. Many studies clearly identified that dissolved O_2 was essential for BPA degradation [17, 18] due to $OH^{\cdot}$

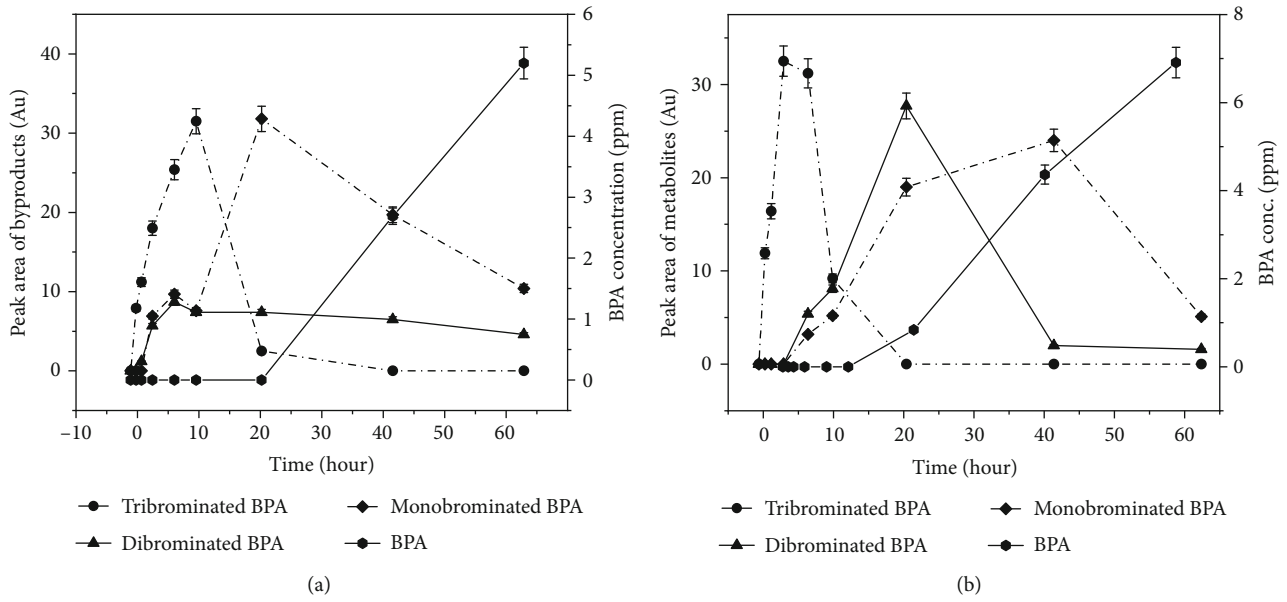

Figure 4: TBBPA, tri-BBPA, di-BBPA, mono-BBPA, and BPA composition during anoxic treatment with various concentrations of S-nZVI. [TBBPA] = 0.037 mM, $[\text{S-nZVI}]_0$ = 2 and 4 g L^{-1}, initial pH = 6.

production under oxic conditions induced by FeS [20, 26, 31]. However, compared with the hydroxyl radical reaction, sulfate radicals demonstrated higher reduction potential at a wider pH range and are more selective for oxidation of phenolic compounds [32, 33]. To evaluate the TBBPA removal efficiency in the sequential redox reaction, the BPA oxidation was set up at slightly acidic pH ~6 and PS oxidant with $SO_4^{\cdot-}$ production was selected. In this study, the BPA degradation was performed by a S-nZVI and persulfate system. As shown in Figure 5, the decrease of BPA was well correlated with the concentrations of persulfate. No degradation of BPA was observed in the presence of S-nZVI without the addition of PS. However, after 2 hours, 50%, 60%, and 98% of BPA were removed in the treatments with PS concentrations at 5 mM, 10 mM, and 20 mM, respectively. This enhancement could be ascribed to the greater decomposition of PS to produce more $SO_4^{\cdot-}$ in the S-nZVI/PS system while the radical scavenging effect was not observed at higher PS concentration.

Earlier studies suggested $SO_4^{\cdot-}$ radical as the only predominant radical for degrading target contaminants. However, recent evidences have emerged that $OH^{\cdot}$ radical could be another reactive oxidizing species besides $SO_4^{\cdot-}$ radical [26] in a PS system. When the pH was less than 7, $OH^{\cdot}$ and $SO_4^{\cdot-}$ could be obtained, whereas at pH > 9 conditions, $OH^{\cdot}$ would be the main radical [34]. In this study, the experiments were set up at pH 6; therefore, the oxidation of BPA could be driven by both $SO_4^{\cdot-}$ and $OH^{\cdot-}$ species. The possible mechanism for BPA degradation by the S-nZVI/PS system was proposed as follows. At first, Fe^{2+} was formed on the surface of NPs via the corrosion of the core Fe^0. Afterwards, PS was activated by Fe^{2+}, and the highly reactive radicals $SO_4^{\cdot-}/OH^{\cdot}$ were generated continuously via Fenton reaction in the presence of O_2. Finally, BPA was attacked by

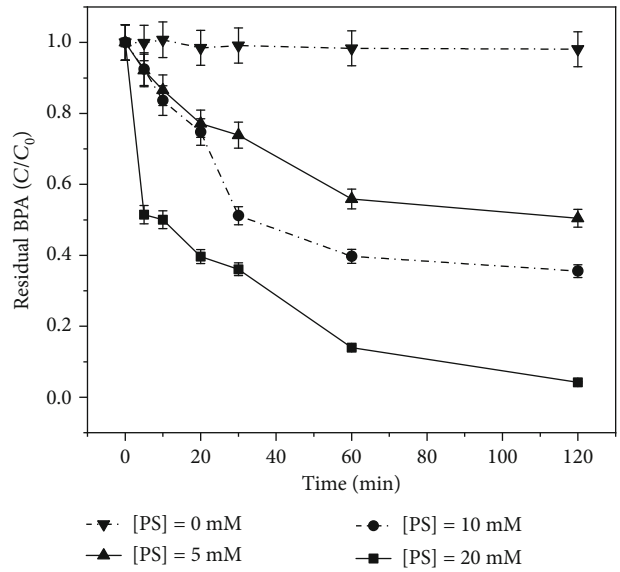

Figure 5: The effect of [PS] on BPA degradation by S-nZVI/PS-AOP system under oxic condition. [BPA] = 0.037 mM, $[\text{S-nZVI}]_0$ = 4 g L^{-1}, [PS] = 0-20 mM, initial pH = 6.

$SO_4^{\cdot-}/OH^{\cdot}$ and transformed into its intermediates via a series of oxidation reactions.

Guo et al. [25] reported that the sulfide layer can significantly promote the release of iron ions in a nonstrong acid environment. Previous studies have proved that iron sulfide is a well-known metallic conductor because of the presence of delocalized electrons in its layers [35–37]. The deposition of FeS on the S-nZVI surface could also facilitate electrons from the iron core to the surface just like an electric "wire" [26, 38], which would lead to a continuous formation of surface-bound ferrous that were capable of activating

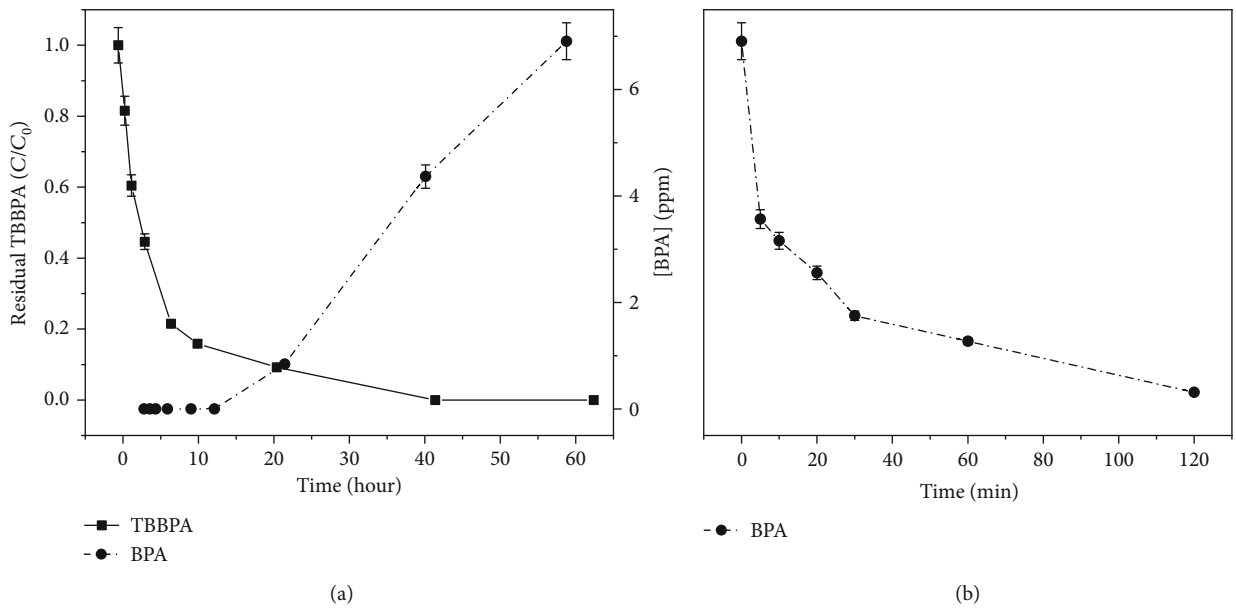

Figure 6: Two-stage anoxic-oxic degradation of TBBPA and BPA. (a) Anoxic reductive debromination of TBBPA by S-nZVI NPs with BPA production. (b) Oxidative degradation of BPA with the addition of PS and air exposure. [TBBPA] = 0.037 mM, $[\text{S-nZVI}]_0 = 4\ \text{g L}^{-1}$, [PS] = 20 mM, initial pH = 6.

persulfate. Besides, $SO_4^{\cdot-}$ radical normally undergo electron transfer reactions while $HO^{\cdot}$ may also react via hydrogen-atom abstraction along with an electron transfer process which is however less prominent in their case. Therefore, S-nZVI showed a better performance than NZVI in activating persulfate to degrade the pollutant [39].

3.3. Sequential Redox Degradation of TBBPA. Based on the abovementioned results, the sequential redox process of TBBPA was examined (Figure 6). In Figure 6, the reductive debromination of TBBPA by S-nZVI significantly increased during the first 24 hours. When the reaction time reached 24 hours, 90% of TBBPA was degraded in accordance with a slow rise of BPA. After 72 hours of treatment, BPA, a final intermediate of the reduction process, was detected as the major byproduct. It was estimated that 83.3% of TBBPA was transformed to BPA. After the 72-hour anoxic reduction process, BPA degradation continuously happened in the opened and stirred system via an oxic process. A number of studies have investigated the reduction of halogenated pollutants, such as TCE, TBBPA, or oxidative process of their metabolites using various types of NPs. Several recent publications utilized the advantages of NPs in sequential processes, consisting of both reductive and oxidative reactions, to completely remove pollutants without any toxic intermediates [17, 18]. A study by Lee et al. [17] emphasized that degradation of TBBPA was completed using Bi/Fe^0 NPs under two-step anoxic- oxic coupled with citric acid (CA) conditions. However, the limitation of that system is the requirement of air sparging and ligand CA to accelerate the generation of reactive oxygen species. Wu et al. [18] previously apply S-nZVI/H_2O_2 to remove TBBPA significantly under a similar sequential concept after a total of 88 hours. In this study, the S-nZVI treatments required less time to degrade TBBPA. In addition, the system utilized S-nZVI and PS which are more stable under nonacid conditions than other nZVI-based NPs or H_2O_2-AOP oxidants. Another advantage of this concept is the utilization of passive atmospheric O_2 dissolution instead of O_2 purging, which could increase the cost effect of the remediation system.

3.4. Implication for Performance under Environmentally Relevant Conditions. Although other nZVI-based materials (e.g., bare nZVI, Fe/Pd bimetals, and S-nZVI) have also demonstrated the ability to degrade TBBPA under anoxic conditions, those NPs require acidic conditions to accelerate degradation efficiency. In addition, the debromination intermediates such as BPA still remained. Therefore, the production of ROS, particularly $OH^{\cdot}$ or $SO_4^{\cdot-}$ radical species, is needed to degrade those intermediates further under the subsequent oxic conditions. Our study demonstrated that TBBPA and BPA were effectively degraded via the two-stage anoxic and oxic processes using S-nZVI/PS at nonacidic conditions with the enhancement of dissolved oxygen from the air. According to the proposed reaction mechanisms, the S-nZVI could be initially applied in anoxic environments such as groundwater. Afterwards, water purging via either natural or anthropogenic activities such as groundwater recharge, dredging, water table fluctuations, and bioturbation could bring anoxic aquifer and lake sediments into oxic environments to initiate the oxidation by PS-AOP. Additionally, the proposed sequential system could be employed in wastewater treatment plans where treatment conditions could be controlled. Hence, S-nZVI/PS can be used in broad areas and locations for environmental remediation of organic contaminants.

4. Conclusions

In this study, a sequential redox process using S-nZVI NPs coupled with PS has been developed and evaluated for the

degradation of TBBPA. Experimental results showed that TBBPA was degraded through the stepwise debromination into lowly brominated intermediates by the reduction process, which was then oxidized further by the oxidation process. The system was inferior to normal nZVI with enhanced electron transfer, increased depassivation of nZVI, facilitated the adsorption of organic pollutants, and effectively worked in a nonacid environment. The proposed sequential treatment system has the advantage of performing reduction and oxidation processes in the same reactor to effectively degrade TBBPA. Therefore, it is expected to be applicable in real-life conditions for remediation of TBBPA and potentially other organic contaminants which are toxic and persistent in the environment.

Data Availability

The datasets generated during and/or analyzed during the current study are available from the corresponding authors on reasonable request.

Conflicts of Interest

The authors declare that they have no competing interests.

References

[1] Y. Yu, Z. Yu, H. Chen et al., "Tetrabromobisphenol A: disposition, kinetics and toxicity in animals and humans," *Environmental Pollution*, vol. 253, pp. 909–917, 2019.

[2] X.-Q. Lin, Z.-L. Li, Y.-Y. Zhu et al., "Palladium/iron nanoparticles stimulate tetrabromobisphenol A microbial reductive debromination and further mineralization in sediment," *Environment International*, vol. 135, p. 105353, 2020.

[3] J.-F. Lu, M.-J. He, Z.-H. Yang, and S.-Q. Wei, "Occurrence of tetrabromobisphenol A (TBBPA) and hexabromocyclododecane (HBCD) in soil and road dust in Chongqing, western China, with emphasis on diastereoisomer profiles, particle size distribution, and human exposure," *Environmental Pollution*, vol. 242, pp. 219–228, 2018.

[4] S. Morris, C. R. Allchin, B. N. Zegers et al., "Distribution and fate of HBCD and TBBPA brominated flame retardants in North Sea estuaries and aquatic food webs," *Environmental Science & Technology*, vol. 38, no. 21, pp. 5497–5504, 2004.

[5] T. B. Chokwe, J. O. Okonkwo, and M. S. Nwamadi, "Occurrence and distribution of tetrabromobisphenol A and its derivative in river sediments from Vaal River Catchment, South Africa," *Emerging Contaminants*, vol. 3, no. 3, pp. 121–126, 2017.

[6] K. Liu, J. Li, S. Yan, W. Zhang, Y. Li, and D. Han, "A review of status of tetrabromobisphenol A (TBBPA) in China," *Chemosphere*, vol. 148, pp. 8–20, 2016.

[7] J.-G. Lee, Y. Jeong, D. Kim, G.-J. Kang, and Y. Kang, "Assessment of tetrabromobisphenol and hexabromocyclododecanes exposure and risk characterization using occurrence data in foods," *Food and Chemical Toxicology*, vol. 137, p. 111121, 2020.

[8] J. H. Tay, U. Sellström, E. Papadopoulou, J. A. Padilla-Sánchez, L. S. Haug, and C. A. de Wit, "Serum concentrations of legacy and emerging halogenated flame retardants in a Norwegian cohort: relationship to external exposure," *Environmental Research*, vol. 178, p. 109731, 2019.

[9] F. Sun, B. A. Kolvenbach, P. Nastold, B. Jiang, R. Ji, and P. F.-X. Corvini, "Degradation and metabolism of tetrabromobisphenol A (TBBPA) in submerged soil and soil–plant systems," *Environmental Science & Technology*, vol. 48, no. 24, pp. 14291–14299, 2014.

[10] J. Tang, J. Feng, X. Li, and G. Li, "Levels of flame retardants HBCD, TBBPA and TBC in surface soils from an industrialized region of East China," *Environmental Science: Processes & Impacts*, vol. 16, no. 5, pp. 1015–1021, 2014.

[11] I. I. Fasfous, E. S. Radwan, and J. N. Dawoud, "Kinetics, equilibrium and thermodynamics of the sorption of tetrabromobisphenol A on multiwalled carbon nanotubes," *Applied Surface Science*, vol. 256, no. 23, pp. 7246–7252, 2010.

[12] J. Xu, W. Meng, Y. Zhang, L. Li, and C. Guo, "Photocatalytic degradation of tetrabromobisphenol A by mesoporous BiOBr: efficacy, products and pathway," *Applied Catalysis B: Environmental*, vol. 107, no. 3, pp. 355–362, 2011.

[13] J. Liu, Y. Wang, B. Jiang et al., "Degradation, metabolism, and bound-residue formation and release of tetrabromobisphenol A in soil during sequential anoxic–oxic incubation," *Environmental Science & Technology*, vol. 47, no. 15, pp. 8348–8354, 2013.

[14] Y. Gao, S.-Y. Pang, J. Jiang et al., "Transformation of flame retardant tetrabromobisphenol A by aqueous chlorine and the effect of humic acid," *Environmental Science & Technology*, vol. 50, no. 17, pp. 9608–9618, 2016.

[15] Y. Wu, Y. Wang, T. Pan, and X. Yang, "Oxidation of tetrabromobisphenol A (TBBPA) by peroxymonosulfate: the role of in-situ formed HOBr," *Water Research*, vol. 169, p. 115202, 2020.

[16] R. J. Watts and A. L. Teel, "Treatment of contaminated soils and groundwater using ISCO," *Practice Periodical of Hazardous, Toxic, and Radioactive Waste Management*, vol. 10, no. 1, pp. 2–9, 2006.

[17] C.-S. Lee, D.-S. Oh, T. T. Le, J. Gong, and Y.-S. Chang, "Ligand-assisted sequential redox degradation of tetrabromobisphenol A using bimetallic zero-valent iron nanoparticles," *Industrial & Engineering Chemistry Research*, vol. 57, no. 51, pp. 17329–17337, 2018.

[18] J. Wu, J. Zhao, J. Hou, R. J. Zeng, and B. Xing, "Degradation of tetrabromobisphenol A by sulfidated nanoscale zerovalent iron in a dynamic two-step anoxic/oxic process," *Environmental Science & Technology*, vol. 53, no. 14, pp. 8105–8114, 2019.

[19] K. Lin, J. Ding, and X. Huang, "Debromination of tetrabromobisphenol A by nanoscale zerovalent iron: kinetics, influencing factors, and pathways," *Industrial & Engineering Chemistry Research*, vol. 51, no. 25, pp. 8378–8385, 2012.

[20] H. Dong, B. Wang, L. Li et al., "Activation of persulfate and hydrogen peroxide by using sulfide-modified nanoscale zerovalent iron for oxidative degradation of sulfamethazine: a comparative study," *Separation and Purification Technology*, vol. 218, pp. 113–119, 2019.

[21] H. Hou, Z. Pi, F. Yao et al., "A critical review on the mechanisms of persulfate activation by iron-based materials: clarifying some ambiguity and controversies," *Chemical Engineering Journal*, vol. 407, p. 127078, 2021.

[22] J. Xu, H. Li, and G. V. Lowry, "Sulfidized nanoscale zero-valent iron: tuning the properties of this complex material for efficient groundwater remediation," *Account of materials research*, vol. 2, pp. 420–431, 2021.

[23] J. Xu, A. Avellan, H. Li et al., "Sulfur loading and speciation control the hydrophobicity, electron transfer, reactivity, and selectivity of sulfidized nanoscale zerovalent iron," *Advance Materials*, vol. 32, no. 17, p. 1906910, 2020.

[24] J. Lee, U. von Gunten, and J.-H. Kim, "Persulfate-based advanced oxidation: critical assessment of opportunities and roadblocks," *Environmental Science & Technology*, vol. 54, no. 6, pp. 3064–3081, 2020.

[25] W. Guo, Q. Zhao, J. Du, H. Wang, X. Li, and N. Ren, "Enhanced removal of sulfadiazine by sulfidated ZVI activated persulfate process: performance, mechanisms and degradation pathways," *Chemical Engineering Journal*, vol. 388, p. 124303, 2020.

[26] H. Dong, K. Hou, W. Qiao et al., "Insights into enhanced removal of TCE utilizing sulfide-modified nanoscale zerovalent iron activated persulfate," *Chemical Engineering Journal*, vol. 359, pp. 1046–1055, 2019.

[27] E.-J. Kim, K. Murugesan, J.-H. Kim, P. G. Tratnyek, and Y.-S. Chang, "Remediation of trichloroethylene by FeS-coated iron nanoparticles in simulated and real groundwater: effects of water chemistry," *Industrial & Engineering Chemistry Research*, vol. 52, no. 27, pp. 9343–9350, 2013.

[28] E. C. Butler and K. F. Hayes, "Factors influencing rates and products in the transformation of trichloroethylene by iron sulfide and iron metal," *Environmental Science & Technology*, vol. 35, no. 19, pp. 3884–3891, 2001.

[29] J. Xu, Y. Wang, C. Weng et al., "Reactivity, selectivity, and long-term performance of sulfidized nanoscale zerovalent iron with different properties," *Environmental Science and Technology*, vol. 53, pp. 5936–5945, 2019.

[30] W. Shen, J. Xu, and L. Zhu, "Triton X-100 improves the reactivity and selectivity of sulfidized nanoscale zerovalent iron toward tetrabromobisphenol A: implications for groundwater and soil remediation," *Journal of Hazardous Materials*, vol. 416, p. 126119, 2021.

[31] Y. Sun, M. Gu, S. Lyu et al., "Efficient removal of trichloroethene in oxidative environment by anchoring nano FeS on reduced graphene oxide supported nZVI catalyst: the role of FeS on oxidant decomposition and iron leakage," *Journal of Hazardous Materials*, vol. 392, p. 122328, 2020.

[32] S. K. Ling, S. Wang, and Y. Peng, "Oxidative degradation of dyes in water using Co^{2+}/H_2O_2 and Co^{2+}/peroxymonosulfate," *Journal of Hazardous Materials*, vol. 178, no. 1, pp. 385–389, 2010.

[33] T. Olmez-Hanci and I. Arslan-Alaton, "Comparison of sulfate and hydroxyl radical based advanced oxidation of phenol," *Chemical Engineering Journal*, vol. 224, pp. 10–16, 2013.

[34] G. Zhao, J. Zou, X. Chen et al., "Iron-based catalysts for persulfate-based advanced oxidation process: microstructure, property and tailoring," *Chemical Engineering Journal*, vol. 127845, 2020.

[35] D. Fan, G. O'Brien Johnson, P. G. Tratnyek, and R. L. Johnson, "Sulfidation of nano zerovalent iron (nZVI) for improved selectivity during in-situ chemical reduction (ISCR)," *Environmental Science & Technology*, vol. 50, no. 17, pp. 9558–9565, 2016.

[36] J. Zou, J. Ma, L. Chen et al., "Rapid acceleration of ferrous iron/peroxymonosulfate oxidation of organic pollutants by promoting Fe(III)/Fe(II) cycle with hydroxylamine," *Environmental Science & Technology*, vol. 47, no. 20, pp. 11685–11691, 2013.

[37] J. Li, X. Zhang, M. Liu et al., "Enhanced reactivity and electron selectivity of sulfidated zerovalent iron toward chromate under aerobic conditions," *Environmental Science & Technology*, vol. 52, no. 5, pp. 2988–2997, 2018.

[38] S. Song, Y. Su, A. S. Adeleye, Y. Zhang, and X. Zhou, "Optimal design and characterization of sulfide-modified nanoscale zerovalent iron for diclofenac removal," *Applied Catalysis B: Environmental*, vol. 201, pp. 211–220, 2017.

[39] H. Dong, C. Zhang, J. Deng et al., "Factors influencing degradation of trichloroethylene by sulfide-modified nanoscale zero-valent iron in aqueous solution," *Water Research*, vol. 135, pp. 1–10, 2018.

Hindawi
Journal of Nanomaterials
Volume 2021, Article ID 8688238, 7 pages
https://doi.org/10.1155/2021/8688238

Research Article

Utilization of Rice Husk, an Abundant and Inexpensive Biomass in Porous Ceramic Membrane Preparation: A Crucial Role of Firing Temperature

Tran Thi Ngoc Dung,[1] **Vu Nang Nam**,[1] **Tran Thi Nhan**,[1] **Bui Nguyen Hoang**,[1] **Do Le Thanh Hung**,[1] **and Dang Viet Quang**[2]

[1]*Institute of Environmental Technology, Vietnam Academy of Science and Technology, 18 Hoang Quoc Viet, Hanoi, Vietnam*
[2]*Faculty of Biotechnology, Chemistry and Environmental Engineering, Phenikaa University, Hanoi 12116, Vietnam*

Correspondence should be addressed to Tran Thi Ngoc Dung; ttndzung@gmail.com
and Dang Viet Quang; quang.dangviet@phenikaa-uni.edu.vn

Received 11 May 2021; Revised 2 July 2021; Accepted 20 July 2021; Published 5 August 2021

Academic Editor: Thanh Dong Pham

The influence of firing temperature on characteristics and bacterial filtration of the porous ceramic membrane prepared from rice husk (20 wt%) and kaolin has been investigated. As firing temperatures increased from 900 to 1100°C, the compressive strength of membrane increased from 555.3 N/cm^2 to 2992.3 N/cm^2, whereas the porosity decreased from 49.4 to 30.2% due to structural condensation and mullite formation. The condensation caused pore contraction that finally improved bacterial removal efficiency from ~90% to 99%. The results suggested that the porous ceramic membrane prepared from rice husk and kaolin should be fired at ~1050°C to attain both strength and filtration efficiency.

1. Introduction

Lack of access to clean water has been a critical issue in many parts of the world, particularly in poor and developing countries [1], and it is the cause of water-borne diseases such as diarrhea. Paradoxically, abundant water resources including lake, river, or stream are available in those countries; however, these sources are usually unsafe and required the application of treatment measures. Various water treatment technologies including boiling, chlorination, sand filtration, reverse osmosis filtration, porous ceramic membrane filtration, coagulation, and adsorption are considerably suitable for water purification. Among those technologies, water filtration using porous ceramic membrane (PCM) has emerged as a great candidate for water treatment [2–4]. The advantages of this method are its easy operation, easy cleaning, high durability, and affordable cost. PCMs can be fabricated in desired shapes from locally available clays and biomass [5]. Biomass sources like sawdust, wood flake, and flour have been widely used as burning additives to prepare PCMs [3, 6–10]. In a research conducted by Zereffa and Bekalo, PCMs fabricated from clay with 5% grog and 15% sawdust and fired at 1000°C can remove 97.5% *E. coli* and 87.9% turbidity [11]. PCM fabricated by Bulta and Micheal using the similar method but fired at 800°C can eliminate 96.5% *E. coli* and 82.1% turbidity, respectively [8]. Obviously, PCMs have a great potential application in the field of water filtration for bacterial removal.

Rice husk is an abundant agricultural waste with an estimation of 1.5×10^8 tonnes/year [12], but only a small fraction has been practically utilized [13]. It is estimated that 90% of rice is burned in open air or discharged into river and oceans, which may cause significant environmental consequences [14, 15]. Rice husk is a high energy source with a heating value of 15 MJ/kg [15], which has high potential for thermal energy production. Traditionally, rice husk is used as thermal energy for household cooking [16, 17], but nowadays, it is slowly replaced by gas and electric energy. Novel

technologies such as direct combustion, fast pyrolysis, alcohol production, and gasification have been investigated to create the added value to rice husk [12–15]. However, the deployment of those novel technologies is still limited; therefore, more practical measures that can create the added value to rice husk are required.

Recently, the utilization of rice husk to produce PCMs has attracted significant attention [18–23]; however, only few works reported on the fabrication of membranes for water filtration. Soppe et al. demonstrated that PCMs prepared from clay and rice husk can meet the requirement for household water filtration with >2-log reduction in *E. coli* concentration [21]. Some parameters such as rice husk/clay ratio, maximum kiln temperature, and rice husk particle size that may affect the filter's performance were investigated. Porosity plays a significant role in controlling the filtration flow rate of PCMs. The porosity and pore size can be controlled by the rice husk/clay ratio and size of rice husk. Firing temperature has considerable influence on the characteristics and filtration performance of PCMs; however, this influence was investigated at firing temperatures ≤ 950°C without elucidating the reason that may cause the increment in ceramic strength and filtration efficiency [21]. Previous investigation on the phase transition of ceramics from kaolin indicated that a major phase that contributes to the strength of ceramics is mullite. The formation of mullite phase begins at ≥900°C, but more noticeable at ≥1000°C [24–26]. Therefore, it is necessary to study the phase transition of porous ceramics using rice husk as a pore-forming agent in a higher range of firing temperature. In this study, the critical effect of firing temperature on the characteristics and bacterial removal efficiency of PCMs prepared from kaolin and rice husk will be studied at a temperature from 900 to 1100°C.

2. Materials and Methods

2.1. Materials. Kaolin samples from Truc Thon (Hai Duong, Vietnam, Table 1) were provided by a local supplier. Rice husk was collected from a local source in Hai Duong, Vietnam. Kaolin samples were dried and ground to the particle size ≤ 63 μm while rice husk was crushed until the size of ≤0.5 mm. Conventional agar and the strains of *E. coli* ATTC 25922 were purchased from Merck.

2.2. Porous Ceramic Membrane Preparation. In a typical PCM preparation, a desired amount of kaolin and rice husk (20–38 wt% in dry ceramic mixture including kaolin and rice husk) was mixed with water (approximately 27 wt% of dry ceramic mixture) and incubated in 48 h. The mixture was then filled in a steel cylindrical mold (60 mm diameter and 20 mm height) and pressed by a hydraulic press machine at about 500 kg/cm^2 to form filter disk samples. The prepared samples were dried at room temperature for 5 days and at 105°C for one day followed by firing in a furnace. Firing process was programmed in 3 steps involving the increase of temperature from room temperature to 200°C, then to 550°C, and to a firing temperature in a range of 900 to 1100°C at the ramping rate of 3°C/min; at the end of each step, an isothermal period of 2 h was applied. Samples were finally cooled down to room temperature for further experiments.

Table 1: Composition of a kaolin sample.

No.	Chemical composition	Kaolin (wt%)
1	SiO_2	63.88
2	Al_2O_3	25.2
3	MgO	1.58
4	K_2O	2.47
6	CaO	2.1
7	TiO_2	0.31
8	MnO	0.02
9	Fe_2O_3	2.63
10	Others	1.78

2.3. Characterization. Porosity of porous ceramic membrane is determined by a saturated water method [27]. Dry filter sample is weighed, soaked in water for 24 hours, and taken out to check the water saturated mass.

$$P = \frac{(m_{s-}m_d)}{\rho_w V_F} \times 100\%, \quad (1)$$

$$V_m = \frac{(m_{s-}m_{iw})}{\rho_w}, \quad (2)$$

where P is porosity (%), m_s is weight of water-saturated membrane (g), m_d is weight of dried membrane (g), ρ_w is density of water (1000 g/L), V_m is volume of membrane (L) that can be determined by equation (2), and m_{iw} is weight of ceramic membrane in water (g), which is determined by weighing filter underwater.

Ceramic membrane specimen with the size of the 60 mm in diameter and 20 mm thickness was used for compressive strength measurement. Cross-sectional surface of the specimen was ground smoothly then mounted on 300 kN compressive strength testing machine followed by applying a load slowly until specimen was broken. Compressive strength (N/cm^2) was calculated by dividing the load (N) to cross-sectional area (cm^2).

X-ray diffraction (XRD) patterns were collected on the XRD Panalytical Empyrean instrument Cu-Kα source operating at a voltage of 45 kV, current of 40 mA, and scanning step of 0.017°/s with a scanning range from 10 to 80°. The morphology of adsorbent was studied by scanning electron microscopy (SEM) using a Quanta 650 microscope. Nitrogen adsorption/desorption study was investigated using Micromeritics TriStar V6.07 A. Samples were first crushed into small bead and then degassed at 320°C for 5 h prior to analysis. FTIR spectra were collected on a Nicolet iS10 FTIR spectrometer (Thermo Fisher Scientific) using a KBr pellet method. TG-DTA were conducted on STA 409PC-NETZCH under air atmosphere from room temperature to 1000°C with the ramping rate of 10°C/min.

2.4. Bacterial Removal Efficiency. To evaluate the bacterial removal, water was spiked with *E. coli* ATCC suspension (~ 2.1×10^4 CFU/mL) and filtered through a ceramic disk with a constant flow. An aliquot (0.1 mL) of filtered water was taken and stretched over agar plates for cultivation at 37°C for 24–48 h to count for bacterial cells that remained. The bacterial removal efficiency was determined as a percentage of bacteria eliminated by filtration.

3. Results and Discussion

3.1. Porous Ceramic Membrane Characterization. The porosity of a ceramic membrane could be significantly affected by rice husk content used as a pore-forming agent; increasing rice husk would produce high porosity but the strength could be reduced. Thus, porosity and strength of a ceramic membrane should be compromised to maximize its performance. To investigate the effect of rice husk additives on the strength and porosity, the rice husk contents in dry ceramic mixture (including rice husk and kaolin) were varied from 20 to 38 wt% while the firing temperature was kept constant at 1000°C. As the rice husk contents increased from 20 to 35 wt%, the porosity increased from 45.5% to 56.6%, respectively (Figure 1(a)). To further understand the porous structure of membrane, nitrogen adsorption and desorption study was conducted and an adsorption/desorption isotherm of a ceramic membrane prepared with 20% rice husk and fired at 1000°C is shown in Figure 1(b). The isotherm has a hysteresis loop of type H3 according to IUPAC classification. This revealed that the ceramic membrane is associated with macropores [28]. The porosity of pore size in the range of 1.7–300 nm is only 0.025 cm^3/g, and the surface area of membrane is 4.1 m^2/g. Obviously, the pores with size < 300 nm account for a very small fraction in the total porosity of the membrane.

Undoubtedly, higher rice husk content helps improve the porosity of PCMs thanks to more space that rice husk created after being burned out. Higher porosity was expected to benefit water filtration flow rate, but, unfortunately, it caused significant reduction in the strength of the membrane. At rice husks contents ≥ 35 wt%, PCMs were broken apart while installing into the filter or during filtration. As the rice husks decreased to 25 wt%, PCMs can be installed into the filter; however, they have a potential of damage during maintenance, whereas PCMs with 20 wt% rice husks were steady without cracking during installation, filtration, and maintenance. The membranes can be removed for cleaning and reinstalled without damage; therefore, 20 wt% rice husks were selected to investigate the effect of firing temperature on the characteristics of PCMs. Accordingly, the variation in compressive strength as a function of firing temperature was investigated and the results are exhibited in Figure 2(a). It is clear that the compressive strength increased along with the elevation of firing temperature; however, the strength increment rate slightly varied at different temperature ranges. Strength inclined almost linearly from 555.3 N/cm^2 to 1597.0 N/cm^2 in the temperature range from 900°C to 1050°C, with a rate of 6.6 $N/cm^2 \cdot °C$. Nevertheless, when the temperature elevated from 1050°C to 1100°C, the compressive strength increased to 2992.3 N/cm^2 with a rate of 27.9 $N/cm^2 \cdot °C$. This suggests that the possible ceramic phase transition occurred at ≥1050°C, particularly the formation of mullite phase that resulted in the improvement of compressive strength.

The phase transition due to the raising firing temperature was studied by X-ray diffraction, and results are shown in Figure 2(b). Peaks at 16.4°, 30.9°, 33.1°, 35.4°, and 40.8° corresponding to the diffraction of mullite phase (PDF 01-076-2578) are relatively weak intensity at 950°C but become profound at 1000°C and 1050°C. Previous works reported that mullite can be formed at >900°C [24–26] and have an important role in the development of mechanical strength in ceramics [29–31]. The XRD study revealed that the mullite phase was likely formed at temperatures ≥ 950°C. This results explain the reason why the compressive strength of ceramics increased more rapidly at a firing temperature range from 1050°C to 1100°C.

The phase transformation can be further asserted by TG-DTA as shown in Figure 3(a). Both kaolin and rice husk/-kaolin showed weight loss at around 100°C which reflects the moisture vaporization. The kaolin sample had a weight loss at 450°C–600°C with an endothermic peak at 519°C, which related to the removal of structural water in kaolin to form metakaolin and the condensation of ≡Si-OH to form siloxane [32]. Whereas the rice husk/kaolin mixture showed thermal decomposition at lower temperature from 230°C to 600°C, besides an endothermic peak at 519°C, it had two exothermal peaks at 346°C and 453°C corresponding to the release of volatile matter in rice husk and the rice husk combustion [33]. Particularly, an exothermic peak was found at 993°C in both samples that belongs to the formation of mullite crystal [32]. The thermal decomposition of rice husk and condensation of ≡Si-OH are also observed on the FTIR spectra of the sample (Figure 3(b)). A remarkable vibration at 2930 cm^{-1}, 3621 cm^{-1}, and 3697 cm^{-1} corresponding to C-H bonding and -OH group in rice husk disappeared after firing at 1050°C indicating the burning out of rice husk. Moreover, a peak at 915 cm^{-1} was significantly reduced suggesting the condensation of ≡Si-OH groups.

Besides the mullite formation, the PCM structure becomes more condensed at higher firing temperature reflecting via the increase in the diameter shrinkage (Figure 4(a)) and reduction in the porosity (Figure 4(b)). The diameter shrinkage increased almost linearly with temperature, from 1.7% to 9.2%, as temperature increased from 900°C to 1100°C, whereas the porosity decreased slowly at a temperature from 900 to 950°C, 49.4% at 900°C to 48.1% at 950°C, but more rapidly at temperature > 950°C, which remained only 30.2% at 1100°C. The reduction in porosity can also be observed clearly in SEM images. SEM images of PCMs fired at 950°C and 1050°C (Figure 5) showed that a porous structure is formed by the connection of primary particles (quartz and mullite) and voids created by burning off rice husk. Large pores 20–30 μm are found in the sample fired at 950°C but hardly observed at ≥1050°C. Obviously, the improvement of porous ceramic strength along with increasing firing temperature is related to structural condensation and mullite formation. Structural condensation caused noticeable diameter shrinkage and reduction in porosity. These may hinder the

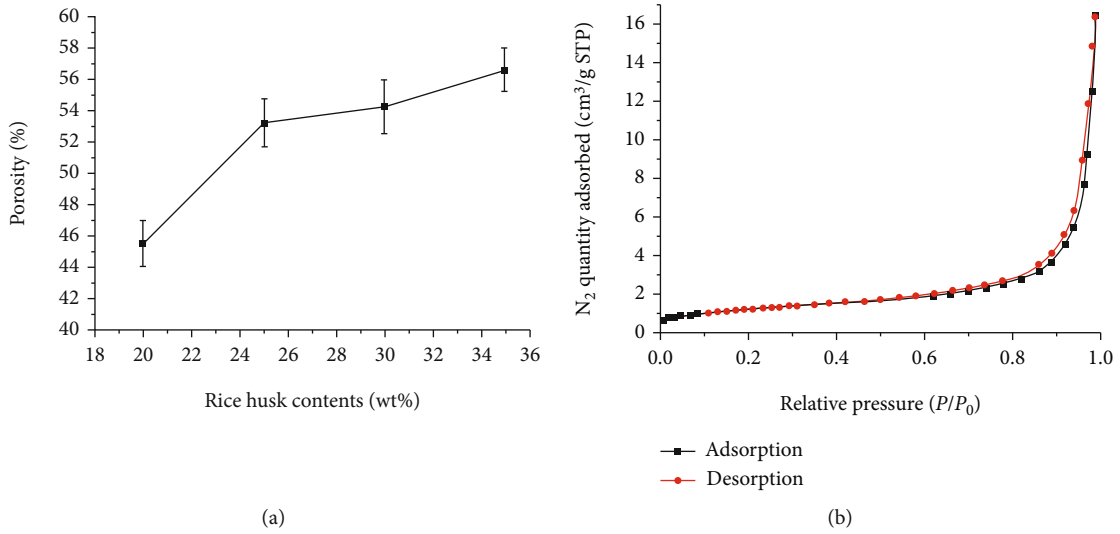

Figure 1: Variation in the porosity of PCMs with rice husk content (wt%) in a ceramic mixture fired at 1000°C (a) and nitrogen adsorption/desorption isotherm of a PCM sample prepared from a ceramic mixture containing 20 wt% rice husk fired at 1000°C (b).

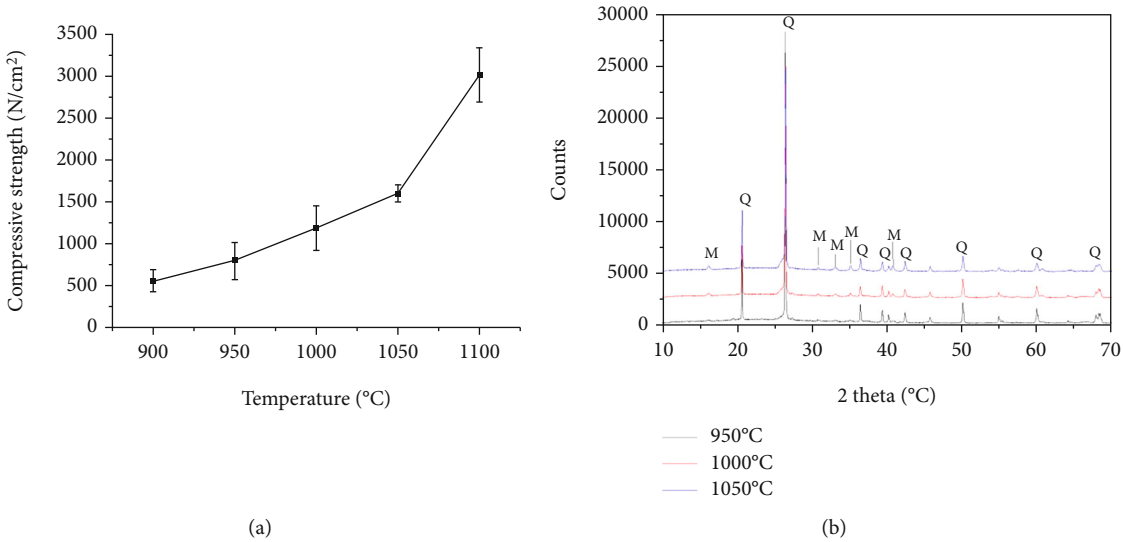

Figure 2: Variation in the compressive strength (a) and X-ray diffraction (b) of PCMs with firing temperatures.

membrane production at large scale and decrease the filtration ability of the membrane; therefore, firing temperature should be optimized to minimize the effect of structural variation on the membrane's performance.

3.2. Bacterial Removal Efficiency. It is apparent as shown in Figure 6 that the removal efficiency of membrane was significantly improved with increasing firing temperature. *E. coli* removal efficiency reached >90% as PCMs were sintered at 900°C and increased to >99% at 1050°C. This removal efficiency is comparable with that of ceramic membrane prepared from clay, laterite, and rice husk and fired at 800–900°C in a previous study, which reached a removal efficiency of approximately 99% [21]. To further evaluate its stability, a membrane fired at 1050°C has been used for the filtration of water spiked with *E. coli* (~ 2.1×10^4 CFU/mL) for 3 days (at least 6 h/day). Interestingly, no significant drop in the bacterial removal efficiency was observed after 3 working days. Obviously, there is a strong relation between porous structure of a PCM and its removal efficiency. Probably, the porous structure was more condensed and large pores created by burned rice husk were constructed to smaller sizes at higher firing temperature resulting in the improvement of *E. coli* removal efficiency. According to the guideline reference level recommended by the World Health Organization, a household water treatment technology that eliminates 2 log of bacteria (equal to 99% removal) can meet the requirement for drinking water at a protective level [34]. Thus, for PCMs

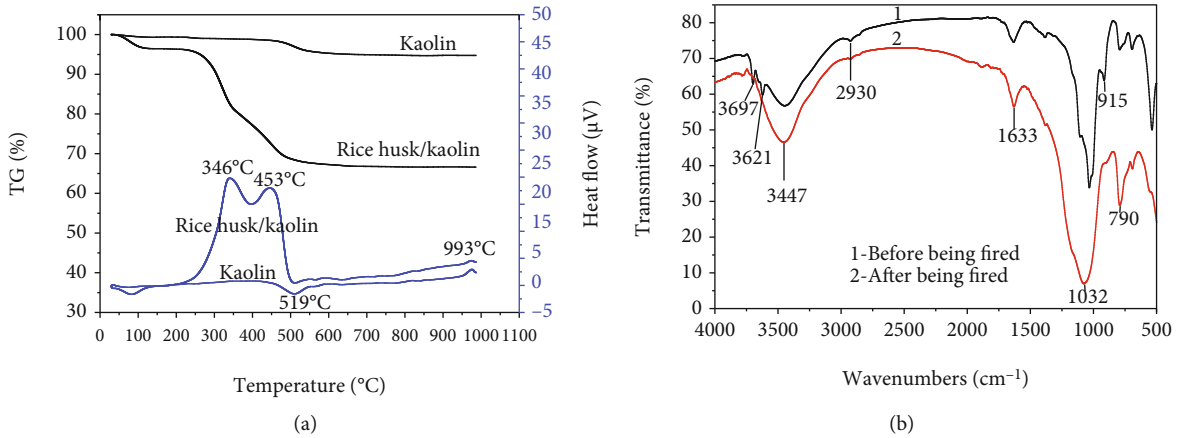

FIGURE 3: TGA and DTA profiles of kaolin and ceramic mixture containing 25% rice husk (a) and FTIR spectra of ceramic samples before and after being fired (b).

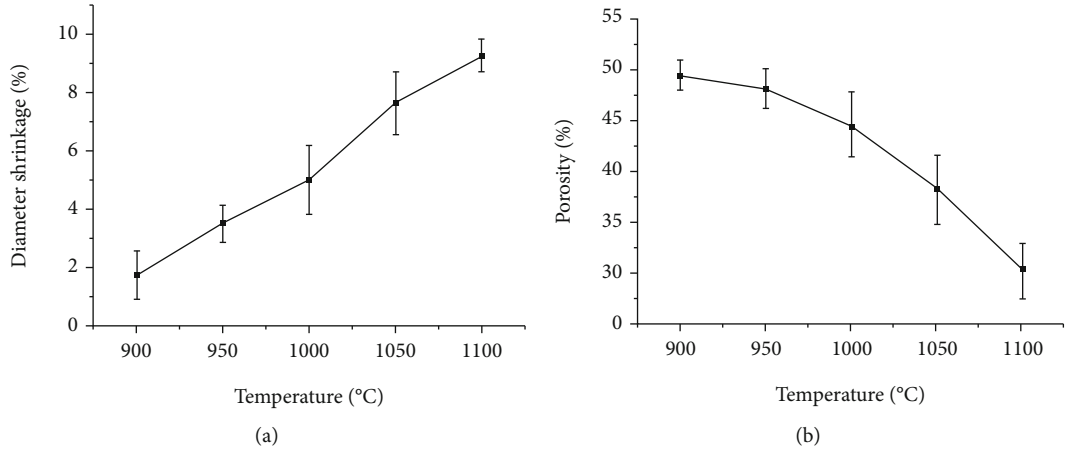

FIGURE 4: Variation in diameter (a) and porosity (b) of PCMs as a function of firing temperature.

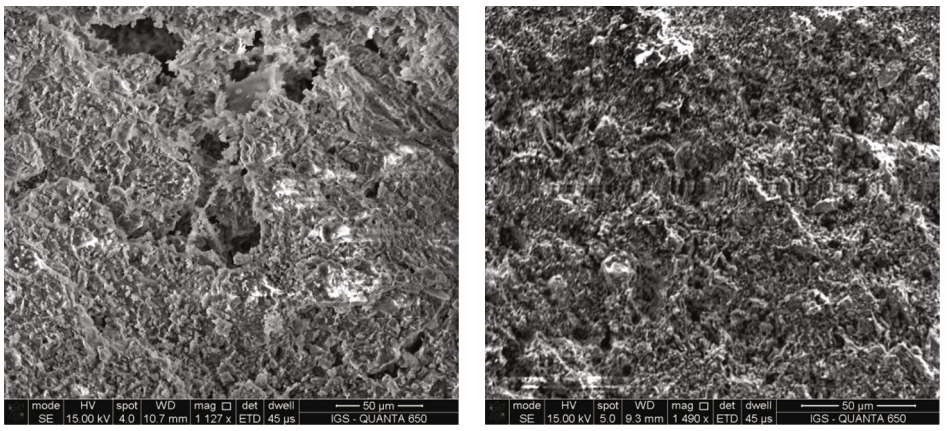

FIGURE 5: SEM images of samples fired at 950°C (a) and 1050°C (b).

prepared from kaolin and 20 wt% rice husk (particle size ≤ 0.5 mm), only membranes fired at ≥1050°C can meet the requirement for a household water treatment technology. This confirmed the importance of firing temperature, which influences not only the strength but also the filtration efficiency of PCMs.

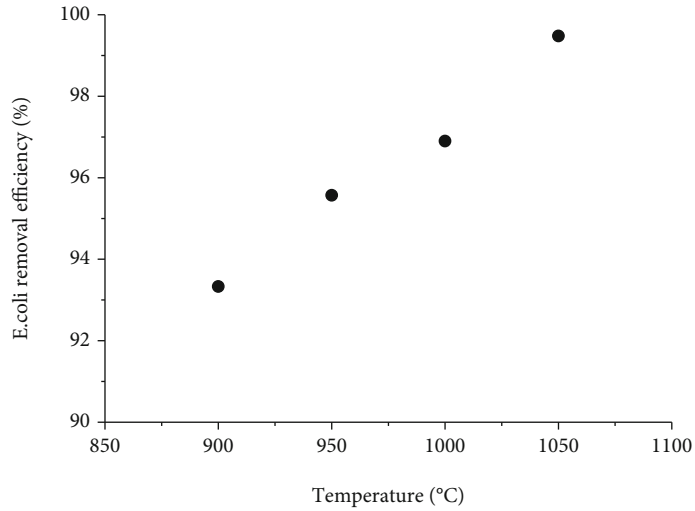

Figure 6: Bacterial removal efficiency by PCMs fired at different temperatures.

4. Conclusion

This study demonstrated an important role of firing temperature in controlling characteristics and filtration performance of PCMs prepared from rice husk and kaolin. Increasing firing temperatures from 900°C to 1100°C generated stronger ceramic membranes with a compressive strength increased from 555.3 to 2992.3 N/cm^2, most likely thanks to the formation of mullite phase. The firing temperature increase caused the ceramic structure condensation, and as a consequence, its porosity decreased from 49.4 to 30.3%, while the diameter of ceramic membrane decreased from 1.7 to 9.2%, respectively. The pore size decrease due to firing temperature increment improved bacterial removal efficiency, which was ~90% at 900°C then reached 99% at 1050°C. The study revealed that the optimum firing temperature should be ~1050°C to balance between strength and filtration efficiency.

Data Availability

The data used to support the findings of this study are available from the corresponding author upon request.

Conflicts of Interest

The authors declare that there is no conflict of interest regarding the publication of this paper.

Acknowledgments

This work is financially supported by a grant from Institute of Environmental Technology, Vietnam Academy of Science and Technology, Vietnam.

References

[1] W. UNICEF, *Progress on Drinking Water and Sanitation: 2017 Update*, World Health Organization, Geneva, Switzerland, 2017.

[2] C. Farrow, E. McBean, G. Huang et al., "Ceramic water filters: a point-of-use water treatment technology to remove bacteria from drinking water in Longhai City, Fujian Province, China," *Journal of Environmental Informatics*, vol. 32, no. 2, 2018.

[3] A. R. Bielefeldt, K. Kowalski, and R. S. Summers, "Bacterial treatment effectiveness of point-of-use ceramic water filters," *Water Research*, vol. 43, no. 14, pp. 3559–3565, 2009.

[4] S. Collin, O. Suntura, S. Cairncross, T. F. Clasen, and J. Brown, "Reducing diarrhea through the use of household-based ceramic water FILTERS: a randomized, controlled trial in rural Bolivia," *The American Journal of Tropical Medicine and Hygiene*, vol. 70, no. 6, pp. 651–657, 2004.

[5] J. Rayner, B. Skinner, and D. Lantagne, "Current practices in manufacturing locally-made ceramic pot filters for water treatment in developing countries," *Journal of Water, Sanitation and Hygiene for Development*, vol. 3, no. 2, pp. 252–261, 2013.

[6] V. A. Oyanedel-Craver and J. A. Smith, "Sustainable colloidal-silver-impregnated ceramic filter for point-of-use water treatment," *Environmental Science & Technology*, vol. 42, no. 3, pp. 927–933, 2008.

[7] K. N. Jackson and J. A. Smith, "A new method for the deposition of metallic silver on porous ceramic water filters," *Journal of Nanotechnology*, vol. 2018, Article ID 2573015, 9 pages, 2018.

[8] A. L. Bulta and G. A. W. Micheal, "Evaluation of the efficiency of ceramic filters for water treatment in Kambata Tabaro zone, southern Ethiopia," *Environmental Systems Research*, vol. 8, no. 1, p. 1, 2019.

[9] B. Ehdaie, C. Krause, and J. A. Smith, "Porous ceramic tablet embedded with silver nanopatches for low-cost point-of-use water purification," *Environmental Science & Technology*, vol. 48, no. 23, pp. 13901–13908, 2014.

[10] T. T. Ngoc Dung, L.-A. Phan Thi, V. N. Nam, T. T. Nhan, and D. V. Quang, "Preparation of silver nanoparticle-containing ceramic filter by _in-situ_ reduction and application for water disinfection," *Journal of Environmental Chemical Engineering*, vol. 7, no. 3, article 103176, 2019.

[11] E. A. Zereffa and T. B. Bekalo, "Clay ceramic filter for water treatment," *Materials Science and Applied Chemistry*, vol. 34, pp. 69–74, 2017.

[12] B. A. Goodman, "Utilization of waste straw and husks from rice production: a review," *Journal of Bioresources and Bioproducts*, vol. 5, no. 3, pp. 143–162, 2020.

[13] C. A. Moraes, I. J. Fernandes, D. Calheiro et al., "Review of the rice production cycle: by-products and the main applications focusing on rice husk combustion and ash recycling," *Waste Management & Research*, vol. 32, no. 11, pp. 1034–1048, 2014.

[14] J. S. Lim, Z. Abdul Manan, S. R. Wan Alwi, and H. Hashim, "A review on utilisation of biomass from rice industry as a source of renewable energy," *Renewable and Sustainable Energy Reviews*, vol. 16, no. 5, pp. 3084–3094, 2012.

[15] I. Quispe, R. Navia, and R. Kahhat, "Energy potential from rice husk through direct combustion and fast pyrolysis: a review," *Waste Management*, vol. 59, pp. 200–210, 2017.

[16] S. P. Parmigiani, F. Vitali, A. M. Lezzi, and M. Vaccari, "Design and performance assessment of a rice husk fueled stove for household cooking in a typical sub-Saharan setting," *Energy for Sustainable Development*, vol. 23, pp. 15–24, 2014.

[17] F. Vitali, S. Parmigiani, M. Vaccari, and C. Collivignarelli, "Agricultural waste as household fuel: techno-economic assessment of a new rice-husk cookstove for developing countries," *Waste Management*, vol. 33, no. 12, pp. 2762–2770, 2013.

[18] A. Kumar, K. Mohanta, D. Kumar, and O. Parkash, "Low cost porous alumina with tailored gas permeability and mechanical properties prepared using rice husk and sucrose for filter applications," *Microporous and Mesoporous Materials*, vol. 213, pp. 48–58, 2015.

[19] R. P. A. Souza, F. V. Motta, R. G. Carvalho et al., "Obtaining ceramic filter from rice husk and kaolinitic clay," *Materials Science Forum*, vol. 802, pp. 232–238, 2014.

[20] K. Mohanta, A. Kumar, O. Parkash, and D. Kumar, "Processing and properties of low cost macroporous alumina ceramics with tailored porosity and pore size fabricated using rice husk and sucrose," *Journal of the European Ceramic Society*, vol. 34, no. 10, pp. 2401–2412, 2014.

[21] A. I. A. Soppe, S. G. J. Heijman, I. Gensburger et al., "Critical parameters in the production of ceramic pot filters for household water treatment in developing countries," *Journal of Water and Health*, vol. 13, pp. 587–599, 2014.

[22] M. F. Serra, M. S. Conconi, M. R. Gauna, G. Suárez, E. F. Aglietti, and N. M. Rendtorff, "Mullite (3Al2O3·2SiO2) ceramics obtained by reaction sintering of rice husk ash and alumina, phase evolution, sintering and microstructure," *Journal of Asian Ceramic Societies*, vol. 4, no. 1, pp. 61–67, 2016.

[23] M. M. Shukur, M. A. Aswad, and S. M. Bader, "Effects of sawdust and rice husk additives on physical properties of ceramic filter," *Journal of University of Babylon for Engineering Sciences*, vol. 26, pp. 221–228, 2017.

[24] Y.-F. Chen, M.-C. Wang, and M.-H. Hon, "Transformation kinetics for mullite in kaolin–Al2O3ceramics," *Journal of Materials Research*, vol. 18, no. 6, pp. 1355–1362, 2003.

[25] D. X. Li and W. J. Thomson, "Kinetic mechanisms for mullite formation from sol-gel precursors," *Journal of Materials Research*, vol. 5, no. 9, pp. 1963–1969, 1990.

[26] K. Okada, "Activation energy of mullitization from various starting materials," *Journal of the European Ceramic Society*, vol. 28, no. 2, pp. 377–382, 2008.

[27] D. V. Halem, *Ceramic silver impregnated pot filters for household drinking water treatment in developing countries, [M.S. thesis]*, Civil Engineering, Faculty of Civil Engineering, Delft University of Technology, 2006.

[28] M. Thommes, K. Kaneko, A. V. Neimark et al., "Physisorption of gases, with special reference to the evaluation of surface area and pore size distribution (IUPAC technical report)," *Pure and Applied Chemistry*, vol. 87, no. 9-10, pp. 1051–1069, 2015.

[29] W. E. Lee, G. P. Souza, C. J. McConville, T. Tarvornpanich, and Y. Iqbal, "Mullite formation in clays and clay-derived vitreous ceramics," *Journal of the European Ceramic Society*, vol. 28, no. 2, pp. 465–471, 2008.

[30] A. Olanrewaju, A. K. Oluseyi, and S. K. Das, "The effect of MgO and Cr2O3on mullite formation from Nigeria sourced kaolin-calcined alumina sintered compacts," *IOP Conference Series: Materials Science and Engineering*, vol. 509, article 012007, 2019.

[31] M. Heraiz, F. Sahnoune, M. Hrairi, N. Saheb, and A. Ouali, "Kinetics of mullite formation from kaolinite and boehmite," *Molecular Crystals and Liquid Crystals*, vol. 628, no. 1, pp. 55–64, 2016.

[32] F. Chargui, M. Hamidouche, H. Belhouchet, Y. Jorand, R. Doufnoune, and G. Fantozzi, "Produccion de mullita a partir de caolin natural y escoria de aluminio," *boletín de la sociedad española de cerámica y vidrio*, vol. 57, no. 4, pp. 169–177, 2018.

[33] A. Chakraverty, P. Mishra, and H. D. Banerjee, "Investigation of thermal decomposition of rice husk," *Thermochimica Acta*, vol. 94, no. 2, pp. 267–275, 1985.

[34] O. World Health, *Evaluating household water treatment options: health-based targets and microbiological performance specifications*, World Health Organization, Geneva, Switzerland, 2011.

Hindawi
Journal of Nanomaterials
Volume 2021, Article ID 9619256, 14 pages
https://doi.org/10.1155/2021/9619256

Research Article

Electrochemical Behavior and Electronucleation of Copper Nanoparticles from $CuCl_2{\cdot}2H_2O$ Using a Choline Chloride-Urea Eutectic Mixture

Thao Dao Vu Phuong,[1,2] Thuy-Linh Phi,[1] Bui Huu Phi,[1] Nguyen Van Hieu,[3,4] Son Tang Nguyen,[5] and Tu Le Manh[1,2]

[1]*Faculty of Materials Science and Engineering, Phenikaa University, Hanoi 12116, Vietnam*
[2]*Advanced Institute for Science and Technology (AIST), Hanoi University of Science and Technology (HUST), No 01, Dai Co Viet Road, Hanoi, Vietnam*
[3]*Phenikaa Research and Technology Institute (PRATI), A&A Green Phoenix Group, 167 Hoang Ngan, Hanoi 100000, Vietnam*
[4]*Faculty of Electrical and Electronic Engineering, Phenikaa Institute for Advanced Study, Phenikaa University, Yen Nghia, Ha-Dong District, Hanoi, Vietnam*
[5]*Faculty of Biotechnology, Chemistry and Environmental Engineering, Phenikaa University, Hanoi 10000, Vietnam*

Correspondence should be addressed to Son Tang Nguyen; son.nguyentang@phenikaa-uni.edu.vn
and Tu Le Manh; tu.lemanh@phenikaa-uni.edu.vn

Received 4 May 2021; Revised 18 June 2021; Accepted 3 July 2021; Published 19 July 2021

Academic Editor: Thanh Dong Pham

This work presents a thorough study on the early stage of copper electrodeposition from a choline chloride-urea deep eutectic solvent (DES). Determination of possible species in DES containing Cu^{2+} ions as the electrolytes has been performed using UV-Vis measurements. Kinetic and thermodynamic aspects of copper electrodeposition on glassy carbon electrode from DES were thoroughly investigated using cyclic voltammetry (CV) and chronoamperometry (CA). Both results from CA and CV have demonstrated that the copper electrodeposition could be performed directly from DES containing a small amount of water by the single potentiostatic step technique. Theoretical approach confirmed that the direct electronucleation of copper nanoparticles in the DES can be described by a model with two contributions, namely, (i) adsorption process and (ii) a three-dimensional (3D) nucleation and diffusion-controlled growth of copper nuclei, to the total current density transients. Kinetic parameters are important for controlling morphology and chemical composition of the obtained nanoparticles, which are verified by surface characterization techniques such as SEM and EDS.

1. Introduction

Copper nanoparticles (Cu-NPs) are of great interest for applications in many engineering fields, including electronics, energy, catalyst, environment, and agriculture, owing to their natural abundance, low cost, and diversity of preparation methods [1, 2]. Some (typical) examples can be mentioned such as the use of Cu-NPs in sensors [3], fuel cell, and solar cell [4, 5] and in conductive inks for printed electronics [6]. In agriculture, Cu-NPs have also shown important effect in regulating plant growth and development and increasing chlorophyll formation and seed production [7]. Moreover, due to their fungicidal and insecticidal activity against the pests of crop plants, they can be used as nano-pesticides, nano-herbicides, nano-fertilizers [8, 9], among others. These benign behaviors of Cu-NPs make the study on their synthesis a topic of current interest.

It is known that Cu-NPs can be produced by different routes, physical methods, or chemical methods [10]. The main concern is the fact that these methods are neither cost-effective nor eco-friendly due to the use of toxic

chemicals [11]. The electrochemical synthesis of Cu-NPs from a "green" solvent such as a deep eutectic solvent (DES) based on choline chloride could be a promising candidate to tackle these problems.

DESs have received much attention for metals electrodeposition applications (i.e., Ni, Fe, Al, and Zn [12–16]) due to several advantages, such as a wide electrochemical window, low cost, ease of preparation, negligible vapor pressure, thermal stability, and (nearly) null hydrogen liberation during electrodeposition [17, 18], compared to conventional aqueous solvents. Particularly, in the case of copper, although the copper electrodeposition from DESs has been reported in the literatures [19, 20], insights on the early stages of this process, specifically, mechanistic and kinetic aspects, are still limited. Abbott et al. [19] have first studied the copper electrodeposition in the eutectic mixture of choline chloride and ethylene glycol (ethaline) and found that copper reduction occurs via two well separated one-electron stages: Cu(II)-Cu(I)-Cu. These processes have been studied by Sebastián et al. [20] using Cu(I) and Cu(II) solutions dissolved in aqueous solvent and in the mixture of choline chloride and urea (reline), DES. They proposed the use of the double potentiostatic step technique to separate current densities related to the reduction of each copper species. However, there have been some concerns in the application of this technique and unsolved problems as follows: (i) it can be facilitated in a medium with the low mobility of species (such as the reline DES under their studied conditions), but it is difficult in medium with the good mobility of ionic species (i.e., aqueous medium); (ii) success of the procedure is dependent on control of the initial conditions at which electrodeposition takes place [20], (iii) effect of residual water in DES has not been considered, while several recent papers [21, 22] have reported that a small amount of water can influence physiochemical properties, the dynamics, and the electrochemistry of active species, (i.e., decreasing the viscosity and resistivity of the DES and altering the speciation of the copper chloro-complexes) [22, 23]; and (iv) although Sebastian et al. [20] have reported some initial results on the copper electronucleation in DES using cyclic voltammetry (CV) and chronoamperometry (CA), insights on the mechanisms and kinetics including mathematical models capable of describing the Cu nucleation and growth processes from DES in practical conditions where it can contain some unavoidable small amounts of residual water adsorbed from the environment or DES preparation, and some important kinetic parameters such as the nucleation frequency, A, the number density of active sites for copper nucleation onto the electrode surface, N_0, have been not determined. Consequently, the knowledge on these aspects must be updated; in addition, (v) details on the speciation of copper ions dissolved in DES and the possibility of using the conventional potentiostatic method to electrodeposit copper from DES have not yet been studied.

Therefore, the aim of this work is to study the nucleation and growth mechanisms and kinetics of copper deposition process on glassy carbon electrode from the reline containing Cu^{2+} ions as the electrolyte solution using both theoretical and experimental approaches. UV-Vis spectra were used to analyze the species containing in Cu^{2+} electrolyte solution.

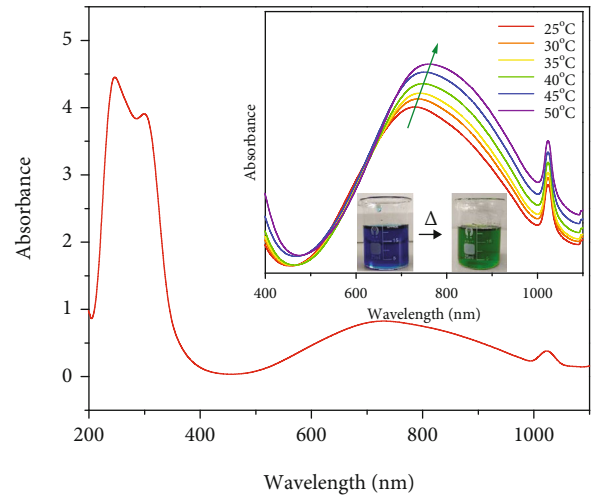

FIGURE 1: UV-Vis-NIR spectra of 10 mM of $CuCl_2{\cdot}2H_2O$ in reline at different temperatures. The inset depicts the shift to the right-hand side of the NIR region, indicating the color change recorded in the system.

2. Materials and Methods

2.1. DES and Electrolyte Preparation. Chemicals such as choline chloride ($C_5H_{14}ClNO$, 97%, Sigma-Aldrich), urea (CH_4N_2O, 99%, Sigma-Aldrich), and copper (II) chloride hexahydrate ($CuCl_2{\cdot}2H_2O$, ACS reagent, ≥99.0%) were used. DES was prepared by mixing choline chloride and urea in a 1 : 2 molar ratio at 100°C. This obtained mixture was constantly stirred until a transparently homogenous solution was obtained. Details of DES preparation can be found in our previous study [24]. The Cu^{2+} electrolyte solution was obtained by adding 50 mM copper (II) chloride hexahydrate salt, to the DES, and the solution was stirred for 12 hours at 60°C. The obtained electrolyte solution was kept in a dehumidifier for latter electrochemical measurements. The water content of $CuCl_2{\cdot}2H_2O$ dissolved in DES was measured by Karl Fischer coulometric titration, using a Titrino Coulometer (Model 756, Metrohm), giving a value of about 0.35%.

2.2. UV-Vis Measurements. UV-Vis measurements of the electrolytes containing Cu(II) dissolved in DES were performed in an UV-Vis spectrophotometer (UV-6850, JENWAY Double Beam Spectrophotometer). UV-Vis spectra of the solution were obtained for different temperature (25°C to 50°C) in a quartz cell with a light path length of 1.0 cm using the Prism 5.51 PC software coupled to the equipment.

2.3. Electrochemical Tests. A conventional water-jacketed cell comprising three electrodes was used for CV and CA tests. The electrochemical cell was composed of a glassy carbon electrode (GCE), with 0.0707 cm^2 surface area as the working electrode, a platinum wire, and a silver wire as counter and

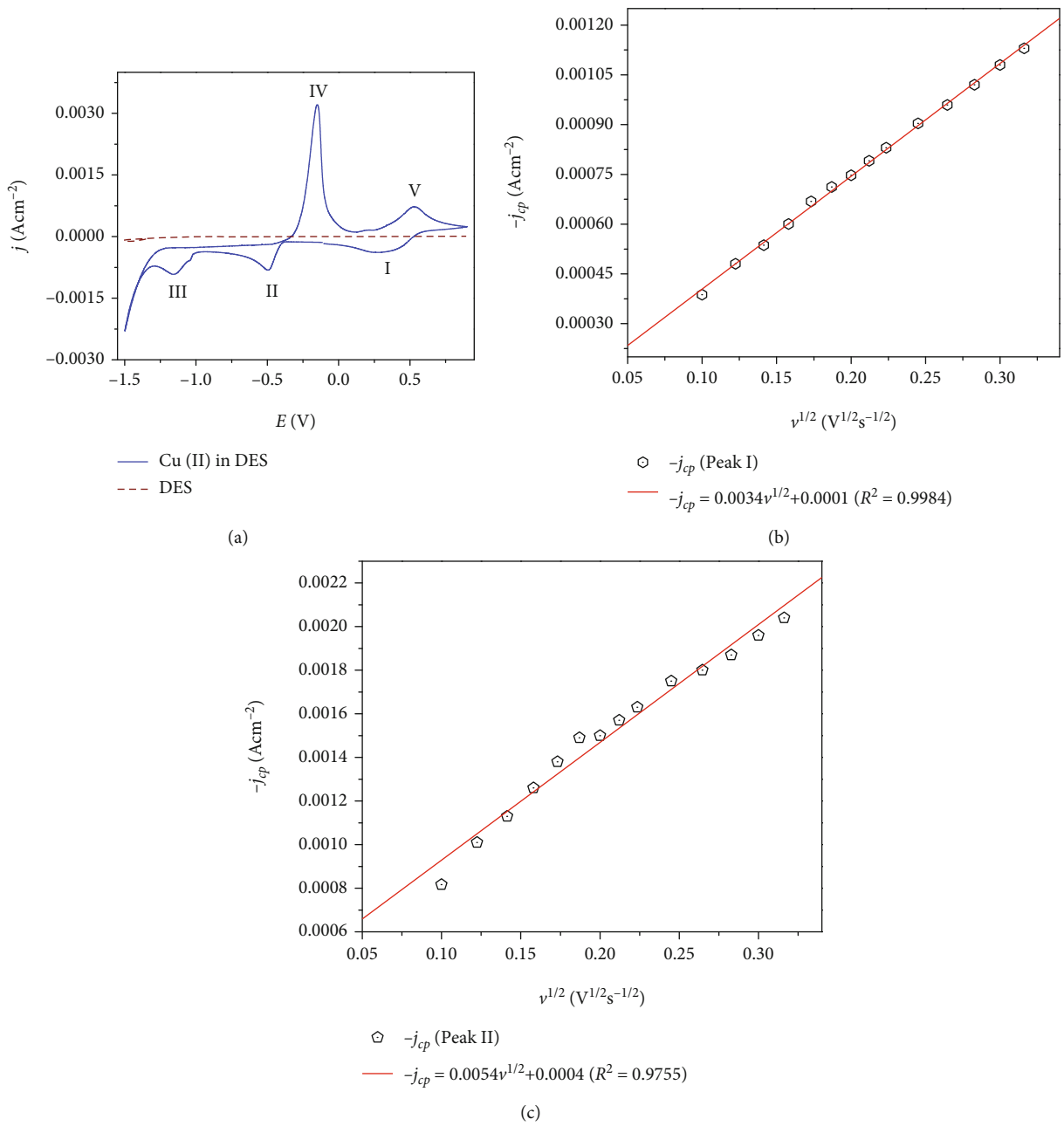

Figure 2: Continued.

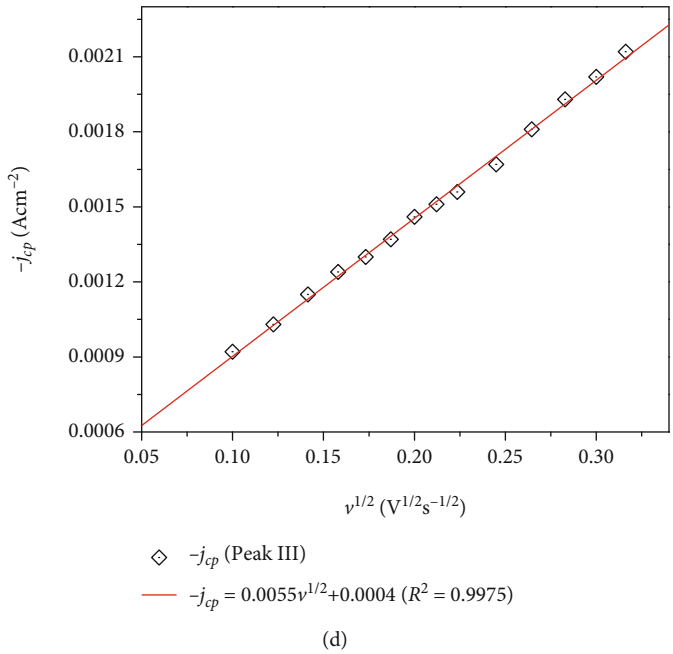

FIGURE 2: (a) CVs obtained in the system GCE/DES (discontinuous curve) and GCE/50 mM Cu(II) in DES (blue curve) at 70°C. The scan was started at a potential of 0.40 V in the negative direction with a scan rate of 10 mVs^{-1}. CVs recorded onto GCE using different scan rates and cathodic peak current density (j_{cp}) as a function of the scan rate ($v^{1/2}$) at 70°C for (b) peak I, (c) peak II, and (d) peak III.

quasi reference electrode, respectively. The electrochemical cell temperature was controlled by a Lauda RMS 179 Circulator with RM6 Refrigerating Water Bath Chiller, −15 to 100°C (with a temperature stability of ±0.02°C). CA and CV measurements were carried out using VersaStat 3 system, coupled to the VersaStudio software installed in a PC for experimental control and data collection. These experiments were performed at 70°C.

2.4. Surface Analysis Characterization. Morphological and chemical compositions of the electrodeposits were characterized using field emission scanning electron microscope (FE-SEM), Model JEOL JSM SEM 7000F, and energy-dispersive X-ray spectroscopy (EDS), respectively, to confirm the existence of Cu-NPs on the GCE surface.

3. Results and Discussion

3.1. Copper Speciation in the Reline. A drastic change in color of Cu^{2+} ions dissolved in DES from blue to green before and after heating (see Figure 1) can be observed with the naked eyes. The green color of the Cu^{2+} electrolyte solution remains unchanged and becomes stable after heating. This phenomenon is able to be recorded by UV-Vis spectra as shown in Figure 1. It reveals two peaks in the UV region, at 246 nm and 298 nm, which can be assigned to the presence of species such as $[CuCl_4]^{2-}$ [25]. Meanwhile, in the near infrared (NIR) region, a broader peak between from 705 to 755 nm and a sharp peak at 1022 nm are detected, which can be due to the presence of $[Cu(H_2O)_6]^{2+}$ species [26]. By increasing the temperature, the absorbance peaks tend to shift to higher value of wavelength (inset of Figure 1). These results confirm the presence of different complexes in DES such as $[Cu(H_2O)_6]^{2+}$ and $[CuCl_4]^{2-}$ species corresponding to room temperature and higher temperature, respectively. Thus, at room temperature, $[Cu(H_2O)_6]^{2+}$ can be predominant due to the small amount of residual water in DES, which is due to the use of $CuCl_2{\cdot}2H_2O$ salt and/or atmospheric moisture. After heating, this water tends to evaporate, and Cl^- ions can substitute (partially) the H_2O ligands to form $[CuCl_4]^{2-}$ complexes. The color change of $CuCl_2$ solution in choline chloride-based DESs has been also observed in other studies [22, 26], where $CuCl_2$(hyd.) dissolved in ethaline exhibits yellow color, typical of forming $[CuCl_4]^{2-}$ species, and by adding water to the solution it shifts from yellow to blue. According to Valverde et al. [22] and Vreese et al. [26], this color change can be explained due to the substitution of Cl^- by H_2O ligand. Therefore, the general species of $CuCl_2{\cdot}2H_2O$ dissolved in reline could be presented in form of the mixed chloro-aqua chemical complex structure $[CuCl_n(H_2O)_m]^{(2-x)-}$, where $n + m = 4 \longrightarrow 6$ and $x = 0 \longrightarrow 6$ [22, 26].

3.2. CV Study. Figure 2(a) shows the CVs recorded on the GCE in DES (discontinuous curve of Figure 2(a)) and with 50 mM Cu^{2+} ions dissolved in DES at 70°C. It can be seen that the (current density) contribution of the pure DES is insignificant and can be neglected. Several peaks (I, II, IV, and V) observed in Figure 2(a) correspond to different electrochemical reactions of Cu^{2+} in DES occurring on the GC electrode surface. In the forward scan of the CV, three reduction peaks are clearly observed in the potential ranges from 0.6 V to -0.1 V (peak I), -0.4 V to -0.86 V (peak II), and from -1.0 V to -1.30 V (peak III).

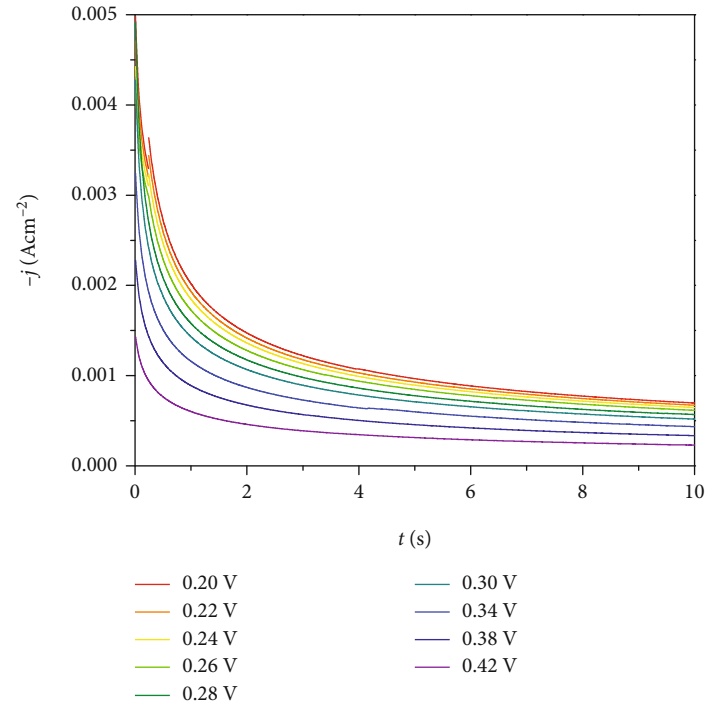

(a)

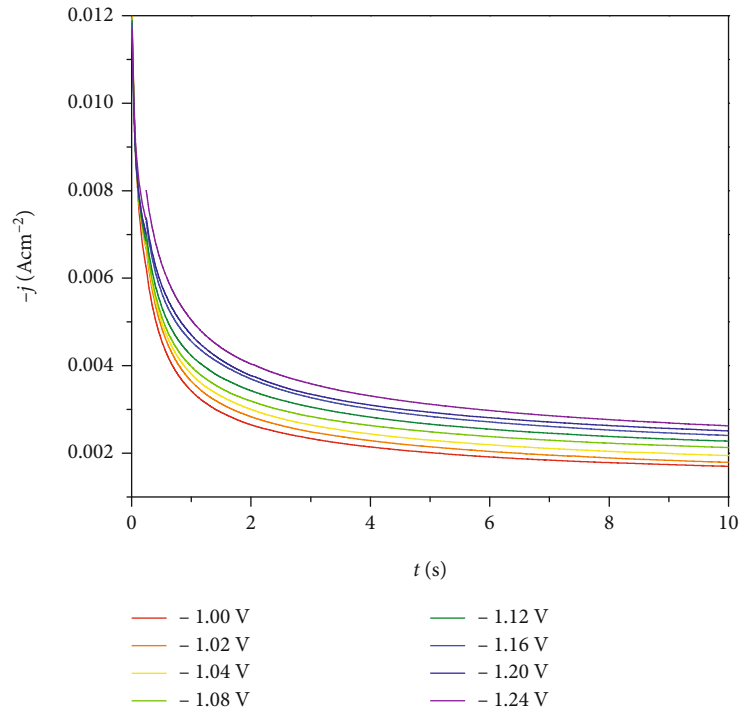

(b)

Figure 3: Continued.

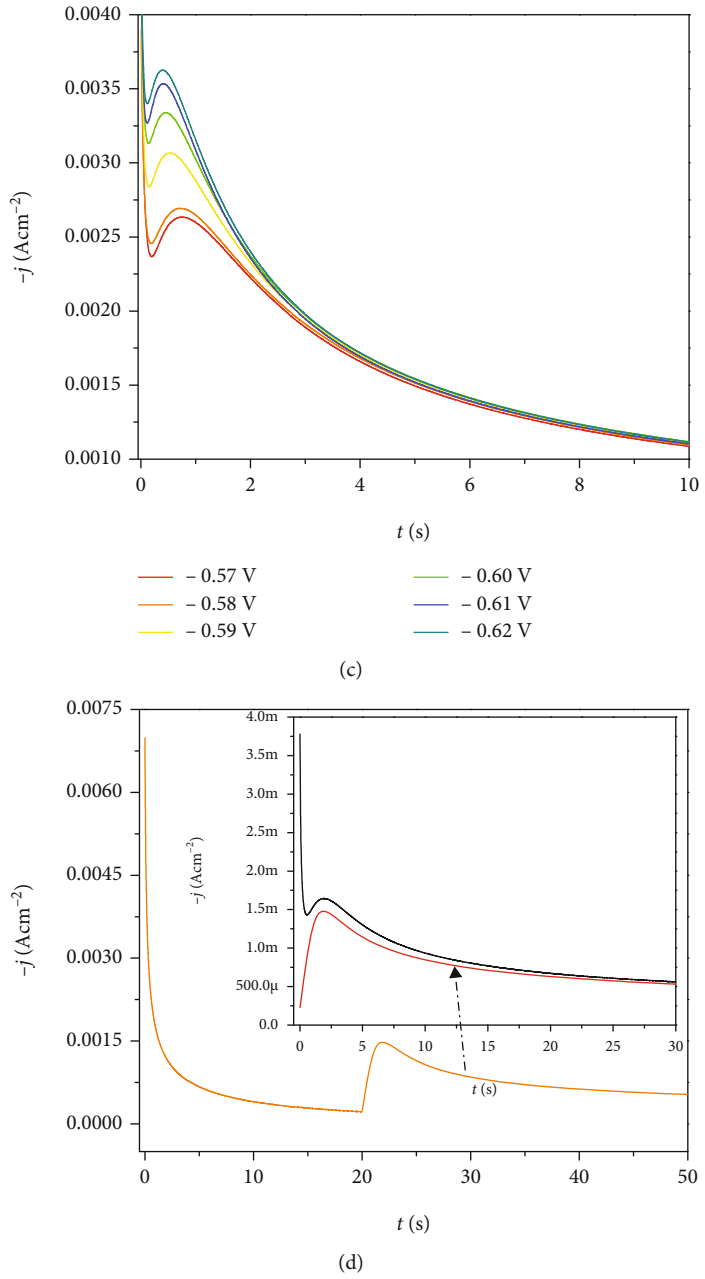

Figure 3: CAs recorded in the system GCE/50 mM Cu(II) in DES at 70°C using different potentials located at the region closed to (a) peak I, (b) peak III, and (c) peak II, defined by the CV depicted in Figure 2(a), and (d) comparison between the experimental CAs at -0.52 V using single potential step and double potential step (applying first step from -0.1 V, then the second step -0.52 V (red line) as shown in the inset).

According to Sebestian et al. [20], the first two peaks can be assigned to the transition process from Cu^{2+} to metallic Cu associated with the reactions, (1) and (2):

$$Cu^{2+}{}_{DES} + e - \longrightarrow Cu^{+}{}_{DES} \quad (1)$$

$$Cu^{+}{}_{DES} + e^{-} \longrightarrow Cu_{(s)} \quad (2)$$

The water reduction reaction to hydrogen associated with peak III observed in the CV (Figure 2(a)) can be given by (3) [23]:

$$2H_2O_{DES} + 2e^{-} \longrightarrow H_2 + 2OH^{-} \quad (3)$$

Meanwhile, in the backward scan, the oxidation peak located in the potential range of -0.40 V to 0.05 V can be attributed to the oxidation reaction of Cu metallic nuclei

(see (4)) previously formed by (2) during the forward scan. The other peak located at 0.28 V–0.80 V (peak V) can be associated with the oxidation reactions of Cu^{+}_{DES} from (1), as given in (5).

$$Cu_{(s)} \longrightarrow Cu^{+}_{DES} + e^{-} \quad (4)$$

$$Cu^{+}_{DES} \longrightarrow Cu^{2+}_{DES} + e^{-} \quad (5)$$

At potentials larger than the potential ranges of peaks III and V, at the extremes of the CV, the current intensity growths are known as the decomposition reactions (reduction and oxidation, respectively) of the solvent [17, 27]. Since this work deals with the copper electronucleation, the reduction reactions, such as (1) and (2), are paid more attention.

To investigate the electrochemical behavior of the system GCE/50 mM Cu(II) in DES, CVs are carried out at different scan rates ranging from 10 to 100 mVs^{-1}. It reveals that cathodic peak current density (j_{cp}) increments with as the scan rate increases. By plotting j_{cp} as a function of square root of the scan rate ($v^{1/2}$) for three peaks I, II, and III (see Figures 2(b)–2(d)), it can be clearly seen that j_{cp} of these peaks exhibits a linear relationship with $v^{1/2}$. This means that the Cu electrodeposition on GCE from DES follows a diffusion-controlled mechanism, which can be described by the Berzins-Delahay equation [28]:

$$j_{cp} = \frac{0.61 \times (Fn)^{3/2} C_0 (Dv)^{1/2}}{(RT)^{1/2}}, \quad (6)$$

where F is the Faraday constant, R is the ideal gases constant, n is the total number of electrons transfer, C_0 (mol cm^{-3}) is the bulk concentration of reduced species, D ($cm^2\,s^{-1}$) is the diffusion coefficient of Cu(II) ions, and T (K) is the temperature of medium.

According to the CV, copper electrodeposition mechanism must be occurred in two steps through (1) and (2). Therefore, from peaks I and II of interest, there are two values of diffusion coefficient to be determined, D_I and D_{II}, correspondingly. D_I can be calculated from Eq. (6) and using the slopes of Figure 2(b) and the initial concentration $C_0 = 0.05$ M; thus, $D_I = 9.9536 \times 10^{-8}\,cm^2\,s^{-1}$. D_{II} is more difficult to determine since Cu^{+} concentration is unknown. Fortunately, in the same DES, concentration, and working temperature, Sebastian et al. [29] have proposed a methodology to estimate the surface concentration (C_s) of Cu^{+} ions using the double step technique, which yields $C_s = 0.01694$ M. Taking into account the C_s and the slope values of Figure 2(c), from Eq. (6), it can be derived $D_{II} = 8.67 \times 10^{-7}\,cm^2\,s^{-1}$ for peak II. These values are consistent with those reported by Sebastian et al. [20] and Popescu et al. [30]. A significant increase in the value of D from peak I to peak II can be explained due to the transition from species Cu^{2+} to Cu^{+} (see (1)) as D is inversely proportional to their atomic radius. This follows the Stokes-Einstein equation as discussed by Mejia-Caballero et al. [31] in the case of chromium.

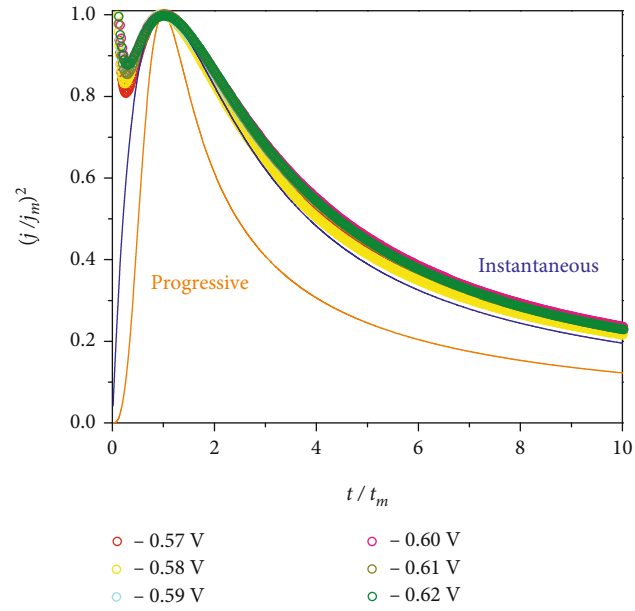

Figure 4: Comparison of the nondimensional plots of the experimental CAs (scatter line) depicted in Figure 3(c) with the theoretical ones for instantaneous (blue) and progressive (orange) nucleation.

3.3. Potentiostatic Study. Figure 3 depicts CA curves recorded on the GCE at 70°C using the potential range defined from CV (Figure 2(a)). In general, a clear distinction of nucleation mechanisms can be observed from CAs of the studied reduction peaks. Figures 3(a) and 3(b) depict the CAs with a typical Cotrellian behavior, while the CA shapes of Figure 3(c) suggest that the early stage of the Cu electrodeposition onto GCE from DES could follow the three-dimensional (3D) nucleation and diffusion-controlled growth [32]. This demonstrates that direct electrodeposition of copper from DES is evident by simply using the single potential step. The direct electrodeposition of copper in this work refers to the single potential step or the conventional chronoamperometry, by applying only one potential pulse to deposit copper from Cu^{2+} to Cu, as be illustrated by the following mechanism, (7):

$$Cu^{2+} + e^{-} <=> Cu^{+} + e^{-} <=> Cu \quad (7)$$

In difference with Sebastian et al. [20], who have stated that (7) could be difficult, Figure 3(d) clearly indicates that both (single and double pulse) techniques can be performed successfully to electrodeposit copper from DES in our case. Interestingly, while the double potentiostatic steps can separate the reduction reactions of each copper species, the single pulse seems to be more advantageous by shortening the reaction time of (1), transition from Cu^{2+} to Cu^{+}, which results in a more complex shape of the experimental CA with an additional (adsorption) contribution to the total current transient density. This process can be explained due to the presence of the residual water containing in the DES, which significantly influences

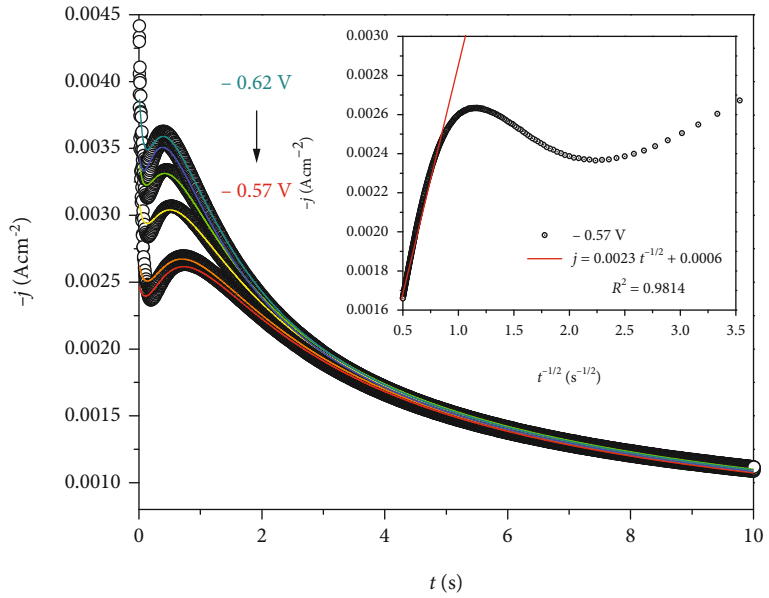

Figure 5: Comparison between the CAs (circle) (lines) recorded in the system GC/50 mM $CuCl_2$ in DES at the potentials (from -0.57 to -0.62 V with a step = −0.01 V), and the theoretical transients (line) obtained after fitting Eq. (12) to the experimental data. The inset of Figure 5 illustrates the Cottrell analysis ($j - t^{-1/2}$ plot) of the CA at -0.57 V.

Table 1: Best-fit parameters obtained from fitting Eq. (12) to the experimental data.

$-E$ (V)	$10^3 P_1$ (A $s^{1/2}$ cm^{-2})	P_2 (s^{-1})	A (s^{-1})	$10^3 P_4$ (Acm^{-2})	P_5 (s^{-1})	$10^{-6} N_0$ (cm^{-2})	$10^7 D$ (cm^2 s^{-1})	$10^{-7} AN_0$ (s^{-1} cm^{-2})
0.57	3.394 ± 0.002	1.065 ± 0.093	4.031 ± 0.072	2.492 ± 0.028	1.267 ± 0.158	9.232 ± 0.806	3.889 ± 0.005	3.722 ± 0.075
0.58	3.424 ± 0.002	1.143 ± 0.071	3.894 ± 0.079	2.647 ± 0.021	1.391 ± 0.132	9.741 ± 0.605	3.956 ± 0.005	3.793 ± 0.081
0.59	3.463 ± 0.002	1.346 ± 0.081	4.902 ± 0.123	3.117 ± 0.020	1.668 ± 0.148	11.217 ± 0.667	4.047 ± 0.005	5.499 ± 0.141
0.60	3.482 ± 0.002	1.533 ± 0.102	5.594 ± 0.128	3.428 ± 0.024	1.880 ± 0.174	12.632 ± 0.840	4.091 ± 0.005	7.066 ± 0.166
0.61	3.428 ± 0.002	1.746 ± 0.146	6.899 ± 0.126	3.486 ± 0.030	2.102 ± 0.235	14.846 ± 1.241	3.966 ± 0.005	10.242 ± 0.196
0.62	3.463 ± 0.002	2.519 ± 0.058	6.578 ± 0.461	3.982 ± 0.025	3.540 ± 0.261	20.976 ± 0.483	4.049 ± 0.005	13.799 ± 0.967

the dynamics and the electrochemistry of active species as shown in Figure 1.

Paying attention to peak II, Figure 3(c) reveals that the peak current densities of the system GCE/Cu^{2+} in DES increase with the increase of the applied potentials. For the determination of the governed nucleation types (instantaneous or progressive nucleation) in the Cu electrodeposition process onto the GCE, a nondimensional analysis is performed using the theoretical plots, which are well-known as Scharifker and Hills models [33].

$$\left(\frac{j}{j_m}\right)^2 = 1.9542\left(\frac{t}{t_m}\right)^{-1}\left(1-\exp\left[-1.2564\left(\frac{t}{t_m}\right)\right]\right)^2,$$
$$\left(\frac{j}{j_m}\right)^2 = 1.2254\left(\frac{t}{t_m}\right)^{-1}\left(1-\exp\left[-2.3367\left(\frac{t}{t_m}\right)^2\right]\right)^2. \quad (8)$$

Figure 4 reveals that at 70°C, for $t/t_m \leq 0.7$ and $t/t_m \geq 2.1$, the nondimensional plots of the experimental current density transients are above the instantaneous one, which is out of the validated zone of the 3D nucleation and diffusion-controlled growth [33]. According to [31], the classic form of the Scharifker and Mostany (SM) model is not applicable, and a modified one based on the SM could be convenient.

Table 2: Diffusion coefficient calculated using the Cottrellian behavior (see the parameter P_1 in Eq. (9)) for different reduction peaks.

Cottrell analysis	Peak I	Peak II
$10^7 D$ (cm^2 s^{-1})	2.0452	7.9493

The parametric form of the SM model associated with the 3D nucleation and growth is given by [31]:

$$j(t)_{3D} = P_1 t^{-1/2}\left(1-\exp\left\{-P_2\left[t-\frac{1-\exp\left(-P_3 t\right)}{P_3}\right]\right\}\right), \quad (9)$$

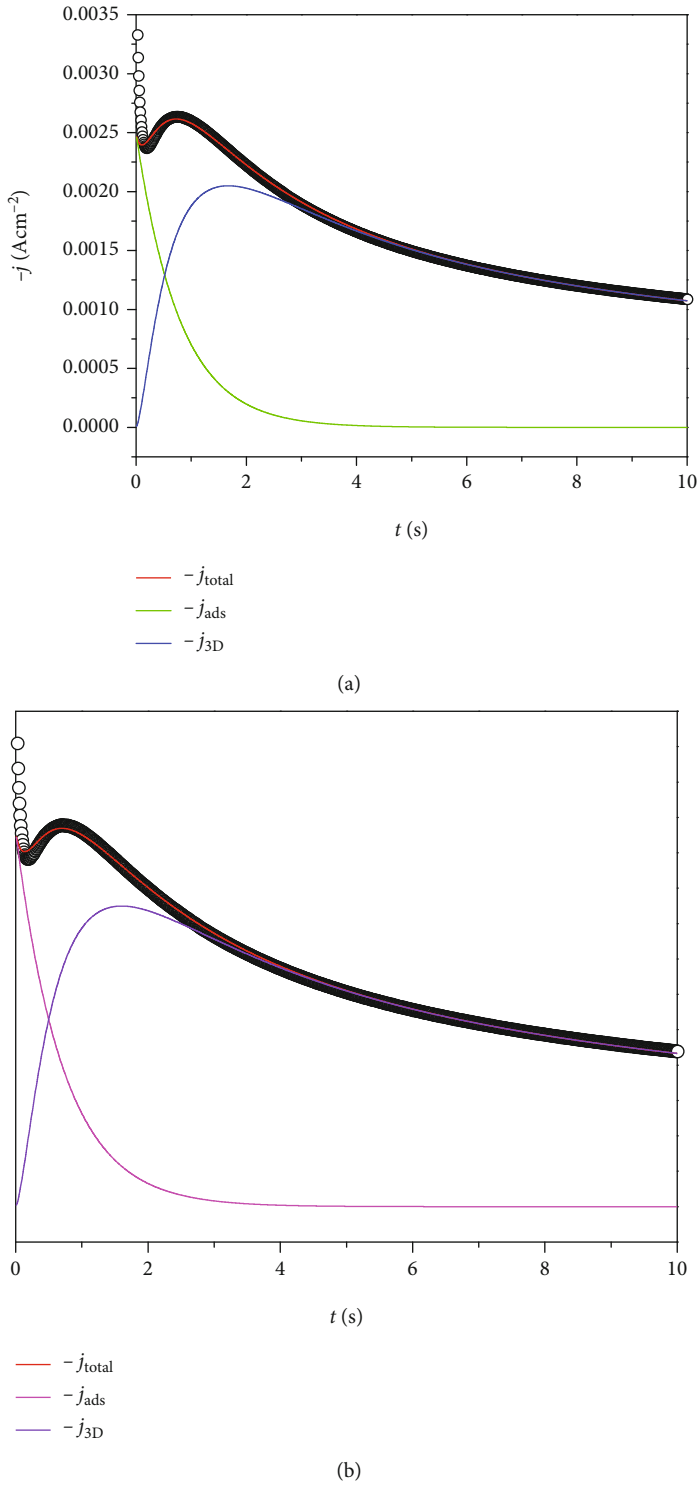

FIGURE 6: Separation of individual contributions to the total current density transient using Eq. (12) for different applied potentials: (a) -0.57 V; (b) -0.58 V.

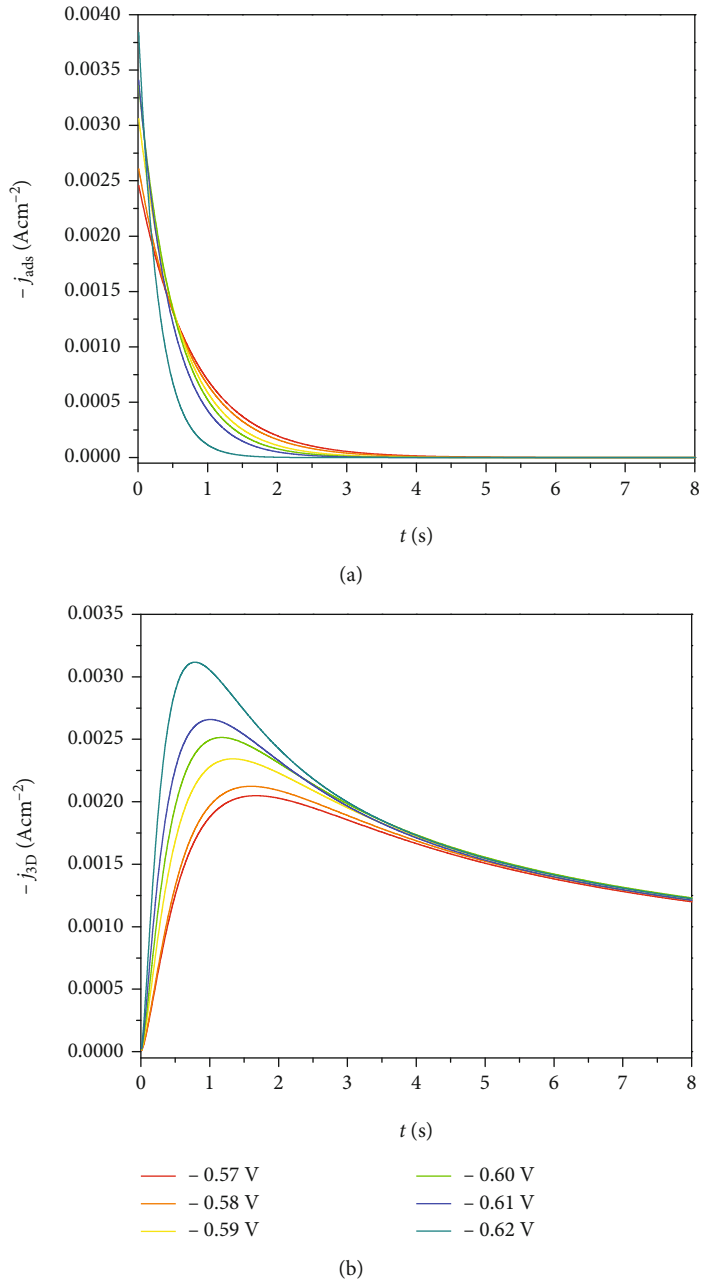

FIGURE 7: Individual contributions of adsorption and 3D nucleation derived from Eq. (12) for CA curves obtained in Figure 5.

where

$$P_1 = \frac{z\mathrm{F}\mathrm{D}^{1/2}C_0}{\pi^{1/2}},$$
$$P_2 = N_0\pi D\left(\frac{8\pi MC_0}{\rho}\right)^{1/2}, \quad (10)$$
$$P_3 = A,$$

where ρ is the density of the Cu deposit and M is its atomic mass, N_0 is the number density of active sites on the electrode surface, and A (s^{-1}) is the nucleation frequency per active site.

The adsorption contribution can be expressed by [31]:

$$j(t)_{\text{ads.}} = P_4 \exp(-P_5 t),$$
$$P_4 = \frac{E}{R_s}, \quad (11)$$
$$P_5 = \frac{1}{R_s C},$$

where E is the applied potential (V), R_s is the solution's resistance (Ω), and C is double layer capacitance (F). Therefore, total contribution to the current density transients shown in Figure 4 is given by:

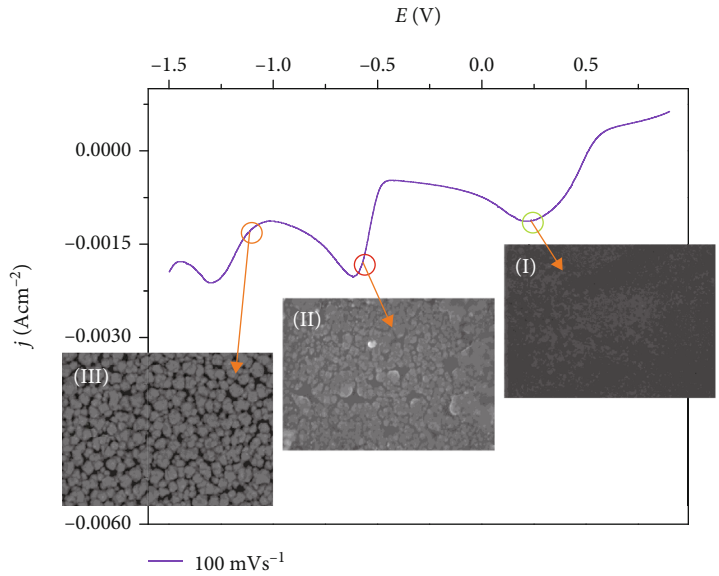

Figure 8: Analysis of GCE surfaces at different applied potentials selected from the CV.

$$j(t)_{\text{total}} = j(t)_{\text{ads.}} + j(t)_{\text{3D}}. \quad (12)$$

Figure 5 displays the comparison between the experimental CAs and the theoretical plots using Eq. (12). The good agreement between these plots means that Eq. (12) is suitable for the description of experimental CAs. Moreover, the derived kinetic parameters, as shown in Table 1, such as A and N_0 are consistent with the trend of metallic nucleation as observed in the literature [24, 30, 34]. Thus, AN_0 product increases with the increase of the potential, confirming the validity of the proposed model. Besides, the average value of the diffusion coefficient, D, is in order $4 \times 10^{-7}\,\text{cm}^2\,\text{s}^{-1}$, which is lower than the result obtained from the CV. However, this is acceptable because it is consistent with several works [24, 29] reported on electrodeposition of other metals in the same DES. Therefore, the use of other methods is necessary as can be seen latter in Cottrell analysis.

To verify the results obtained by CV and Eq. (9), a Cottrell analysis was done to derive the diffusion coefficient from CAs by linearization of longer time after the peak (the falling part) of the transients depicted in Figure 5. Thus, according to the procedure given in to Palomar-Pardave et al. [34] when $t >> t_m$ the transient follows the Cottrell equation (see the red line in the inset of Figure 5), in contrast ($t < t_m$) the CA deviates from that behavior. The diffusion coefficients calculated for the transients of the three peaks are shown in Table 2. It reveals that in general the average values of D are higher than the previous results from the CV and fitting Eq. (9) to experimental data. But they are still in the order and agree with the CV method in the increasing trend of D as the potential becomes more negative.

Applying Eq. (12), it is possible to separate the individual contribution of adsorption and 3D nucleation + diffusion-controlled growth of copper in DES to the total current density transients, as shown in Figure 6. It clearly shows that the current densities corresponding to the adsorption effect (Figure 7(a)) tend to reduce as the potential becomes more negative (increasing in magnitude), while the (peaks) current densities related to $j(t)_{\text{3D}}$ (Figure 7(b)) increase with the applied potentials. These results validate that the use of the proposed model is suitable for the case of copper electrodeposition on the GCE from reline DES.

3.4. SEM and EDS. Figure 8 shows SEM images of GCE surfaces obtained after electrodeposition with the applied potentials corresponding to region associated with different reduction peaks I, II, and III. It reveals clearly that peak I exhibits a surface with the absence of metallic copper, black color, the same color as seen in a bare GCE surface (see Figure 9(a)), while both peaks II and III result in formation of (copper) NPs, which are verified by EDS spectra depicted in the right-hand side of Figures 9(a)–9(c). But it seems to be not efficient using the potentials at peak III due to the hydrogen evolution reaction (see (3)). Moreover, these verify the reduction reactions proposed in the CV analysis. Thus, according to the speciation results and the mechanisms derived from CV and modeling analysis, the nanoparticles observed in Figure 9(c) should be associated with the mixture of $Cu/Cu(OH)_2$ as the core/shell structure due to the presence of OH- ions in (3), as similar to the mechanism of Ni electrodeposition from reline reported in other studies [35, 36]. As suggested from the SEM image depicted in Figure 9(b) showing the formation of metallic (copper) nuclei with different sizes and ages, the copper electrodeposition process onto the GCE from DES containing a small amount of water follows to the progressive nucleation mechanism. This could be explained due to the contribution of the adsorption process, which occurs first in the short time of the CA, giving rise to the formation of the first nuclei on the electrode surfaces.

It is worth mentioning that the Cu-NPs obtained using the potential around peak II are denser than those obtained from peak III giving more porous and larger particle size.

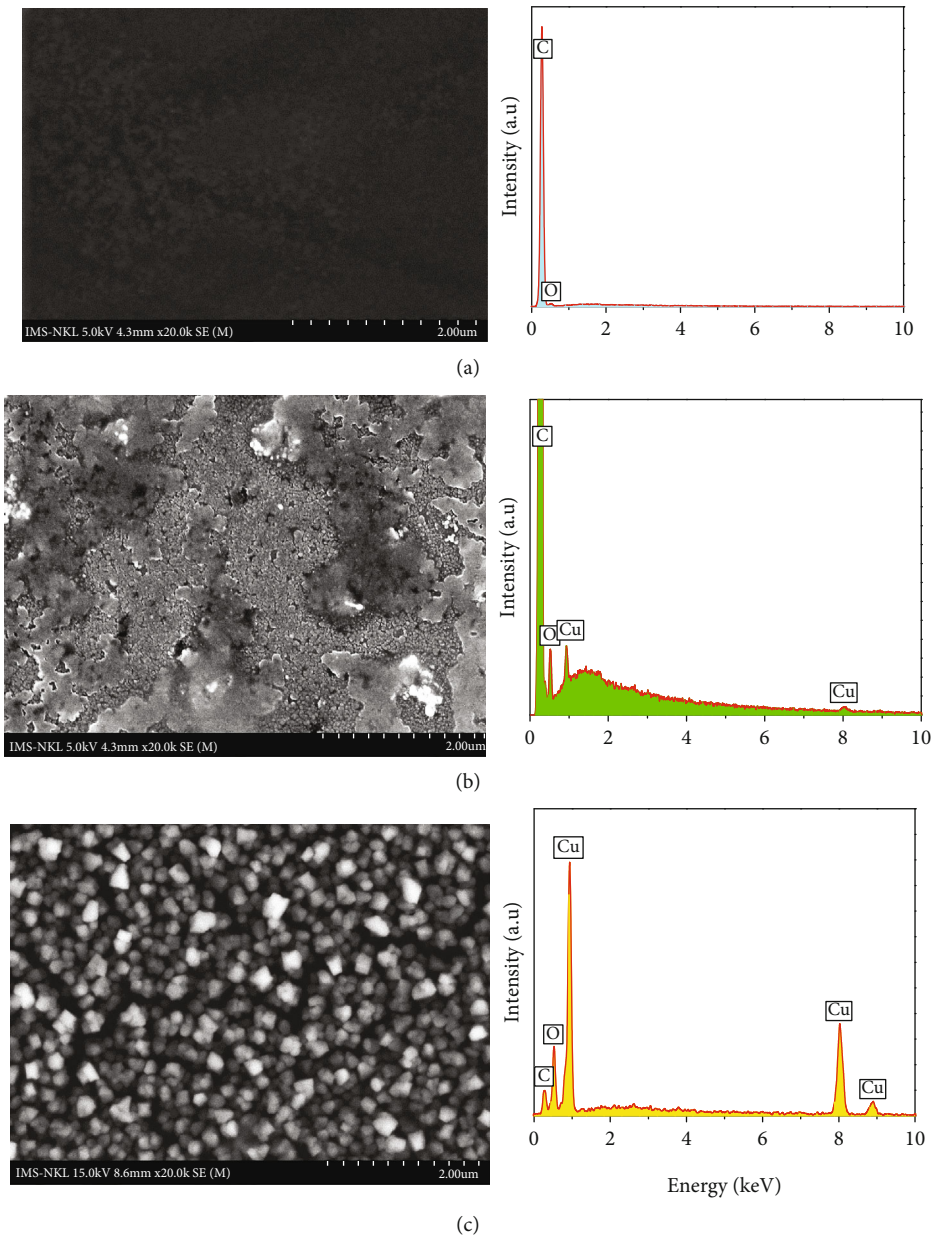

FIGURE 9: SEM images showing Cu-NPs and their corresponding EDS spectra obtained on the GCE surfaces at different reduction peaks using an applied potential of (a) -0.4 V during 3600 s, (b) -0.61 V during 60 s, and (c) -1.1 V during 3600 s at 70°C.

This is extremely useful for further applications (i.e., biosensors, microelectromechanical systems, and MEMS) of the copper electrodeposition from DES since one can select the (appropriate) conditions to obtain desired surface morphology, structure, and chemical composition.

4. Conclusions

The electrochemical synthesis of Cu-NPs from DES reline (containing a small amount of water, ~0.35%) was thoroughly studied. From the UV-Vis spectra measurements, a sudden change in color of Cu^{2+} electrolytes solution from blue to green was observed by heating the solution from room temperature to above 40°C. This can be associated with the presence of complex species such as $[CuCl_n(H_2O)_m]^{(2-x)-}$, where $n + m = 4 - 6$ and $x = 0 - 6$. A wider potential range (compared to the literature) observed from the recorded CV on the system GCE/50 mM Cu(II) in DES, which exhibits more complex behavior with three reduction peaks (see (1), (2), and (3)). By means of the CA technique, it was possible to distinguish the electrochemical behavior of these processes, indicating that peak I corresponds to the reduction of intermediate (soluble) species (Cu(II) to (Cu(I)), (1)); peak II corresponds to the formation of metallic copper from soluble species ((Cu(I)) to Cu(0), (2)), and peak III could be occurring simultaneously both reactions, namely, hydrogen

evolution reaction of small amount of water containing in DES and (2). From these results, it has verified that the copper electrodeposition can be performed by the single potentiostatic step route. A model, comprising two contributions, 3D nucleation and diffusion-controlled growth + adsorption, was proposed and validated to explain the copper electrodeposition on the GCE from the reline DES. These kinetic and mechanistic aspects play the key role in controlling morphology, structure, and chemical composition of Cu-NPs, which are verified by surface characterization techniques using SEM and EDS. Finally, SEM images have verified that the copper electrodeposition from DES containing a small amount of water follows the progressive nucleation mechanism.

Data Availability

The data used to support the findings of this study have not been made available because it is part of an undergoing project.

Conflicts of Interest

The authors declare that they have no conflicts of interest.

Acknowledgments

This research is funded by the Vietnam National Foundation for Science and Technology Development (NAFOSTED) under grant number 103.02-2019.28.

References

[1] M. B. Gawande, A. Goswami, F. X. Felpin et al., "Cu and Cu-based nanoparticles: synthesis and applications in catalysis," *Chemical Reviews*, vol. 116, no. 6, pp. 3722–3811, 2016.

[2] M. I. Din, F. Arshad, Z. Hussain, and M. Mukhtar, "Green adeptness in the synthesis and stabilization of copper nanoparticles: catalytic, antibacterial, cytotoxicity, and antioxidant activities," *Nanoscale Research Letters*, vol. 12, no. 1, p. 638, 2017.

[3] G. Eranna, B. Joshi, D. Runthala, and R. Gupta, "Oxide materials for development of integrated gas sensors—a comprehensive review," *Critical Reviews in Solid State and Materials Sciences*, vol. 29, no. 3-4, pp. 111–188, 2004.

[4] H. M. Zhang, W. Xu, G. Li, Z. M. Liu, Z. C. Wu, and B. G. Li, "Assembly of coupled redox fuel cells using copper as electron acceptors to generate power and its in-situ retrieval," *Scientific Reports*, vol. 21059, 2016.

[5] F. Parveen, B. Sannakki, M. V. Mandke, and H. M. Pathan, "Copper nanoparticles: synthesis methods and its light harvesting performance," *Solar Energy Materials and Solar Cells*, vol. 144, pp. 371–382, 2016.

[6] S. Magdassi, M. Grouchko, and A. Kamyshny, "Copper nanoparticles for printed electronics: routes towards achieving oxidation stability," *Materials (Basel)*, vol. 3, no. 9, pp. 4626–4638, 2010.

[7] D. V. Nguyen, H. M. Nguyen, N. T. Le et al., "Copper nanoparticle application enhances plant growth and grain yield in maize under drought stress conditions," *Journal of Plant Growth Regulation*, pp. 1–12, 2021.

[8] M. T. el-Saadony, M. E. Abd el-Hack, A. E. Taha et al., "Eco-friendly synthesis and insecticidal application of copper nanoparticles against the storage pest Tribolium castaneum," *Nanomaterials (Basel)*, vol. 10, no. 3, p. 587, 2020.

[9] M. Rai, A. P. Ingle, R. Pandit et al., "Copper and copper nanoparticles: role in management of insect-pests and pathogenic microbes," *Nanotechnology Reviews*, vol. 7, no. 4, pp. 303–315, 2018.

[10] E. Masarovicova and K. Kralova, "Metal nanoparticles and plants/nanocząstki metaliczne I rośliny," *Ecological Chemistry and Engineering S*, vol. 20, no. 1, pp. 9–22, 2013.

[11] A. Umer, S. Naveed, N. Ramza, and M. S. Rafique, "Selection of a suitable method for the synthesis of copper nanoparticles," *Nano*, vol. 7, no. 5, p. 1230005, 2012.

[12] P. Huang and Y. Zhang, "Electrodeposition of nickel coating in choline chloride-urea deep eutectic solvent," *International Journal of Electrochemical Science*, vol. 13, pp. 10798–10808, 2018.

[13] A. S. C. Urcezino, L. P. M. dos Santos, P. N. S. Casciano, A. N. Correia, and P. de Lima-Neto, "Electrodeposition study of Ni coatings on copper from choline chloride-based deep eutectic solvents," *Journal of the Brazilian Chemical Society*, vol. 28, no. 7, pp. 1193–1203, 2017.

[14] T. L. Manh, E. M. Arce-Estrada, I. Mej'ıa-Caballero et al., "Iron electrodeposition from Fe(II) ions dissolved in a choline chloride: urea eutectic mixture," *Journal of the Electrochemical Society*, vol. 165, no. 16, pp. D808–D812, 2018.

[15] E. R. Clemente, T. L. Manh, C. E. G. Pano et al., "Aluminum electrochemical nucleation and growth onto a glassy carbon electrode from a deep eutectic solvent," *Journal of the Electrochemical Society*, vol. 166, no. 1, pp. D3035–D3041, 2019.

[16] L. Vieira, A. H. Whitehead, and B. Gollas, "Mechanistic studies of zinc electrodeposition from deep eutectic electrolytes," *Journal of the Electrochemical Society*, vol. 161, no. 1, pp. D7–D13, 2014.

[17] E. L. Smith, A. P. Abbott, and K. S. Ryder, "Deep eutectic solvents (DESs) and their applications," *Chemical Reviews*, vol. 114, no. 21, pp. 11060–11082, 2014.

[18] A. P. Abbott, G. Capper, D. L. Davies, R. K. Rasheed, and V. Tambyrajah, "Novel solvent properties of choline chloride/urea mixtures," *Chemical communications*, no. 1, pp. 70-71, 2003.

[19] A. P. Abbott, K. E. Ttaib, G. Frisch, K. J. McKenzie, and K. S. Ryder, "Electrodeposition of copper composites from deep eutectic solvents based on choline chloride," *Physical Chemistry Chemical Physics*, vol. 11, no. 21, pp. 4269–4277, 2009.

[20] P. Sebastián, E. Vallés, and E. Gómez, "Copper electrodeposition in a deep eutectic solvent. First stages analysis considering Cu(I) stabilization in chloride media," *Electrochimica Acta*, vol. 123, pp. 285–295, 2014.

[21] V. S. Protsenko, A. A. Kityk, D. A. Shaiderov, and F. I. Danilov, "Effect of water content on physicochemical properties and electrochemical behavior of ionic liquids containing choline chloride, ethylene glycol and hydrated nickel chloride," *Journal of Molecular Liquids*, vol. 212, pp. 716–722, 2015.

[22] P. E. Valverde, T. A. Green, and S. Roy, "Effect of water on the electrodeposition of copper from a deep eutectic solvent," *Journal of Applied Electrochemistry*, vol. 50, no. 6, pp. 699–712, 2020.

[23] E. A. M. Cherigui, K. Sentosun, and M. H. Mamme, "On the control and effect of water content during the

electrodeposition of Ni nanostructures from deep eutectic solvents," *The Journal of Physical Chemistry. A*, vol. 122, no. 40, pp. 23129–23142, 2018.

[24] T. D. V. Phuong, L. M. Quynh, N. N. Viet et al., "Effect of temperature on the mechanisms and kinetics of cobalt electronucleation and growth onto glassy carbon electrode using reline deep eutectic solvent," *Journal of Electroanalytical Chemistry*, vol. 880, p. 114823, 2021.

[25] C. Amuli, M. Elleb, J. Meullemeestre, M. J. Schwing, and F. Vierling, "Spectrophotometric study of copper(I1) chloride-trimethyl phosphate solutions. Thermodynamic and spectroscopic properties of copper(II) chloro complexes in nonaqueous solutions," *Inorganic Chemistry*, vol. 25, no. 6, pp. 856–861, 1986.

[26] P. D. Vreese, N. R. Brooks, K. V. Hecke et al., "Speciation of copper(II) complexes in an ionic liquid based on choline chloride and in choline chloride/water mixtures," *Inorganic Chemistry*, vol. 51, no. 9, pp. 4972–4981, 2012.

[27] Q. Zhang, K. D. Vigier, S. Royer, and F. Jerome, "Deep eutectic solvents: syntheses, properties and applications," *Chemical Society Reviews*, vol. 41, pp. 7108–7146, 2012.

[28] T. Berzins and P. Delahay, "Oscillographic polarographic waves for the reversible deposition of metals on solid electrodes," *Journal of the American Chemical Society*, vol. 75, no. 3, pp. 555–559, 1953.

[29] P. Sebastián, E. Torralba, E. Vallés, A. Molina, and E. Gómez, "Advances in copper electrodeposition in chloride excess. A theoretical and experimental approach," *Electrochimica Acta*, vol. 164, pp. 187–195, 2015.

[30] A. M. Popescu, A. Cojocaru, C. Donath, and V. Constantin, "Electrochemical study and electrodeposition of copper(I) in ionic liquid-reline," *Chemical Research in Chinese Universities*, vol. 29, no. 5, pp. 991–997, 2013.

[31] I. Mejıa-Caballero, J. A. Gonzalez, T. L. Manh et al., "Mechanism and kinetics of chromium electrochemical nucleation and growth from a choline chloride/ethylene glycol deep eutectic solvent," *Journal of the Electrochemical Society*, vol. 165, no. 9, pp. D393–D401, 2018.

[32] B. R. Scharifker and J. Mostany, "Three-dimensional nucleation with diffusion controlled growth: part I. Number density of active sites and nucleation rates per site," *Journal of Electroanalytical Chemistry*, vol. 177, no. 1-2, pp. 13–23, 1984.

[33] B. Scharifker and G. Hills, "Theoretical and experimental studies of multiple nucleation," *Electrochimica Acta*, vol. 28, no. 7, pp. 879–889, 1983.

[34] M. Palomar-Pardavé, B. R. Scharifker, E. M. Arce, and M. Romero-Romo, "Nucleation and diffusion-controlled growth of electroactive centers: reduction of protons during cobalt electrodeposition," *Electrochimica Acta*, vol. 50, no. 24, pp. 4736–4745, 2005.

[35] A. Parsa and H. Heli, "Electrodeposition of nickel wrinkled nanostructure from choline chloride:urea deep eutectic solvent (reline) and application for electroanalysis of simvastatin," *Microchemical Journal*, vol. 152, p. 104267, 2020.

[36] J. Aldana-González, M. Romero-Romo, J. Robles-Peralta et al., "On the electrochemical formation of nickel nanoparticles onto glassy carbon from a deep eutectic solvent," *Electrochimica Acta*, vol. 276, pp. 417–423, 2018.

Hindawi
Journal of Nanomaterials
Volume 2021, Article ID 9312358, 6 pages
https://doi.org/10.1155/2021/9312358

Research Article

Hydrothermal Synthesis of Li_2MnO_3-Stabilized $LiMnO_2$ as a Cathode Material for Li-Ion Battery

Ngoc Hung Vu,[1,2] **Van-Duong Dao**,[1,2] **Hong Ha Thi Vu**,[1,2] **Nguyen Van Noi**,[3] **Dinh Trinh Tran**,[3] **Minh Ngoc Ha**,[3] **and Thanh-Dong Pham**[3]

[1]*Faculty of Biotechnology, Chemistry and Environmental Engineering, Phenikaa University, Hanoi 10000, Vietnam*
[2]*Phenikaa Research and Technology Institute (PRATI), A&A Green Phoenix Group, 167 Hoang Ngan, Hanoi 10000, Vietnam*
[3]*Faculty of Chemistry, University of Science, Vietnam National University, 334 Nguyen Trai, Thanh Xuan, Hanoi, Vietnam*

Correspondence should be addressed to Ngoc Hung Vu; hung.vungoc@phenikaa-uni.edu.vn

Received 25 May 2021; Accepted 26 June 2021; Published 12 July 2021

Academic Editor: Domenico Acierno

Herein, we reported the composite structure of $LiMnO_2$ and Li_2MnO_3 as a low-cost and environmentally benign cathode material. This composite with the main phase of $LiMnO_2$ (90%) was synthesized by hydrothermal method at 220°C from LiOH and $Mn(CH_3COO)_2$ precursors. The obtained nanosized $LiMnO_2$-$LiMnO_3$ cathode material exhibits a high capacity of 265 mAh g^{-1} at C/10. The incorporation of Li_2MnO_3 into the $LiMnO_2$ phase could stabilize the structure, leading to the improved cycle stability of the cathode. The capacity retention of the cathode was 93% after 80 cycles at C/2. Our results facilitate a potential strategy for developing high-performance cathode materials based on the Li-Mn-O system.

1. Introduction

Although lithium-ion batteries (LIBs) have a dominant position as the power source in mobile electronics, they still do not meet the growing demand for these power-consuming devices [1]. In addition, the reduction of product costs, including production costs and treatment costs that affect the environment after disposal, is of considerable concern to manufacturers. Accordingly, the use of inexpensive and environmentally friendly commercial cathode materials such as $LiMn_2O_4$ and $LiFePO_4$ takes precedence over $LiCoO_2$ under these conditions [2, 3]. Compared with Fe-based materials, Mn-based materials have a higher range of working potential and conductivity. Accordingly, there are many other Mn-based materials that are studied such as $LiMnO_2$, Li_2MnO_3, $Li_4Mn_5O_{12}$, and $Li_4Mn_2O_5$ and their composites [4–8]. These materials exhibit superior capacity than available commercial cathode materials and are expected to fulfill the requirement in electric vehicle application. Freire et al. [9] reported that a rock-salt structure of $Li_4Mn_2O_5$ which is synthesized by a mechanochemical synthesis method could deliver a high capacity of 355 mAh g^{-1}. Liu et al. [10] reported the synthesis of $Li_4Mn_5O_{12}$ at low temperature by solid-state reaction, and the cathode could deliver a high capacity of 212 mAh g^{-1}. Li_2MnO_3 has the highest theoretical capacity among others (485 mAh g^{-1}), and it has been extensively studied in the Li-rich layered oxide system (LLO) as a structural stabilizer and a capacity booster. On the other hand, $LiMnO_2$ also has high theoretical capacity of 285 mAh g^{-1}. It has a lot of metastable states including orthorhombic (*o*-$LiMnO_2$, space group *Pmmn*), monoclinic (*m*-$LiMnO_2$, space group *C*2/*m*), and layered $LiMnO_2$ (space group *R*3*m*) with α-$NaFeO_2$-like structure. Among these structures, the *o*-$LiMnO_2$ is the most stable. However, the single phase of Mn-based compounds, such as Li_2MnO_3, $LiMnO_2$, or $Li_4Mn_5O_{12}$, cannot be used as a cathode material for LIBs due to their structural instability. As a way to overcome some of these difficulties, compounds derived from the substitution of Mn by Ni and Co have been studied. The other way is designing a composite structure between them. The LLO, which is $xLi_2MnO_3{\cdot}(1\text{-}x)LiMO_2$ (M = Mn, Ni, Co), has more than two decades of investigation [11–13]. To promote using standing Mn-based materials, we investigate the stabilization of Li_2MnO_3 for $LiMnO_2$ as cathode materials for LIBs.

2. Experimental

The integrated structure was synthesized by a hydrothermal method. First, manganese (II) acetate tetrahydrate (4.9 g, Sigma-Aldrich) and lithium hydroxide monohydrate (3.36 g, Sigma-Aldrich) were dissolved in distilled water (40 mL) separately. Then, hydrogen peroxide (H_2O_2, 30% (w/w) in H_2O, 1.6 mL) was added to the Li solution before adding Mn solution slowly. The mixture was mixed with methanol (20 mL) and stirred for 0.5 h. Subsequently, it was located into a Teflon-lined autoclave for the hydrothermal reaction at 220°C for 12 h. Finally, the powder was centrifuged and washed with ethanol and distilled water thoroughly.

The phase of the sample was identified by X-ray diffraction (XRD) measurements using Philips X'Pert with Cu-Kα radiation in a range of $10° \leq 2\theta \leq 100°$. The morphology of particles was recorded by scanning electron microscopy (SEM, Nova NanoSEM 450) and high-resolution transmission electron microscopy (HRTEM, JOEL JEM-2100F). The oxidation state of elements was determined by X-ray photon spectroscopy (XPS, K-Alpha+ Thermo Scientific). The chemical composition was analyzed by ICP (Optima 8300 ICP-OES spectrometer).

For cathode fabrication, the active material (70 wt%), Ketjen black (10 wt%), and teflonized acetylene black (binder, 20 wt%) were mixed thoroughly. Then, it was pressed onto a stainless-steel mesh and dried at 120°C under vacuum for 12 h. For coin-cell (2032 coin-type cell) fabrication, the cathode, an electrolyte (1 M $LiPF_6$ solution in a 1 : 1 mixture of ethylene carbonate and dimethyl carbonate), a separator, and Li metal were assembled in an Ar-filled glovebox. The cell was tested of its electrochemical properties by a Neware Battery Tester between 2.0 and 4.8 V vs. Li^+/Li.

3. Results and Discussion

3.1. Structural Characterization of Cathode. Figure 1 shows the XRD pattern of the synthesized sample. All peaks can be indexed according to the space group *Pmmn* of the orthorhombic $LiMnO_2$ structure. There is a slightly weak peak that appears at ~18.3°, which is assignable to the Li_2MnO_3 phase (space group *C*2/*m*). This second phase originated from the oxidation decomposition reaction [14]. All peaks are sharp, indicating the high crystallinity of particles. Note that the ratio of $LiMnO_2$ to Li_2MnO_3 phase can be changed by using an oxidizing agent [15] or controlling the synthesis temperature [16]. The ICP result shows that the ratio of Li : Mn = 1.095 : 1 due to the existence of the Li_2MnO_3 phase. Rietveld refinement is performed using the model shown in Table 1. The main phase is *o*-$LiMnO_2$ with space group *Pmmn*, and the second phase is Li_2MnO_3 with space group *C*2/*m*. In the *o*-$LiMnO_2$ structure, Mn and Li occupy the 2*a* Wyckoff site. The oxygen occupies the 2*b* Wyckoff site. The oxygen array is distorted from idea cubic-close packing due to Jahn-Teller effect on Mn^{3+}. The structure is built up from independent MnO_6 and LiO_6 octahedra that are arranged in corrugated layers. The Rietveld refinement shows that the degree of substitution of Li/Mn in the octahedra is about

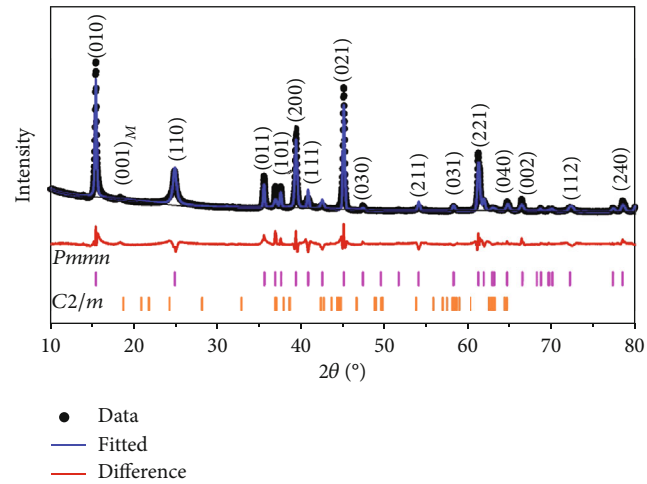

Figure 1: XRD pattern of prepared sample indexed against the standard *o*-$LiMnO_2$ (PDF #35-0749, space group *Pmmn*) and Li_2MnO_3 phase (PDF #84-1634, space group *C*2/*m*).

Table 1: Rietveld refinement and crystal data obtained from the XRD data.

Phase	*o*-$LiMnO_2$	Li_2MnO_3
Space group	*Pmmn*	*C*2/*m*
Phase fraction	90%	10%
Lattice parameter (Å)	$a = 4.5758$	$a = 4.8660$
	$b = 5.7482$	$b = 8.4210$
	$c = 2.8100$	$c = 5.0257$
		$\beta = 108.9202$
Li/Mn substitution	5%	
Fitting quality	R_p (%) = 5.35	
	R_{wp} (%) = 8.03	
	χ^2 (%) = 10.99	

5%. The cation disorder can improve the electrochemical performance of the cathode [17–19]. The lattice parameter of *o*-$LiMnO_2$ is slightly smaller than that in literature [20]. This might be caused by the effect of the Li_2MnO_3 phase.

SEM and TEM analyses were performed to study the particle's morphology and are shown in Figure 2. Accordingly, the particles have a well-defined shape (Figure 2(a)). The particles are elongated, parallelogram-shaped grains. The particle size ranges from 100 to 400 nm. The *d*-spacing is calculated as 0.588 nm, which corresponds to the (010) plane at $2\theta = 15°$. These results further confirm the predominance of the *o*-$LiMnO_2$ phase with good crystallinity of the particles.

To examine the oxidation state of Mn in the compound, XPS measurement was carried out and shown in Figure 3. The survey XPS profiles (Figure 3(a)) contain peaks at ~641, 530, 285, and 55 eV, which are allocated for Mn 2p, O 1s, C 1s, and Li 1s, respectively. This indicates the presence of Li, Mn, C, and O in the sample. The presence of C is due to the absorption of CO_2 from the air onto the sample's surface

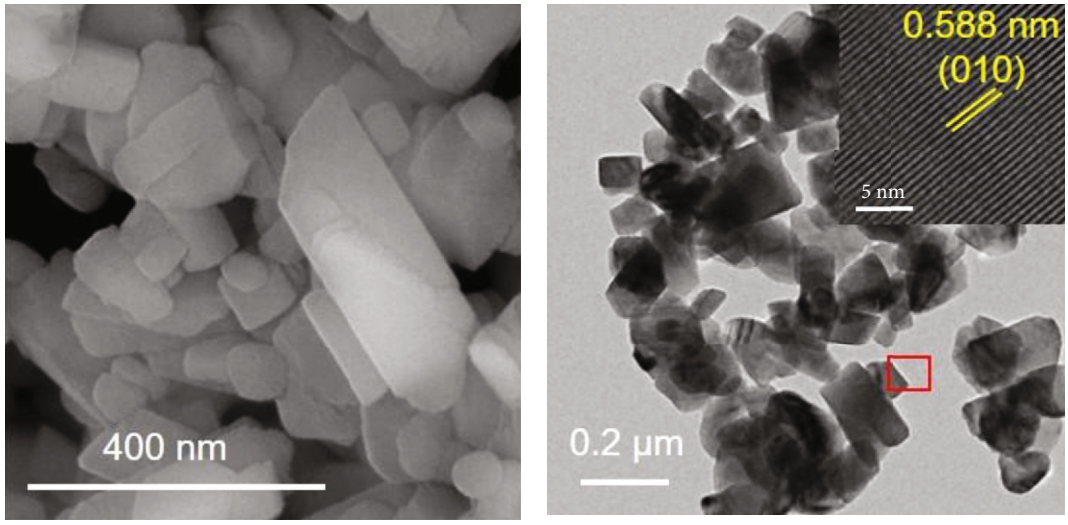

Figure 2: (a) SEM and (b) TEM of the sample. Enlarged image of marked region shows lattice fringe.

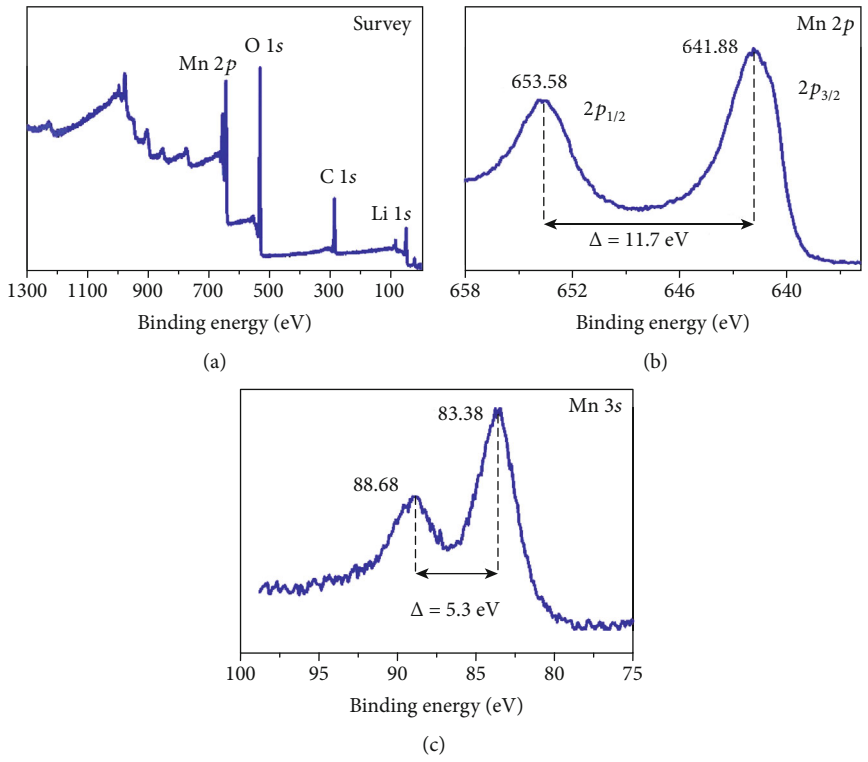

Figure 3: XPS spectra of (a) survey, (b) Mn 2p, and (c) Mn 3s of the sample.

[21–23]. Figure 3(b) shows the Mn 2p core-level spectrum, which exhibits two peaks, namely, Mn $2p_{3/2}$ and Mn $2p_{1/2}$. These peaks locate at 641.88 and 653.58 eV, respectively, with the spin-orbital splitting value of 11.7 eV. The binding energy of Mn $2p_{3/2}$ of the sample is in between binding energy of those in Mn_2O_3 (641.6 eV) and MnO_2 (642.6 eV) [24]. This result indicates the coexistence of both Mn^{3+} and Mn^{4+} in the sample. Figure 3(c) shows the Mn 3s spectrum to further evaluate the oxidation state of Mn. The splitting in Mn 3s spectrum is caused by the coupling of the nonionized 3s electron with 3*d* valence-band electrons, and its value indicates the oxidation state of Mn. Here, it is 5.3 eV so the oxidation state of Mn in the compound is +3.

Figure 4 shows the charge-discharge curve and the corresponding *dQ*/*dV* plot, measured between 2.0 and 4.8 V at C/10 rate (1C = 280 mA g^{-1}) at the 1st, 2nd, and 5th cycles. The cell exhibits two charging voltage plateaus at 3.45 and 4.3 V. The plateau at 4.5 V which is typical for the activation

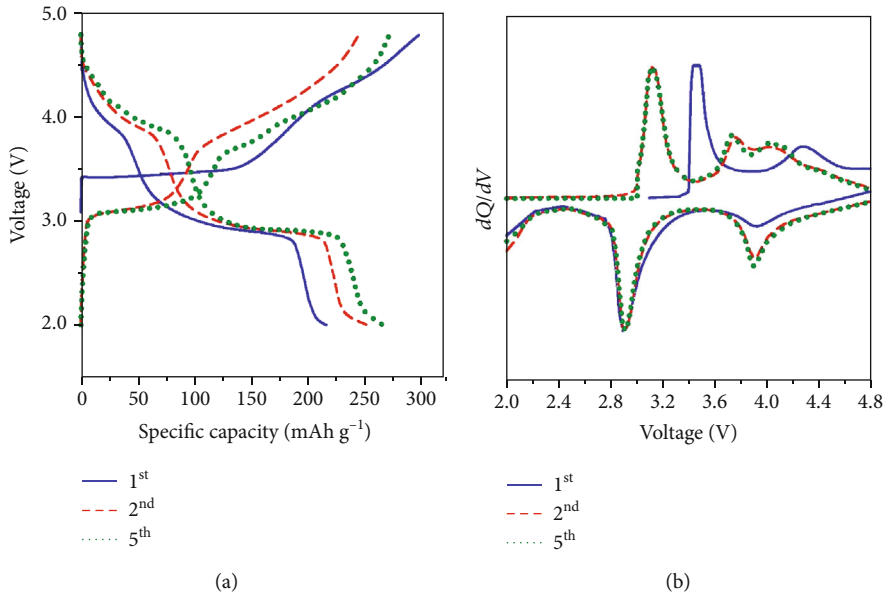

Figure 4: (a) Charge-discharge profiles and (b) corresponding dQ/dV plots for the 1st, 2nd, and 5th cycles of the sample.

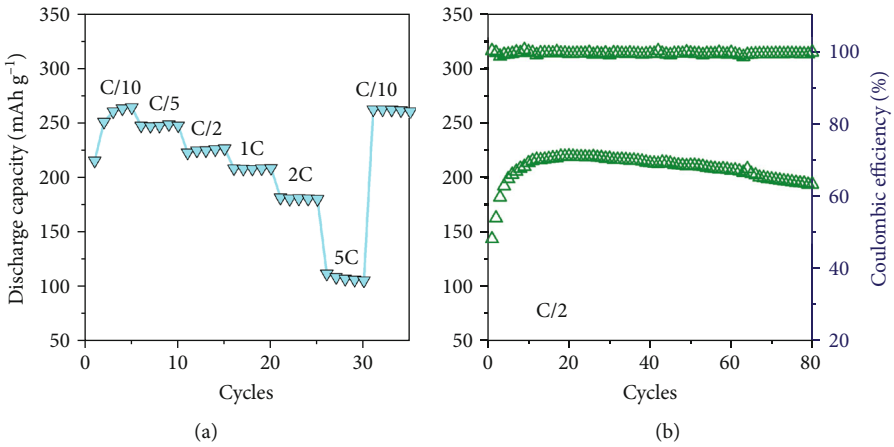

Figure 5: Cycling stability of the sample at (a) different C-rates and (b) at C/2.

of Li_2MnO_3 does not appear. It might be caused by the small fraction of the Li_2MnO_3 phase. The plateaus at 3.45 V are irreversible due to the structural change. For the first discharge, there is a plateau at 4 V and a long plateau ~3.0 V. The first charge and discharge capacity is 297 and 216 mAh g^{-1}, respectively. The low first Coulombic efficiency (72.7%) is due to the irreversible structural change during the first cycle of the $LiMnO_2$ and Li_2MnO_3 phase [4, 6, 25–31]. During cycling, the capacity contribution in the 4 V region increases, resulting in an increase in the overall capacity. After 5 cycles, the cathode could deliver a capacity of 265 mAh g^{-1}, which is higher than those reported in the literature [20, 32–37]. The dQ/dV plot (Figure 4(b)) shows peaks that correspond to the plateaus observed in Figure 4(a). For the first cycle, the peak at 3.5 V is irreversible while the peak at 4.3 V is reversible and there is a strong peak appearing at 2.9 V. For the subsequent cycles, the peak at 4.3 V shifts to lower voltage and induces two peaks at 3.8 and 4.0 V. These are typical peaks of spinel $LiMnO_4$, indicating the transformation of o-$LiMnO_2$ to a spinel-like phase during cycling [38].

A fresh cell was cycled 5 times at each C-rate including C/10, C/5, C/2, 1C, 2C, and 5C between 2.0 and 4.8 V to check its C-rate performance. Figure 5(a) shows the resulting discharge capacities. At C/10 rate, the highest capacity of 265 mAh g^{-1} is obtained after 5 cycles. With increasing C-rate, the capacities decrease as expected. The capacity is 249, 226, 208, 180, and 103 mAh g^{-1} for C/5, C/2, 1C, 2C, and 5C, respectively. The capacity is still as high as 263 mAh g^{-1} at C/10 after a severe test at 5C. Figure 5(b) shows the cycling stability and Coulombic efficiency of the sample at C/2. The capacity increases gradually over the first 12 cycles due to the transition of o-$LiMnO_2$ to a new spinel-like phase [4, 39]. However, the transformation is slow in this compound due to the stabilization of the Li_2MnO_3 phase. After 80 cycles, the capacity retention is 93%. The Coulombic efficiency is close to 100%, indicating less energy loss during the charge-discharge process.

4. Conclusion

o-$LiMnO_2$ was successfully synthesized by the hydrothermal method. The XRD and XPS results show the existence of the Li_2MnO_3 phase. SEM and TEM analyses confirmed the presence of a dominant *o*-$LiMnO_2$ phase with particle sizes in the range of 100-400 nm. The galvanostatic cycling demonstrates that a high capacity of 265 mAh g^{-1} and 93% capacity retention after 80 cycles at C/2 could be achieved with this cathode. The structural change from the initial phase to the spinel-like phase is retarded due to the stabilization of the Li_2MnO_3 phase. Lastly, this work promotes environmentally friendly, low-cost, and high-capacity cathode materials for LIBs.

Data Availability

The data used to support the findings of this study are available from the corresponding author upon request.

Conflicts of Interest

The authors declare that there is no conflict of interest regarding the publication.

Acknowledgments

This research is funded by the Vietnam National Foundation for Science and Technology Development (NAFOSTED) under grant number 103.02-2019.26 and the Ministry of Science and Technology of Vietnam under the project code NĐT.75.CHN/19.

References

[1] P. Yan, J. Zheng, J. Xiao, C.-M. Wang, and J.-G. Zhang, "Recent advances on the understanding of structural and composition evolution of LMR cathodes for Li-ion batteries," *Frontiers in Energy Research*, vol. 3, no. 26, pp. 1–10, 2015.

[2] Z. Yang, J. Zhang, M. C. W. Kintner-Meyer et al., "Electrochemical energy storage for green grid," *Chemical Reviews*, vol. 111, no. 5, pp. 3577–3613, 2011.

[3] B. Li, W. Zhao, C. Zhang et al., "Monodispersed $LiFePO_4$@C core-shell nanoparticles anchored on 3D carbon cloth for high-rate performance binder-free lithium ion battery cathode," *Journal of Nanomaterials*, vol. 2020, Article ID 2607017, 11 pages, 2020.

[4] Y. I. Jang, B. Huang, H. Wang, D. R. Sadoway, and Y. M. Chiang, "Electrochemical cycling-induced spinel formation in high-charge-capacity orthorhombic $LiMnO_2$," *Journal of the Electrochemical Society*, vol. 146, no. 9, pp. 3217–3223, 1999.

[5] D. Y. W. Yu and K. Yanagida, "Structural analysis of Li_2MnO_3 and related Li-Mn-O materials," *Journal of the Electrochemical Society*, vol. 158, no. 9, pp. A1015–A1022, 2011.

[6] D. Y. W. Yu, K. Yanagida, Y. Kato, and H. Nakamura, "Electrochemical activities in Li_2MnO_3," *Journal of the Electrochemical Society*, vol. 156, no. 6, pp. A417–A424, 2009.

[7] D. Kim, G. Sandi, J. R. Croy et al., "Composite 'layered-layered-spinel' cathode structures for lithium-ion batteries," *Journal of the Electrochemical Society*, vol. 160, no. 1, pp. A31–A38, 2013.

[8] J. C. Im, N. H. Vu, H. Tran Huu, D. S. H. Lee, and W. B. Im, "Effects of fluorine doping on electrochemical performance of spinel-layered Li3Mn3O7.5-xFxas cathode materials for Li-ion batteries," *Journal of the Electrochemical Society*, vol. 166, no. 8, pp. A1568–A1573, 2019.

[9] M. Freire, N. V. Kosova, C. Jordy et al., "A new active Li-Mn-O compound for high energy density Li-ion batteries," *Nature Materials*, vol. 15, no. 2, pp. 173–177, 2016.

[10] Y. Liu, G. Liu, H. Xu et al., "Low-temperature synthesized $Li_4Mn_5O_{12}$-like cathode with hybrid cation- and anion-redox capacities," *Chemical Communications*, vol. 55, no. 56, pp. 8118–8121, 2019.

[11] D. Y. Wan, Z. Y. Fan, Y. X. Dong et al., "Effect of metal (Mn, Ti) doping on NCA cathode materials for lithium ion batteries," *Journal of Nanomaterials*, vol. 2018, Article ID 8082502, 9 pages, 2018.

[12] N. H. Vu, P. Arunkumar, J. C. Im, and W. B. Im, "High capacity $Li_{1.5}MnTiO_{4+\_\delta\_}$ as thermally stable core-shell-driven cathode materials for lithium-ion batteries," *Journal of Alloys and Compounds*, vol. 704, pp. 459–468, 2017.

[13] N. H. Vu, J. C. Im, S. Unithrattil, and W. B. Im, "Synergic coating and doping effects of Ti-modified integrated layered-spinel Li1.2Mn0.75Ni0.25O2+δas a high capacity and long lifetime cathode material for Li-ion batteries," *Journal of Materials Chemistry A*, vol. 6, no. 5, pp. 2200–2211, 2018.

[14] Y.-I. Jang, W. D. Moorehead, and Y.-M. Chiang, "Synthesis of the monoclinic and orthorhombic phases of $LiMnO_2$ in oxidizing atmosphere," *Solid State Ionics*, vol. 149, no. 3-4, pp. 201–207, 2002.

[15] X. Huang, Q. Zhang, H. Chang, J. Gan, H. Yue, and Y. Yang, "Hydrothermal synthesis of nanosized $_{LiMnO[sub\ 2]–Li[sub\ 2]MnO[sub\ 3]}$ compounds and their electrochemical performances," *Journal of The Electrochemical Society*, vol. 156, no. 3, p. A162, 2009.

[16] N. H. Vu, P. Arunkumar, J. C. Im et al., "Effect of synthesis temperature on the structural defects of integrated spinel-layered $Li_{1.2}Mn_{0.75}Ni_{0.25}O_{2+\delta}$: a strategy to develop high-capacity cathode materials for Li-ion batteries," *Journal of Materials Chemistry A*, vol. 5, no. 30, pp. 15730–15742, 2017.

[17] A. Boulineau, L. Croguennec, C. Delmas, and F. Weill, "Structure of Li_2MnO_3 with different degrees of defects," *Solid State Ionics*, vol. 180, no. 40, pp. 1652–1659, 2010.

[18] R. Wang, X. Li, L. Liu et al., "A disordered rock-salt Li-excess cathode material with high capacity and substantial oxygen redox activity: $Li_{1.25}Nb_{0.25}Mn_{0.5}O_2$," *Electrochemistry Communications*, vol. 60, pp. 70–73, 2015.

[19] N. H. Vu, S. Unithrattil, V. H. Hoang, S. Chun, and W. B. Im, "Template-engaged synthesis of spinel-layered $Li_{1.5}MnTiO_{4+\_\delta\_}$ nanorods as a cathode material for Li-ion batteries," *Journal of Power Sources*, vol. 355, pp. 134–139, 2017.

[20] S. Komaba, S.-T. Myung, N. Kumagai, T. Kanouchi, K. Oikawa, and T. Kamiyama, "Hydrothermal synthesis of high crystalline orthorhombic $LiMnO_2$ as a cathode material for Li-ion batteries," *Solid State Ionics*, vol. 152-153, pp. 311–318, 2002.

[21] N. H. Vu, H. T. T. Le, V. H. Hoang et al., "Highly N-doped, H-containing mesoporous carbon with modulated physicochemical properties as high-performance anode materials for Li-ion and Na-ion batteries," *Journal of Alloys and Compounds*, vol. 851, article 156881, 2021.

[22] Z. Zheng, W.-B. Hua, C. Yu et al., "Heterogeneous intergrowth $_{xLi1.5Ni0.25Mn0.75O2.5\cdot(1}$ − x)Li0.5Ni0.25Mn0.75O2(0 ≤ x ≤ 1) composites: synergistic effect on electrochemical performance," *Dalton Transactions*, vol. 44, no. 32, pp. 14255–14264, 2015.

[23] J. Sicklinger, M. Metzger, H. Beyer, D. Pritzl, and H. A. Gasteiger, "Ambient storage derived surface contamination of NCM811 and NCM111: performance implications and mitigation strategies," *Journal of the Electrochemical Society*, vol. 166, no. 12, pp. A2322–A2335, 2019.

[24] D. BriggsG. E.Muilenberg Perkin-Elmer Corp, "Handbook of X-ray Photoelectron Spectroscopy," in *Surface and Interface Analysis*, C. D. Wanger, W. M. Riggs, L. E. Davis, and J. F. Moulder, Eds., vol. 3, no. 4pp. 78-79, Physical Electronics Division, Eden Prairie, Minnesota, USA, 1981.

[25] Z. X. Shu, I. J. Davidson, R. S. McMillan, and J. J. Murray, "Electrochemistry of $LiMnO_2$ over an extended potential range," *Journal of Power Sources*, vol. 68, no. 2, pp. 618–622, 1997.

[26] J. Lim, J. Moon, J. Gim et al., "Fully activated Li_2MnO_3 nanoparticles by oxidation reaction," *Journal of Materials Chemistry*, vol. 22, no. 23, pp. 11772–11777, 2012.

[27] A. D. Robertson and P. G. Bruce, "Mechanism of electrochemical activity in Li_2MnO_3," *Chemistry of Materials*, vol. 15, no. 10, pp. 1984–1992, 2003.

[28] R. Wang, X. He, L. He et al., "Atomic structure of Li2MnO3-after partial delithiation and re-lithiation," *Advanced Energy Materials*, vol. 3, no. 10, pp. 1358–1367, 2013.

[29] D. Y. W. Yu, K. Yanagida, Y. Kato, and H. Nakamura, "Electrochemical activities in $_{Li[sub\ 2]MnO[sub\ 3]}$," *Journal of the Electrochemical Society*, vol. 156, no. 6, pp. A417–A424, 2009.

[30] N. H. Vu, V.-D. Dao, H. Tran Huu, and W. B. Im, "Effect of synthesis temperature on structure and electrochemical performance of spinel-layered $Li_{1.33}MnTiO_{4+z}$ in Li-ion batteries," *Energies*, vol. 13, no. 11, p. 2962, 2020.

[31] N. H. Vu, V.-D. Dao, H. N. Van et al., "Spinel-layered $Li_2MnTiO_{4+\_z\_}$ nanofibers as cathode materials for Li-ion batteries," *Solid State Sciences*, vol. 103, article 106178, 2020.

[32] S. T. Myung, S. Komaba, and N. Kumagai, "Synthesis of orthorhombic LiMnO2as a high capacity cathode for Li-ion battery by emulsion drying method," *Chemistry Letters*, vol. 30, no. 6, pp. 574-575, 2001.

[33] X.-D. Li, W.-S. Yang, S.-C. Zhang, D. G. Evans, and X. Duan, "The synthesis and characterization of nanosized orthorhombic $LiMnO_2$ by in situ oxidation-ion exchange," *Solid State Ionics*, vol. 176, no. 7-8, pp. 803–811, 2005.

[34] S.-h. Wu and M.-t. Yu, "Preparation and characterization of _o_ -$LiMnO_2$ cathode materials," *Journal of Power Sources*, vol. 165, no. 2, pp. 660–665, 2007.

[35] S. Chen, F. Cao, F. Liu et al., "Facile hydrothermal synthesis and electrochemical properties of orthorhombic LiMnO2-cathode materials for rechargeable lithium batteries," *RSC Advances*, vol. 4, no. 26, pp. 13693–13703, 2014.

[36] W. K. Pang, J. Y. Lee, Y. S. Wei, and S. H. Wu, "Preparation and characterization of Cr-doped $LiMnO_2$ cathode materials by Pechini's method for lithium ion batteries," *Materials Chemistry and Physics*, vol. 139, no. 1, pp. 241–246, 2013.

[37] X. Xiao, L. Wang, D. Wang, X. He, Q. Peng, and Y. Li, "Hydrothermal synthesis of orthorhombic $LiMnO_2$ nano-particles and $LiMnO_2$ nanorods and comparison of their electrochemical performances," *Nano Research*, vol. 2, no. 12, pp. 923–930, 2009.

[38] S.-T. Myung, S. Komaba, and N. Kumagai, "Hydrothermal synthesis and electrochemical behavior of orthorhombic $LiMnO_2$," *Electrochimica Acta*, vol. 47, no. 20, pp. 3287–3295, 2002.

[39] R. J. Gummow, D. C. Liles, and M. M. Thackeray, "Lithium extraction from orthorhombic lithium manganese oxide and the phase transformation to spinel," *Materials Research Bulletin*, vol. 28, no. 12, pp. 1249–1256, 1993.

Hindawi
Journal of Nanomaterials
Volume 2021, Article ID 5586951, 7 pages
https://doi.org/10.1155/2021/5586951

Review Article

Estimating the Possibility of Lead Contamination in Soil Surface due to Lead Deposition in Atmosphere

Nguyen Thi Lan Binh, Nguyen Trung Hoang, Nguyen Thi Thanh Truc, Vu Dinh Khang, and Hung Anh Le

Institute for Environmental Science, Engineering and Management, Industrial University of Ho Chi Minh City, Vietnam

Correspondence should be addressed to Nguyen Thi Lan Binh; nguyenthilanbinh@iuh.edu.vn

Received 1 March 2021; Revised 12 April 2021; Accepted 23 April 2021; Published 12 May 2021

Academic Editor: Ajit Kumar Sharma

An increase in heavy metal soil contamination, especially lead, in the industrial area or near industrial areas has become a serious environmental problem. An industrial zone including paints, electrical plants, metal works, machining, and smelting factories, in the suburban of Ho Chi Minh City, was chosen as the study area. Soil samples were collected from the industrial area and in the residential area next to the industrial area for three experiments, namely, lead content in the surface soils, lead leachate into the water, and movement of lead in soil. Then, the results were compared to the values in the Soil Contamination Countermeasures Law of the Japan Ministry of Environment to assess the possibility of soil contamination which may cause health risks to a human living in that area. The results of the analysis show that the soil has been contaminated by lead. In particular, the lead concentrations of the surface soil samples are 23–35 mg kg^{-1}, while the lead elution of soil samples is quite high, about 0.6 mg L^{-1}. With these results, the soil can harm people by direct ingestion. More importantly, this work proves that lead species have been going down gradually. To assess the possibility of lead approaching groundwater, more further studies need to be achieved.

1. Introduction

Lead (Pb) and its compounds may exist in nature or as a product of transportation or metalwork manufacturing, etc. Although lead can be emitted by various sources, industrial sources take a big part in lead contamination [1]. The U.S. EPA in 2014 reported that a high level of airborne lead is found near the industrial operations that materials containing lead, such as metal works, paints… [2]. In recent studies, many scientists also have indicated that high smokestacks of these factories are the factor to spread heavy metal pollution in a wide area [3–5]. Therefore, people who live in the zone that is adjacent to the contamination sources have a high possibility to get health risk from heavy metal contamination.

Lead compounds can be divided into two general categories, namely, inorganic lead and organic lead. The inorganic lead compounds usually consist of lead in a divalent state such as lead carbonate, lead oxide, and lead sulfate, while organic lead compounds, lead tetraethyl and lead tetramethyl, were found in automotive gasoline [6]. Lead compound particles suspend in the atmosphere for over three weeks and are spread many hundreds of kilometers by the wind and then settle onto the ground through a wet deposition. Particles larger than 10 millimeters, which constitute up to 95% of the emission, may settle out within short distances [1]. In Vietnam, to control soil pollution, there is a national regulation named National Technical Regulation on the Allowable Limits of Heavy Metals in the Soils [7]. In this, the total lead concentration in a residential area and the industrial area is limited at 120 mg kg^{-1} and 300 mg kg^{-1}, respectively [7]. However, according to several previous works, a type of soluble lead compounds can cause harm to human health and the environment with small concentrations, while insoluble lead compounds can do with a significant concentration [8].

Humans and animals may inhale or ingest lead that is the main route to exposure to lead. According to Fritz Bischoff et al., there are six lead compounds which are the most toxic

because of their solubility, namely, ionic lead, colloidal lead hydroxide, metallic lead, glycerophosphate, oleate, and stearate [9], while some insoluble compounds such as lead oxychloride, oxy carbonate, and carbonate are supposed to have less toxicity than soluble compounds, because these insoluble compounds probably are removed from the bloodstream before they have a chance to react with the constituents of the blood. Lead exposure causes some serious harmful effects on various systems in the human body. Various previous studies indicate that lead causes a decrement in neurological function, cognitive function, low IQ, and even cancer. Lead poison also affects the reproductive system, kidney, liver, and gastrointestinal tract [8]. Not only causing an effect on human health, lead deposition also brings some serious problems to the ecosystem. By lead deposition, for a long time, lead species can accumulate within the surface soil and run deeper into groundwater. This may cause a drop in biodiversity, animals, and plants [10, 11]. Therefore, controlling soil pollution by total lead concentration will not be relevant to protect people who live near an industrial area. In a study about estimating the atmospheric lead deposition on surface soil pollution by Lan et al., the Soil Contamination Countermeasures Law was applied to assess the lead contamination in an area around a cement factory [12]. For soil and groundwater protection, the Soil Contamination Countermeasures Law was issued by the Japanese government in 2002 [13]. This law declares designated hazardous standards and a designation standard for soil contamination assessment, in which the soil is assessed as contaminated if it exceeds either the soil concentration standard which risks for direct ingestion or the soil leachate standard risk for ingestion of groundwater. In this case, lead and lead compounds are limited to 150 mg Pb kg^{-1} soil on soil concentration standard and 0.01 mg Pb L^{-1} solution on soil leachate standards [13].

In this study, we used the Japan Soil Contamination Countermeasures Law to assess the lead pollution in the industrial area and the residential area. The goals of this work are to determine the level of lead in soil from the industrial area and its neighborhoods that may cause risk to human health when a lead substance enters the human body by ingestion. Besides, the possibility of lead elution into the ground and the movement of lead through soil layers were also studied.

2. Experimental Method

2.1. Study Area. Sample collection was carried out in and around an industrial zone famous for steelwork, electronics, and machinery in Ho Chi Minh City suburban. This industrial zone has 195 hectares for industrial work and 77 hectares for the residents. In recent years, because of employment demand, human density in this area has been increasing quickly and uncontrollably. The increasing population density in a potentially polluted zone raises health safety concerns. Thus, it is necessary to have a study evaluating soil pollution here to serve the health risk assessment in the future.

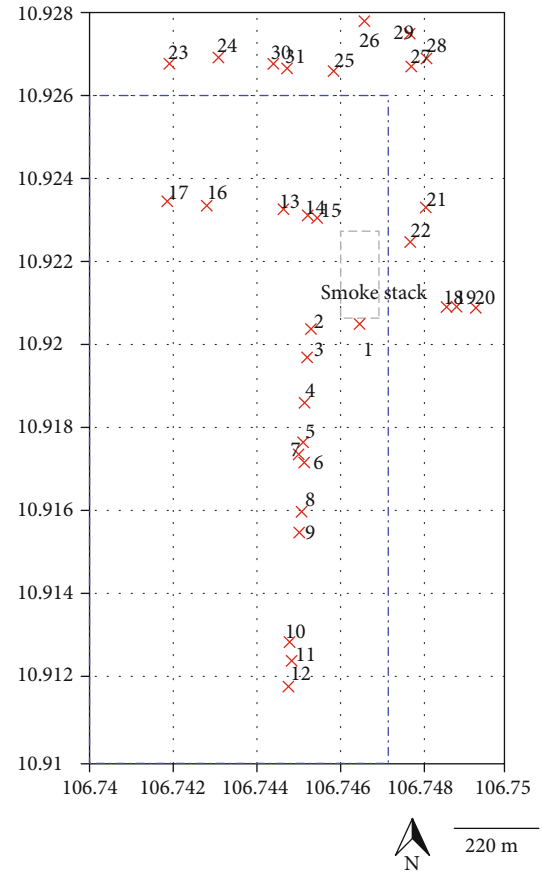

Figure 1: Sampling locations, in which inside the dashed line box are those in the industrial operation, while outside the dashed line box are those in the residential area. The *y*-axis shows the latitude of samples' coordinates while the *x*-axis shows their longitude.

According to the site survey, there are many potential lead contamination sources in the industrial zone, but a smokestack of steelwork factories is supposed to be the main source that can spread polluted aerosols in a wide area. Therefore, to determine the lead contamination due to atmospheric deposition, the steelwork smokestack was chosen as the main source of lead emission.

Wind direction is not certain in this area. Two main directions are north to south and inverse way. For that, the samples were focused on the north-south axis (Figure 1). The soil sampling was taken in late May and during the rainy season of Ho Chi Minh City. Soil samples were always wet. The study area had a warm temperature ranging from 30°C to 38°C at that moment. The soil in the area was characterized by loam, sandy, and clay.

2.2. Sample Procedure. To determine the lead content and lead elution, a total of 31 surface soil samples including 17 samples in the industrial area and 14 samples in the residential area were collected in a radius of 1 kilometer from the steelwork factory's stack (Figure 1). The sample sites were not distributed evenly in the study area because the land is almost covered by roads and factories in the industrial area. Surface soil samples were collected at the depth of 0–2

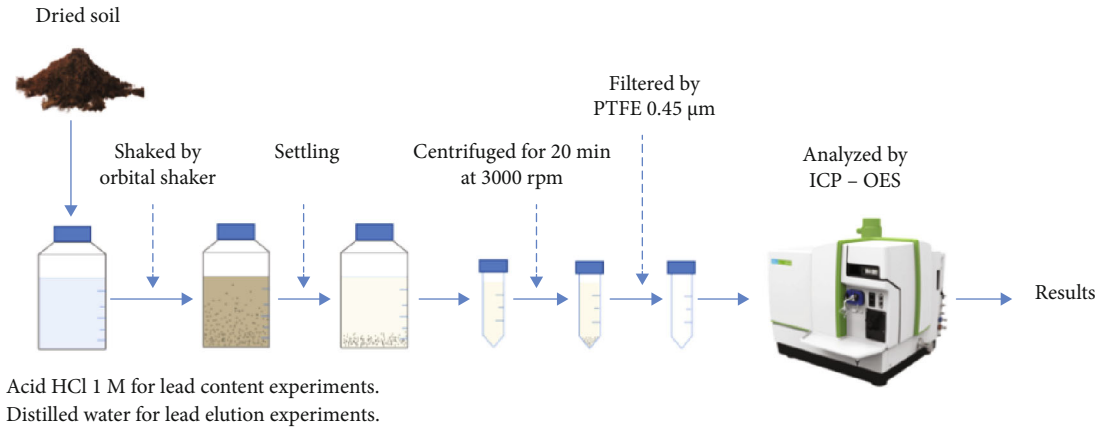

Figure 2: Lead content and lead elution analysis method schematic.

centimeters after cleaning off the grass, waste, rocks, and so on. 31 soil samples are divided into 4 groups which represent for their location that correlate with the smokestack on the map, in which samples 1 to 12 are in the south of the smokestack, samples 13 to 17 are in the east, samples 18 to 22 are in the west, and samples 23 to 31 are in the north.

Soil layer samples were also collected from six spots within the study area to estimate a lead moving into the soil. These spots were decided by three spots in the industrial area and three others in the residential area. Four layers of samples were collected at every 2 centimeters from the surface samples. All soil samples were sieved through to 2 millimeters of plastic sieve opening to remove vast wastes, rock, etc. Finally, each analytical sample was stored in a zip lock bag.

2.3. Elemental Analysis

2.3.1. Measurement of Lead Content in Soil Samples. In this work, the lead content (mg kg^{-1}) of each soil sample was analyzed to estimate the risk of lead contamination in the industrial zone and the residential zone. Sample preparation followed the Japanese Ministry of the Environment's Notification No. 9 [14]. The general method schematic is shown in Figure 2. For lead concentration in soil experiment, a dried soil sample was mixed with hydrochloric acid (HCl) 1 M with the ratio of 3 grams of soil in 100 mL acid. At first, a sample emulsion was prepared by putting 6 grams of dry soil into a 250 mL polypropylene bottle then adding gradually HCl 1 M to 200 mL. HCl was purposely controlled at 1 M to simulate acid in the human stomach that helps to estimate the risk of lead contamination to human health when people or children accidentally ingest. The mixture of soil and HCl 1 M had been shaken for 2 hours at 200 rounds per minute. Then, the solution had been settled for 20 min before centrifuging for 20 minutes at 3000 rounds per minute. The centrifuged solution was filtered with a 0.45 μm pore size syringe filter PTFE membrane before being analyzed by inductively coupled plasma optical emission spectrometry (ICP–OES Spectroblue, Spectro Ametek, Germany).

ICP–OES uses unit mg L^{-1} to represent the content of solution lead. To make a comparison with the regulations, we have to change the unit mg Pb L^{-1} of the volume of sample solution to unit mg Pb kg^{-1} of dried soil which is showed in

$$C_1\left(\frac{\text{mg}}{\text{kg}}\right) = \frac{C_2(\text{mg/L}) \times (V\,(\text{mL})/1000)}{M_{\text{soil}}/1000}, \quad (1)$$

in which C_1 is the lead concentration in soil (mg kg^{-1}), C_2 is the lead concentration in ICP–OES result (mg L^{-1}), V is the volume of HCl 1 M (mL), and M_{soil} is the weight of soil extracted in HCl 1 M (gram). In this study, M_{soil} = 6 grams.

2.3.2. Measurement of Lead Elution into Groundwater. Soil leachate into groundwater was carried on to determine the concentration of lead that can dissolve in water. Sample preparation and analysis methods are based on the method shown in the Japanese Ministry of the Environment's Notification No. 9 [14] and the study of Nguyen et al. in 2018 [12]. According to Figure 2, the method of lead elution analysis is quite similar to lead content experiment but we replaced acid with distilled water. Firstly, 10 g of dried soil was mixed with 100 mL distilled water with a ratio of 1 gram of soil in 10 mL water. The emulsion was contained in a polyethylene container. And then, it had been shaken for 6 hours at a speed of 200 rounds per minute. After 40 minutes of the sedimentation, the solution was poured into a Falcon tube and then centrifuged for 20 minutes at 3000 rounds per minute. Finally, the sample solution was filtered with a 0.45 μm pore size syringe filter PTFE membrane before being analyzed by ICP–OES. The result of lead elution is shown in the unit of mg L^{-1}.

3. Results and Discussion

3.1. Lead Content in Surface Soil Samples May Cause a Health Risk. We assume that if a child playing in the study area accidentally eats a certain amount of soil, will the child have any adverse health effect? Figure 3 depicts the lead concentration in soil can dissolve in HCl 1 M which imitated human's stomach acid. In this work, the lead concentration fluctuates from 23 mg kg^{-1} to 35 mg kg^{-1}. However, there were 6 samples with nonlead detection occupying 20% of the total amount of samples. This proportion is very interesting. In this work, 31

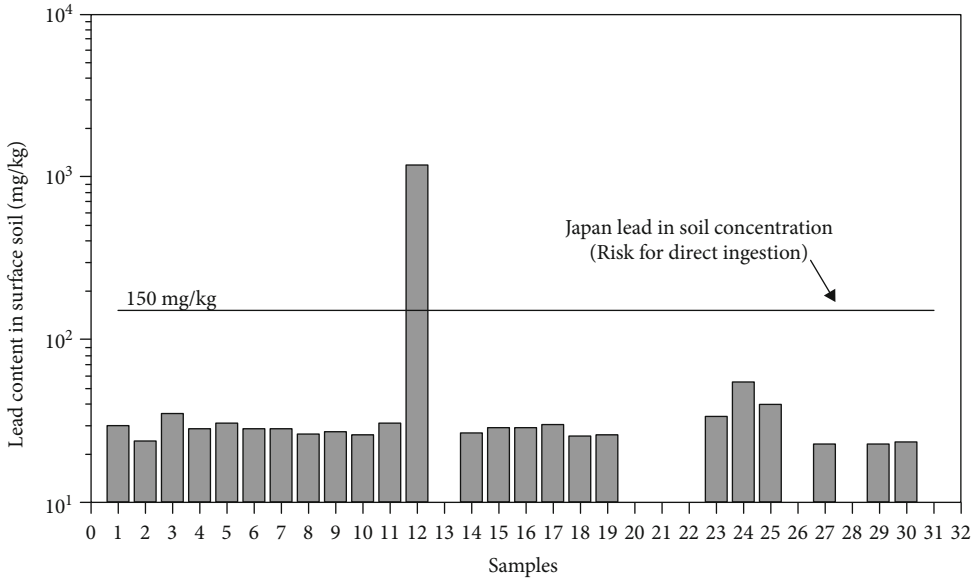

Figure 3: Lead content results of surface soil samples compared to Japanese lead in soil concentration standard at 150 mg kg^{-1}.

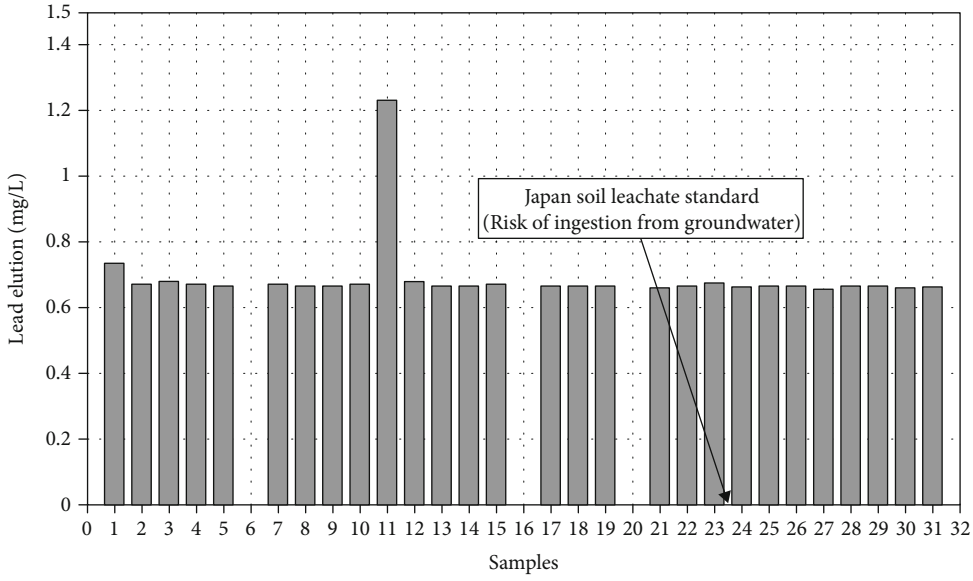

Figure 4: Lead elution results of surface soil samples compared to Japanese soil leachate standard at 0.01 mg L^{-1}.

soil samples are separated into four groups which represent for their locations mentioned in Sample Procedure. We notice that nonlead samples C20, C21, and C22 are on the west of the smokestack while nonlead samples C26, C28, C31, and C32 are on the north of the smokestack. We suppose that wind direction has played an important role in air pollution spread. The airborne heavy metals have tended to move to the south because of the wind. Lead concentrations in most of the samples are 4-6 times lower than the risk threshold of the Japanese Soil Contamination Countermeasures Law (150 mg kg^{-1}) [13] and 8-12 times lower than that in the Vietnamese Heavy Metal Limit in Soil Regulation (300 mg kg^{-1}) [7], except for sample C12. However, it should be noted that the Vietnamese regulation on lead concentrations above is the concentration in the soil. In the fact that only soluble lead compounds affect human health, sample C12 has a remarkably high lead concentration, 1187 mg kg^{-1}. This may be due to some exotic agents causing high lead contamination such as batteries and paint waste on the ground.

According to the site survey in this industrial zone, we suppose that there are two major lead emission sources, namely, a steelwork factory and a paint factory. A paint factory undoubtedly is a source of heavy metal contamination in soil [15]. Nevertheless, the paint factory is a point pollution source that cannot spread airborne heavy metal in a large area. Look at Figure 3; samples C27, C29, and C30, which are about 800 meters away from the steelwork factory stack, also have quite the same lead concentration as

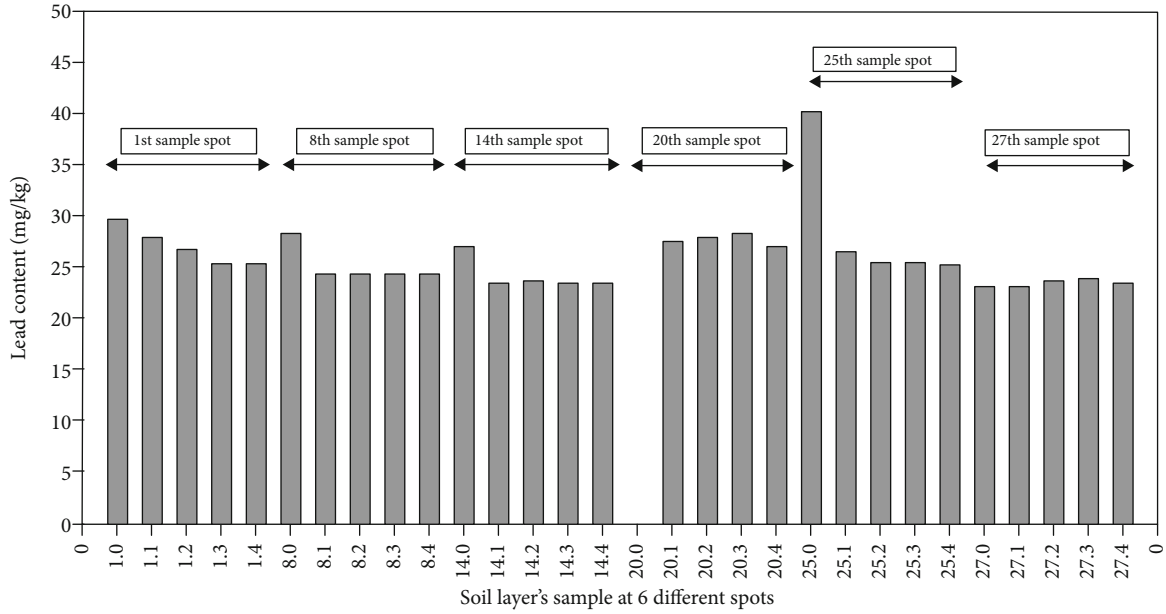

FIGURE 5: Lead content results in soil layer samples. There were 5 layers of soil from 0 cm to 10 cm at each sample spot alternatively: 1st sample spot, 8th sample spot, 14th sample spot, 20th sample spot, 25th sample spot, and 27th sample spot.

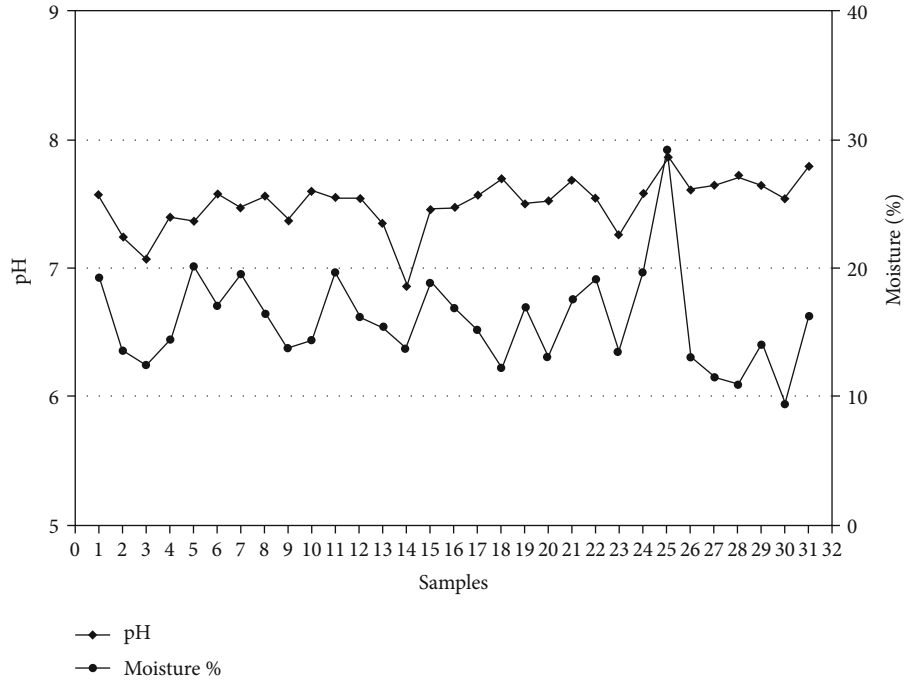

FIGURE 6: pH and moisture of 31 soil samples.

that of samples near the stack. Because of that, we stated that the 25-meter stack of steelwork factory is the main heavy pollution source in the study area. More interestingly, this steelwork factory is established in 2012, but the lead contamination level in the residential area is as high as in the industrial area. Therefore, the lead content that accumulates gradually in the future will cause serious risks to the residence.

3.2. Lead Elution into Groundwater. Similar to the lead content in surface soil experiments, 31 soil samples from Section 3.1, which are so-called E1 to E31, were extracted by water. Lead concentrations are shown in Figure 4. In general, the lead elution of most soil samples is much higher than the upper limit in the Japanese Soil Contamination Countermeasures Law (0.01 mg L^{-1}) [13]. This is truly dangerous for children playing at a playground who may drink water on the

ground accidentally. There are 3 water samples that had nondetected results, while 27 water samples have a lead elution 60 times higher than that of threshold in the law. In particular, sample E11 has a lead concentration over 120 times more than the threshold.

In industrial works, there are many kinds of lead compounds that exist. However, this result shows that the lead contamination in the study area is contributed by highly dissolvable lead substance's proportion, for example, lead acetate, lead chloride, and lead nitrate. The dissolvable lead substances are really dangerous to human health. Moreover, with high lead elution, the groundwater is soon contaminated with lead.

3.3. Lead Concentration in Soil Layers. Lead species tend to follow the water flow upon going down. However, the movement of lead through the soil is slow because a strong tendency to be adsorbed onto organic matter and clay particles makes it immobile and biologically inert. In 1996, Maskall et al. examined soil samples in the lead-smelting site, which proved no movement farther than 70 centimeters in 200 years [16]. The mobility of lead in soil depends on various factors, for instance, the type of soil, pH, moisture content of the soil, and water infiltration. In this experiment, there are three types of soils in which loam appears in samples No. 1, No. 8, No. 20, and No. 25; clay appears in sample No. 14; sand appears in sample No. 27. Lead concentrations in each soil layer as data for the movement of lead examiners are reported in Figure 5. Generally, samples No. 1, No. 8, No. 14, and No. 25 have the same trend, the concentration of lead in the lower layers slice lower than that in the surface layer. Mostly, the lead at 10 centimeters from the surface is around $23\,mg\,kg^{-1}$ to $28\,mg\,kg^{-1}$. Water passes slowly through the loam soils and more slowly in the case of clay. That is why lead moves gradually from the surface to the lower layers. In contrast, sandy soils do not hold water well and it goes down quickly. In the results of sample No. 27, the lead contents at the surface and lower layers show no difference.

The pH and moisture of soil also impact the movement of lead. Figure 6 shows the results of pH and the moisture % of each surface soil sample. The pH of the soils in this work fluctuated from 6.9 to 8. At neutral or higher pH, the soil holds lead species strongly. Usually, atmospheric lead is deposited on the surface of the soil (2–5 centimeters) and retains in it when pH is higher than 5 [17].

4. Conclusions

Lead exists in many forms in the environment. It can come from natural sources such as in ores or from nonnatural sources such as from industrial activities and transportation. Usually, lead and its compounds emitted from industrial works are hazardous. These toxic materials are released into an industrial zone's atmosphere every day. And then, they get into the soil by the wet deposition process. More importantly, the population density near the industrial zone is increasing rapidly in Vietnam that raised up a concern in health safety. After this study, according to the Soil Contamination Countermeasure Law of Japan, the surface soil in the industrial area and near the industrial area has been contaminated by lead, even though the lead concentration is lower than the upper limit. Interestingly, the lead elution is too much higher, about 60 to 120 times more than the safety threshold. The lead elution will affect groundwater sooner or later.

Data Availability

No data were used to support this study.

Conflicts of Interest

The authors declare that they have no conflicts of interest.

References

[1] I. Thornton, R. Rautiu, and S. Brush, "Lead: The Facts," vol. 40, no. 2, 2001.

[2] EPA, *Report on the environment - lead emission*, 2014.

[3] R. A. Wuana and F. E. Okieimen, "Heavy metals in contaminated soils: a review of sources, chemistry, risks and best available strategies for remediation," *ISRN Ecology*, vol. 2011, Article ID 402647, 20 pages, 2011.

[4] K. Šichorová, P. Tlustoš, J. Száková, K. Kořínek, and J. Balík, "Horizontal and vertical variability of heavy metals in the soil of a polluted area," *Plant, Soil and Environment*, vol. 50, no. 12, pp. 525–534, 2011.

[5] R. Martin, K. Dowling, D. Pearce, J. Sillitoe, and S. Florentine, "Health effects associated with inhalation of airborne arsenic arising from mining operations," *Geosciences*, vol. 4, no. 3, pp. 128–175, 2014.

[6] National Toxicology Services Program Department of Health and Human, *Report on carcinogens-lead and lead compounds*, Natl. Toxicol. Serv. Progr. Dep. Heal. Human, 14th edition, 2004.

[7] "QCVN 03 : 2008 / BTNMT Quy chuẩn kỹ thuật quốc gia trong đất National technical regulation on the allowable limits of heavy metals in the soils," 2008.

[8] H. Abadin, A. Ashizawa, Y.-W. Stevens et al., "Toxicological profile for lead," 2019.

[9] R. D. E, F. R. N. F. Bischoff, and L. C. Maxwell, "Studies on the toxicity of various lead compounds given intravenously," *Journal of Pharmacology and Experimental Therapeutics*, vol. 34, pp. 85–109, 1928.

[10] "Air pollution from Lead. General information on lead, and the TCEQ planning activities addressing the lead standard-Texas Commission on Environment QualityJune 2019, https://www.tceq.texas.gov/airquality/sip/criteria-pollutants/sip-lead.

[11] A. L. Wani, A. Ara, and J. A. Usmani, "Lead toxicity: a review," *Interdisciplinary Toxicology*, vol. 8, no. 2, pp. 55–64, 2015.

[12] B. Nguyen Thi Lan, T. Kobayashi, A. Suetsugu, X. Tian, and T. Kameya, "Estimating the possibility of surface soil pollution with atmospheric lead deposits using the ADMER model," *Sustainability*, vol. 10, no. 3, p. 720, 2018.

[13] S. Aoki, "Soil contamination countermeasures law," *Japan Tappi Journal*, vol. 57, no. 10, pp. 1475–1493,021, 2003.

[14] "The lead content in the soil was measured by the Japan Ministry of the Environment, Notification N.19," 2004, September 2019, http://www.env.go.jp/hourei/06/000029.html.

[15] W. Ji, T. Yang, S. Ma, and W. Ni, "Heavy metal pollution of soils in the site of a retired paint and ink factory," *Energy Procedia*, vol. 16, pp. 21–26, 2012.

[16] J. Maskall, K. Whitehead, C. Gee, and I. Thornton, "Long-term migration of metals at historical smelting sites," *Applied Geochemistry*, vol. 11, no. 1–2, pp. 43–51, 1996.

[17] S. C. Xintaras, *Impact of lead-contaminated soil on public health*, U.S. department of health and human services, Public Health Service, Agency for Toxic Substances and Disease Registry, Atlanta, Georgia, 1992, https://wonder.cdc.gov/wonder/prevguid/p0000015/p0000015.asp.